Strongly Interacting Many-Body Systems in Cold Atomic Gases

Von der Fakultät Mathematik und Physik
der Universität Stuttgart
zur Erlangung der Würde eines Doktors der
Naturwissenschaften (Dr. rer. nat.) genehmigte Abhandlung

vorgelegt von

Jens Daniel Honer

aus Böblingen

Hauptberichter: Prof. Dr. Hans Peter Büchler
Mitberichter: Prof. Dr. Walter Metzner
Prüfungsvorsitz: Prof. Dr. Tilman Pfau

Tag der mündlichen Prüfung: 8.3.2013

Institut für Theoretische Physik III
Universität Stuttgart
2013

Abstract

The remarkable progress in control over cold atomic gases has led to a point where people are no longer satisfied with merely studying these systems, but rather put them to use to understand complex quantum many-body systems. The basis of this development is a deep understanding of the interaction between atoms, and how to exploit those in order to engineer interesting and novel quantum-systems. The aim of this particular thesis is to contribute to this *third quantum revolution* [1] and hence help to understand the inner workings of complex many-body systems.

We present a method to control the shape and character of the interaction between cold atoms based on dressing the atomic ground-state with a Rydberg-state. The latter induces a van der Waals interaction between all the atoms in the ensemble, and allows for control via the coupling light-field. We find that with increasing atom densities the ensemble shows a direct transition into a collective regime that preempts the onset of three-body interactions associated with a break-down of the first Born-approximation. The reason for this intriguing behavior is the strong interaction between Rydberg atoms that gives rise to the blockade-mechanism, and prevents the simultaneous excitation to the Rydberg-state for spatially close atoms. The non-trivial behavior of the interaction-potential within the collective regime yields a novel tool for shaping the interaction between ground-state atoms beyond s-wave scattering. We study this collective regime and the resulting interaction-potential between the atoms within a variational/mean-field approach, and discuss its effects on a trapped Bose-Einstein condensate.

Artificial atoms show remarkable properties, that are often superior to *real* atoms. In particular, since they are built out of many constituents, such systems often exhibit an enhanced coupling to the light-field as well as strong optical non-linearities even for small light-fields. On the other hand, noise in quantum-mechanical systems can not only destroy coherence, but rather can be used in order to robustly drive a system into an interesting state. We study the effect of a controlled dephasing onto an artificial atom in the context of an ensemble of atoms coherently coupled to a Rydberg state and demonstrate that such an enhanced artificial atom allows for the deterministic absorption of a single photon from an arbitrary incoming probe field. Such behavior yields a unique tool in light-matter interaction, and opens the path to realise quantum-networks or to fabricate novel quantum-devices. Here, we discuss the applicability of this single-photon absorber as a single-photon transistor, a high fidelity n-photon counter, and a device that allows for the deterministic creation of non-classical states of light via photon-subtraction.

A non-trivial topological order of quantum-states leads to conservation of certain properties and, hence, increases their robustness against external perturbations. This can even stabilize quantum-states against local fluctuations. The latter usually corrupts the coherence within a macroscopic object and thereby prevents quantum-phenomena to occur in our macroscopic world. As an example of such a topological state, we study the behavior of vortex-excitations in a two-dimensional superfluid confined to a periodic potential, as can be realised within a cold atomic gas in an optical lattice. For large superfluid filling factors and strong interactions, the healing-length and, accordingly, the vortex core is much smaller than the lattice spacing. As a result, vortices are confined to the plaquettes of the lattice, and can be described in the framework of an effective tight-binding Hamiltonian. Via a first-principle calculation based on coherent-state path-integrals we derive the microscopic parameters of this model and provide an analytic expression for the vortex mass. Moreover, we show that such a quantum vortex is not obliged to follow the superfluid flow, but rather exhibits Bloch-oscillations perpendicular to it, which is a telltale sign for quantum interference of this macroscopic many-body excitation.

Recently, Jonathan Simon et al. [2] performed a major step towards simulating quantum many-body systems in cold atomic gases by simulating the paramagnet-antiferro-magnet transition of a one-dimensional Ising-model. Fundamental excitations in the phase with broken translational symmetry are domain-walls carrying fractional statistics. The question is, whether experimentally accessible single-particle excitations, which correspond to two closely-bound domain-walls, decay into fractional excitations or remain closely-bound. By use of perturbation theory, we derive an analytic model for the time-evolution of these fractional excitations in the framework of a tilted Bose-Hubbard model, and demonstrate the existence of a repulsively bound state above a critical center-of-mass momentum. The validity of the perturbative approach is confirmed by the use of t-DMRG simulations. Together with the recent demonstration of single-site addressing and readout in optical lattices, these findings open the path for experimental observation of fractional excitations within cold atomic gases.

Zusammenfassung

Die Forschung an ultra-kalten Quantengasen ist heute nicht mehr ausschliesslich reiner Selbstzweck. Vielmehr versucht man kalte Gase als Werkzeug zu verwenden, um komplexe Vielteilchen-Systeme besser zu verstehen. Die Grundlage dieser erstaunlichen Entwicklung ist ein tiefes Verständnis über die Wechselwirkung zwischen den Atomen, sowie die Möglichkeit diese nach Belieben zu verändern, und dadurch interessante und neuartige Quantensysteme zu kreieren. Ziel dieser Dissertation ist es, einen Beitrag zu dieser *dritten Quanten-Revolution* [1] zu leisten, und so komplexe Vielteilchen-Systeme besser zu verstehen.

Wir zeigen eine Methode, um sowohl die Form als auch den Charakter der Wechselwirkung zwischen kalten Atomen zu verändern. Unser Ansatz basiert auf der Möglichkeit dem Grundzustand der Atome etwas von einem angeregten Rydberg-Zustand beizumischen. Die van der Waals Wechselwirkung zwischen Rydberg-Atomen überträgt sich so auf jedes einzelne Atom im Ensemble. Erhöht man die Wechselwirkung, so zeigt das Ensemble einen direkten Übergang in ein kollektives Regime, wobei das Regime mit dominanten Dreiteilchen-Wechselwirkungen übersprungen wird. Der Grund für dieses faszinierende Verhalten ist der Blockade-Mechanismus zwischen Rydberg-Atomen, welcher die Anregung räumlich naher Atome verhindert. Dieses nicht-triviale Verhalten des Wechselwirkungs-Potentials im kollektiven Regime stellt ein neuartiges Werkzeug dar, um die Wechselwirkungen zwischen Atomen über die s-Wellenstreuung hinaus zu beeinflussen. Wir untersuchen dieses kollektive Regime und das daraus resultierende Wechselwirkungs-Potential zwischen den Atomen mit Hilfe eines Variations- / Mean-Field-Ansatzes, und diskutieren dessen Auswirkungen auf ein Bose-Einstein-Kondensat in einer harmonischen Falle.

Die extremen Eigenschaften künstlicher Atome sind denen realer Atome in vielen Aspekten überlegen. Da sie aus mehreren Teilchen aufgebaut sind, zeigen derartige Systeme oft eine erhöhte Kopplung an das Lichtfeld sowie starke optische Nicht-Linearitäten, die schon bei kleinen Feldstärken signifikante werden. Auf der anderen Seite sind Fluktuationen in quantenmechanischen Systemen nicht ausschliesslich Quellen von Dekohärenz, sondern können dazu genutzt werden um ein System zuverlässig in einen interessanten Zustand zu bringen. Wir studieren die Auswirkungen von kontrolliertem Dephasieren auf ein künstliches Atom, genauer eines Ensembles von Atomen das kohärent an einen Rydberg-Zustand gekoppelt ist.

Wir zeigen, dass ein derart verbessertes künstliches Atom deterministische Einzel-Photonen-Absorption ermöglicht. Dieses Verhalten stellt eine einzigartige Licht-Materie-Wechselwirkung dar, die den Weg für Quanten-Netzwerke und neuartige Quanten-Geräte ebnet. Insbesondere diskutieren wir die Anwendbarkeit des Einzel-Photonen-Absorbers als einen Einzel-Photonen-Transistor, einen hochauflösenden n-Photonen-Zähler sowie als Quelle für nicht-klassische Licht-Zustände.

Eine nicht-triviale topologische Ordnung führt zu neuen Erhaltungssätzen und verringert damit die Empfindlichkeit des Systems gegen äussere Störungen. Insbesondere erlaubt dies die Stabilisierung von Zuständen trotz lokaler Fluktuationen, welche üblicherweise die Kohärenz innerhalb eines makroskopischen Objekts und damit das Auftreten von Quanten-Phänomenen in unserer makroskopischen Welt verhindern. Als ein Beispiel eines solchen topologischen Zustands untersuchen wir das Verhalten von Vortex-Anregungen in einem zweidimensionalen Superfluid in einem periodischen Potential. Ein derartiges System kann zum Beispiel über ein kaltes atomares Gas in einem optischen Gitter realisiert werden. Im Regime mit vielen superfluiden Teilchen pro Gitterplatz sowie starken Wechselwirkungen ist die Kohärenz-Länge, welche die Grösse des Vortex-Kerns bestimmt, viel kleiner als die Gitterkonstante. Die Vortices sind damit auf den Plaquetten des Gitters gefangen, und können gut mit einem effektiven *tight-binding* Hamiltonian beschrieben werden. Basierend auf einer mikroskopischen Beschreibung des Superfluids leiten wir mittels Pfad-Integralen die mikroskopischen Parameter dieses Modells her, und geben einen analytischen Ausdruck für die Vortex-Masse an. Wir zeigen, dass im Gegensatz zum klassischen Fall ein massiver Quanten-Vortex nicht dem superfluiden Strom folgt, sondern Bloch-Oscillationen orthogonal dazu ausführt, und damit eine klare Signatur für Interferenz einer Vielteilchen-Anregung zeigt.

Jonathan Simon et al. [2] simulierten vor kurzem den Paramagnet-Antiferromagnet-Übergang in einem eindimensionalen Ising-Modell mittels kalter Atome und leisteten damit einen wichtigen Beitrag zum Gebiet der Quanten-Simulation. Die fundamentalen Anregungen in der Phase mit gebrochener Translations-Symmetrie sind Domänenwände, welche eine fraktionelle Statistik aufweisen. Die Frage ist nun, ob die experimentell zugänglichen Einteilchenanregungen, die zwei eng gebundenen Domänenwänden entsprechen, in fundamentale Anregungen zerfallen können oder gebunden bleiben. Mit einem störungstheoretischen Ansatz leiten wir ein analytisches Modell für die Zeit-Evolution der fraktionellen Anregungen her, und zeigen die Existenz eines repulsiv-gebundenen Zustands oberhalb eines kritischen

Schwerpunkts-Impulses. Zusätzlich bestätigen wir unsere analytische Rechnung durch numerische t-DMRG-Simulationen. Mit der neusten Generation von Experimenten, die das Adressieren und Auslesen einzelner Plätze in einem optischen Gitters erlaubet, eröffnet dies die Möglichkeit fraktionelle Anregungen in kalten atomaren Gasen zu beobachten.

"If the laws of physics no longer apply in the future …
God help you."

—Portal 2

Contents

Chapter 1

Introduction

Imagine you want to understand a very complex system. Rather than try and account for everything at once, it is the very human nature to simplify and concentrate on particular aspects. These simplifications might not give accurate predictions, and leave some or even most phenomena unexplained. Nevertheless, they are useful as long as they capture the basic idea of the particular aspect one is interested in. In theoretical physics, this concept of simplification is well established. In fact, already Isaac Newton reduced whole planets and suns to point-like objects in his quest to understand gravitation. Needless to say, he was quite successful in his approach.

Today, cold atomic gases offer the same possibility for experimental physics: They allow for the creation of a simplified version of a complex quantum many-body systems as is often found in condensed-matter physics, and thus to perform experiments in an idealized environment.

Yet one might ask: *Would it not be simpler to use the version nature gave you?* Well, the answer is *sometimes*. Cold atomic gases offer the possibility to observe a particular system in its purest form, that is without undesirable effects such as dissipation, disorder, and all those minor annoyances which in total might obscure the effect one actually hopes to observe. In that sense, experiments on cold atoms have more in common with a simulation rather than an actual experiment: One is quite sure about the model describing the system, but not about how the system will behave. Moreover, there are measurements that are incredibly hard or even impossible to perform in solid materials, yet straightforward in cold atomic gases (and vice versa). Hence, the different point of view offered by cold atomic gases might shed light on systems whose inner workings have been elusive for decades.

In the beginning years of cold atomic physics the main focus of research was to reach a Bose-Einstein condensate, and, after its realization by Wieman and Cornell [3] in 1995, to explore the coherent properties of this intriguing macroscopic quantum-state [4–6]. However, the remarkable success of ultra-cold atomic gases in recent years is based on the possibility to reach the strongly-correlated regime, in which interactions rather than the properties of individual particles govern the behavior of the system [1,7,8]. On the one hand, these strongly-correlated systems exhibit a rich variety of interesting phenomena, such as superfluidity in liquid helium, fractional quantum-hall excitations and the peculiarity of high-temperature superconductivity. On the other, they are notoriously hard to understand, as often standard methods, both analytically and numerically, simply fail. To achieve this highly interesting regime, the interaction energy of the particular system needs to exceed its kinetic energy, and basically leaves one with two paths to follow:

The first one is to increase the interaction energy by increasing the interaction itself, and was explored by Stoof et al. [9] in 1996. They proposed to use Feshbach resonances in order to fabricate a BCS pairing in a degenerate gas of ^{6}Li. In general, a Feshbach resonance appears whenever the energy of two scattering particles coincides with the energy of a bound state, which in that context are called open and closed channel, respectively. The scattering particles are then temporarily captured in this particular bound state, and the resulting delay in emission yields an effective increase in the scattering-length depending on the relative energetic distance between open and closed channel. Now, the main reason for Feshbach-resonances to be so commonly used in cold atomic gases is the possibility to tune this energy difference and, in consequence, the scattering length via an external macroscopic parameter: For instance, if the open and closed channel feature different magnetic moments, a uniform magnetic field can be applied in order to change their relative energetic position, and, in turn, the scattering length [10]. It is thus possible to create a smooth transition from the weakly-interacting to the strongly-correlated regime, without any change on the experiment itself. Such a setup was first realised experimentally by Cornish and coworkers [11] in 2000. Unfortunately, the increase in scattering length led to a decrease in the condensate lifetime due to three-body losses.

An alternative route was followed by Jaksch et al. [12]: They proposed to use a so called optical lattice to reduce the kinetic energy by restricting the motion of the atoms. Exposing an atom to a coherent light-field induces a constant energy shift $E_{\mathrm{ac}} \sim I/\Delta$, where I is the intensity of the light field and $\Delta = \omega - \omega_{\mathrm{a}}$ is the detuning of the laser frequency ω from the nearest atomic transition ω_a [1,8]. This energy shift is due to the dipole-force, and can be understood as the time-dependent version of the Stark-effect, the so called ac-Stark shift. Interference between two laser beams creates a spatial modulation of the light-intensity and yields a periodic potential for the atoms with a length-scale given by half the laser wave-length. The combination of several lasers then allows for the creation of near arbitrary lattice geometries, ranging from a simple one-dimensional stack of atomic *pancakes* to complicated structures such as a Kagome lattice [13]. Both the lattice-depth and the lattice-spacing can be tuned by the laser frequency as well as the overall light-intensity. Typically, the lattice-depth is much larger than the thermal energy of cold atoms. For a three-dimensional lattice, the atoms are thus confined to small, quasi-one-dimensional lattice sites. Although their low thermal energy prevents them from moving over the energy barrier, quantum mechanics allows them to tunnel, and therefore hop from one site to another. This hopping then corresponds to the kinetic energy of the atoms and depends exponentially on the lattice depth. On the other hand, if two atoms occupy the same lattice site, their interaction gives rise to an energy shift. Again, this can be tuned by the lasers generating the lattice as well as the aforementioned Feshbach-resonances. Yet, the strong atomic localization prevents particles to interact if they are on different lattice sites. The simple picture of particles tunneling from one site to another and interacting only if they are on the same site can be cast in the famous Bose-Hubbard model [14], which is an exemplary model for strongly correlated Bosons. In a beautiful experiment in 2002, Markus Greiner and coworkers [15] realised such a system within a Bose-Einstein condensate, and observed a quantum phase transition from a superfluid phase in which particles move freely all over the lattice to a Mott-insulating phase where the atoms sit put on their respective lattice site.

From these beginning steps of manipulating the properties of cold atomic gases a whole field of quantum engineering has developed over the last decade. This remarkable progress is based on both experimental achievements in increasing the control over atoms as well as theoretical understanding on how to exploit the basic properties of cold atomic gases. Given the abundance of good review articles about cold atomic gases, we will name but a few of the most famous publications, and refer the interested reader to the literature [4, 7, 10, 16].

One of the first experiments to demonstrate the capabilities of cold atomic gases in modeling solid-state physics was the fabrication of a Tonks-Giradeau gas [17] as a first example of a bosonic Luttinger-liquid [18] by Kinoshita et al. [19] and Paredes et al. [20] following the proposal of Petrov, Shlyapnikov and Walraven [21]. Another beautiful experiment by Juliet Billy and coworkers [22] demonstrated Anderson-localization [23] of a Bose-Einstein condensate by use of a speckle pattern of light, and opened the path to study disorder in these systems. In two dimensions, Hadzibabic [24] observed a crossover between a phase with an exponential decay of correlations and a phase with quasi-long-range order, in which correlations decay algebraically, and thus provides evidence for a Berezinskii-Kosterlitz-Thouless-type transition [25] from a phase of bound vortex pairs to one of free vortices. Another way to efficiently prepare interesting many-body states is the use of long-range interactions due to Rydberg excitations. Those might offer the possibility to study dynamics and disorder for scalable quantum information networks, as was recently reported by Dudin et al. [26].

In next generation experiments, built in Munich and Harvard by Sherson et al. [2] and Bakr et al. [27], that allow for single-site addressing and imaging in optical lattices, one can actually see atom dynamics in an optical lattice. By use of these techniques Cheneau et al. [28] reported on the observation of correlation spreading in an optical lattice and Endres et al. [29] studied a Higgs-mode in a two-dimensional neutral superfluid. Simon et al. [2] made a huge step towards a dedicated quantum-computer by simulating the antiferromagnet-paramagnet transition in an Ising-model at the multi-critical point.

Although a fully fledged quantum-computer is still a long way from realization, the recent advances in control over quantum-matter might lead to systems that are capable to simulate specific strongly-correlated models. Such dedicated quantum-simulators can help to understand whether certain analytically unsolvable models are even applicable in the first place, and carry the effects one hopes to describe. Following Feynman, this *quantum revolution associated with control over macroscopic quantum systems and the rise of quantum technologies* [1] might give insight into the inner workings of solid-state systems which eluded our understanding so far. There is still much work to do in both experimental control over the cold atomic gases as well as our theoretical understanding of these systems and what they are actually capable of. Yet, *steps to enlightenment brighten the way; but the steps are steep. Take them one at a time.* [30]. In this thesis I try to take one of the steep steps, and hopefully contribute to the understanding of strongly-correlated many-body systems.

In chapter 2 we study the influence of Rydberg dressing on the ground state wave-function of a Bose-Einstein condensate. Due to their huge spatial extent, Rydberg atoms are easily polarizable and feature a strong van der Waals interaction. Quantum mechanics then allows one to admix the strongly interacting Rydberg state to the atomic ground state, and thus induce a long-range interaction-potential between all atoms in the ensemble. In the weak-dressing limit, the interaction is governed by two-body processes, and can be treated approximately within an adiabatic Born-Oppenheimer approach. However, this approximation breaks down if one increases the Rabi-frequency coupling the ground- and Rydberg-state. Although one would expect three-body and higher-order interactions to become gradually important, we show that the system exhibits a direct transition into a collective regime where all orders of the interaction need to be taken into account. This remarkable behavior is a result of the blockade-mechanism of Rydberg atoms that prevents the simultaneous Rydberg excitation of two atoms in close vicinity. We apply a variational/mean-field approach in order to derive an effective interaction-energy from the microscopic Hamiltonian. As a result, this allows us to describe the system within a generalized Gross-Pitaevskii equation and to derive the condensate wave-function in the Thomas-Fermi limit.

The weak interaction between light and matter renders photons a promising candidate for quantum information transport. Yet, this very property requires an efficient way to convert an excitation in a light-field into one of a quantum-system, and usually takes some stringent requirements on the side of the light-field, such as a π pulse or a *Stimulated Raman Adiabatic Passage* (STIRAP). In Chapter 3 we demonstrate how to circumvent most of these restrictions and to create a system that is capable to deterministically absorb a single photon from a probe-beam with minimal requirements on the probe-beam itself. The design is based on the blockade-mechanism, as can be realised in an artificial atom, in combination with a controlled dephasing of the excited states. The latter breaks the bright- and dark-space invariance induced by a coherent light-field driving the transition from ground to the collective excited state. In turn, the modified artificial atom features enhanced absorption properties, which in the limit of infinite constituents create a perfect single-photon absorber. This design provides a unique tool in photon-matter interaction, and opens the path to create novel quantum-devices useful in several fields of research and technology. We explicitly address its application as a single-photon transistor, a high fidelity n-photon counter, and for deterministic creation of non-classical states of light via photon-subtraction.

In chapter 4, we investigate whether macroscopic many-body excitations such as topological defects can exhibit quantum-phenomena. In particular, we consider a cold atomic gas in a two-dimensional optical lattice, described within the framework of a Bose-Hubbard model. In the regime of large particle-filling and strong interactions close to the Mott-insulator transition, the lattice spacing is the defining length-scale of the system. As a result, the healing-length of the superfluid associated with the dimension of the vortex core is much smaller than the lattice spacing, so that the vortices are pinned to the plaquettes of the lattice. By use of a coherent-state path-integral formalism we obtain an effective action for the vortices that is similar to the action of charged particles under the influence of a perpendicular magnetic field. The low-distance cut-off provided by the lattice leads to dissipationless vortex-tunneling in this particular regime and, thereby, to a finite tunneling-rate associated with a vortex-mass, and, ultimately, gives rise to an effective tight-binding Hamiltonian for the vortices. In contrast to a classical massless vortex, the nearest-neighbor hopping in the tight-binding Hamiltonian yields a periodic dispersion relation. In the presence of a force we find that a vortex performs Bloch-oscillations that are a telltale sign for single-particle interference and, hence, quantum-behavior of a macroscopic many-body excitation.

In the final chapter 5, we study the behavior of excitations in a tilted one-dimensional optical lattice cast in the form of a Bose-Hubbard model. The equivalence of this model with the one-dimensional Ising-model suggests that fundamental excitations in a density-wave phase with two atoms on every other lattice site are domain-walls, which show fractional statistics. Yet, the only excitations accessible in this broken-symmetry phase correspond to two closely-bound domain-walls. The important question is then, whether such an experimentally accessible excitation decays into fundamental domain-wall excitations, or stays in its bound form. By use of a perturbative approach we derive an analytic model for the time-evolution of experimentally accessible excitations and show that the system features both the decay into fractional excitations as well as a stable bound state above a critical center-of-mass momentum. Furthermore, we confirm our findings via t-DMRG simulations, and provide parameters for experimental observation. Together with the recently demonstrated single-site readout in optical lattices, this opens the path to simulate fractional excitations in a well-controlled cold atomic setup.

Chapter 2

Collective Many-Body Interaction in Rydberg-Dressed Atoms

2.1 Motivation

A microscopic understanding of the interaction and the means to control them via external fields is one of the stepping-stones in the quest of finding novel and interesting quantum phases within ultra-cold atomic gases.
Nowadays, there are several tools available to alter interactions. Arguably the most prominent example are Feshbach-resonances [31–34], which allow for a tuning of the s-wave scattering-length an external magnetic or laser field [10], and can be efficiently implemented in experimental setups. However, to realise anisotropy or long-range behavior in particle interactions, one has to rely on different means. A path to implement the former are atomic gases with large magnetic dipole-moments. Lahaye [35] studied a Bose-Einstein condensate of ^{52}Cr purely governed by dipolar interactions. There, the anisotropy leads to a strong dependence of the stability on the trap-geometry, which results in a collapse of the condensate followed by a *Bose-Nova* with d-wave like features in the unstable region. To realise long-range interactions one can use atoms excited into an high-lying electronic state, namely a Rydberg-state [36]. The strong van der Waals interaction [37] of these exited atoms accounts for the famous excitation-blockade [38–42] and opens the path to explore novel quantum-phases and phase-transitions [43–45].
On the other hand, the concept of dressing ground-state atoms with an excited state [46] in order to create novel and interesting particle-behavior has been extensively studied in the past in the context of coupling polar molecules with different

rotational states to suppress inelastic scattering [47]. Pupillo and coworkers [45] proposed to tune the interaction between ground state atoms via Rydberg-dressing in the dipole-dipole regime, and studied the emergent quantum phases via Monte-Carlo simulations. The same idea was used by Henkel et al. [48] to show that the dressing with Rydberg s-states yields a roton-maxon excitation spectrum and a transition to a super-solid state in a Bose-Einstein condensate. Both proposals are based on an off-resonant coupling between ground- and Rydberg state in order to limit the losses via spontaneous emission from the excited Rydberg-state.

In this Chapter, we show that near-resonant coupling between ground and Rydberg-state does not necessarily lead to increased losses. Rather, the breakdown of the Born-approximation associated with the onset of three-body interactions is preempted by a transition into a collective regime. As a result, the system exhibits a direct crossover from a regime with dominating two-particle interaction to a collective many-body regime, in which the fraction of Rydberg-excitations becomes suppressed by their interaction. Since losses mainly depend on the number of Rydberg-excitations, this mechanism allows for a resonant coupling between ground and Rydberg-states. We show that in this regime the system can be described within the framework of a generalized Gross-Pitaevskii equation, and derive an effective interaction-potential via a variational/mean-field approach.

2.2 Rydberg-Dressing of a Single Atom

We start with a system of ultra-cold atoms driven into an excited Rydberg-state via a two-photon process. The relevant internal structure is well described by a three-level system: for the i-th atom, the ground-state $|g\rangle$ is coupled to the Rydberg-state $|r\rangle$ via an intermediate p-state $|p\rangle$, see Fig. 2.1. The Rabi-frequency and detuning for the transition from ground- to p-level is denoted by Ω_p and Δ_p, and for the transition from p-state to Rydberg-state by Ω_r and Δ_r. In order to avoid inhomogeneous light-intensities due to absorption [49], it is necessary to reduce the population of the intermediate state. Such a suppression can either be achieved by a far off-resonant coupling to the p-state, or, more elegantly, by tuning the system to the EIT-condition [50], in which the ground- and Rydberg-state form a dark state. Then, both schemes allow for an adiabatic elimination of the intermediate p-state, and reduce the internal structure to an effective two-state system (see ref. [51]). Henceforth, we concentrate on a simple setting in which the

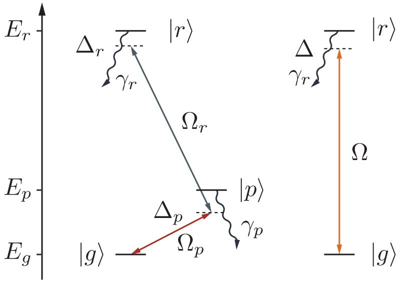

Figure 2.1: Setup for the ground-state dressing with the Rydberg-state $|r\rangle$ via the intermediate p-state with the corresponding Rabi-frequencies Ω_r and Ω_p as well as the detunings Δ_r and Δ_p. The decay-rates from the p-state and the Rydberg-state are denoted by γ_p and γ_r, respectively. (b) For far off-resonant coupling to the intermediate state, i.e. $\Delta_p \gg \Omega_r$, the system reduces to an effective two-state system with two-photon Rabi-frequency $\Omega = \Omega_r\Omega_p/2|\Delta_p|$ and total detuning $\Delta = \Delta_r + \Delta_p$.

coupling to the intermediate state is off-resonant, and comment on the suppression via EIT in the appendix 2.A. According to ref. [51], the two-photon Rabi-frequency takes the approximate form $\Omega = \Omega_r\Omega_p/2|\Delta_p|$, whereas the total detuning is given by $\Delta = \Delta_r + \Delta_p$. Although we are interested in the quantum-gas regime, where typical timescales are on the order of ms, the timescale of the internal degrees of freedom is on the order of μs, and gives rise to the notion of the frozen Rydberg-gas [52]. Accordingly, the microscopic single-atom Hamiltonian for the electronic degree of freedom in the rotating frame of the driving light-field is equivalent to a spin 1/2 model,

$$H_{\text{micro}} = \sum_i H_i = -\hbar\Delta \sum_i S_z^i + \hbar\Omega \sum_i S_x^i. \tag{2.1}$$

Spin-down corresponds to the atomic ground state, whereas spin-up corresponds to the excited Rydberg-state. Therefore, the spin operators in the z and x direction take the form $S_z^i = (|r\rangle\langle r| - |g\rangle\langle g|)/2$ and $S_x^i = (|r\rangle\langle g| + |g\rangle\langle r|)/2$, respectively. Diagonalization of the microscopic Hamiltonian then yields the eigenstates of the non-interacting system, namely

$$|\pm\rangle = \frac{1}{\sqrt{\Omega^2 + \left(\Delta \mp \sqrt{\Delta^2 + \Omega^2}\right)^2}} \begin{pmatrix} \Delta \mp \sqrt{\Delta^2 + \Omega^2} \\ -\Omega \end{pmatrix}, \tag{2.2}$$

and correspond to eigenenergies $E_\pm = \pm\frac{1}{2}\hbar\sqrt{\Delta^2 + \Omega^2}$ of the dressed atomic states.

2.3 Weak Dressing Limit and Two-Body Interaction

The van der Waals interaction between Rydberg atoms gives rise to an induced interaction between the dressed state $|-\rangle$ adiabatically connected to the ground state $|g\rangle$. The interaction-potential between two dressed states can then be obtained by diagonalizing the two-body Hamiltonian with van der Waals interaction, that is

$$H_{\mathrm{TB}} = \sum_{i=1}^{2} H_i + \frac{C_6}{2} \sum_{j \neq i} \frac{P^i P^j}{|\mathbf{x}_i - \mathbf{x}_j|^6}. \tag{2.3}$$

Here, $P^i = |r\rangle\langle r|_i$ is the projection operator onto the i-th excited Rydberg-state and C_6 is the van der Waals coupling parameter. A plot of the resulting eigenenergies over the separation x between the atoms is shown in Fig. 2.2. For far off-resonant coupling between ground and Rydberg-state, $\Delta \gg \Omega$, the energy level separation is on the order of the total detuning Δ, and thus allows for an adiabatic Born-Oppenheimer treatment [48]. More specifically, a fourth order perturbation in Ω/Δ yields the Born-Oppenheimer surface adiabatically connected to the many-body ground-state, and yields the interaction-potential

$$V_{\mathrm{BO}}(x) = -2|E_-| + \frac{\hbar\Omega^4}{8|\Delta|^3} \frac{1}{1 + (x/\xi_0)^6}, \tag{2.4}$$

where $\xi_0 = (C_6/4|E_-|)^{1/6}$ is the two-body blockade-radius [41] (see appendix 6.A.4). A comparison between the full interaction-potential derived via numerical diagonalization of the two-body Hamiltonian (2.3) and the Born-Oppenheimer approximation (2.4) is shown in Fig. 2.2 for a realistic set of parameters.

In the low-energy limit scattering between atoms is well described within the first Born-approximation and allows us to reduce the interaction-potential to a single interaction-parameter g_{eff} [4] associated with the s-wave scattering length via the

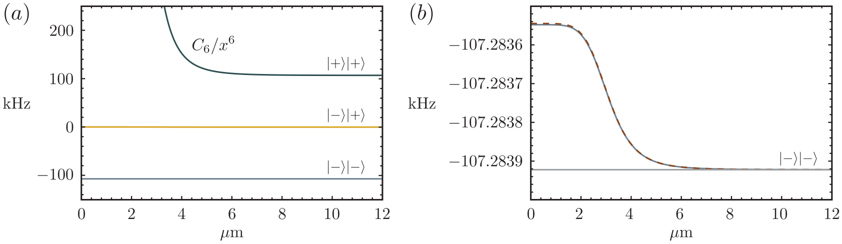

Figure 2.2: (a) Eigenvalues of the two-body Hamiltonian (2.3) as a function of the relative distance x between the atoms. We have choosen realistic parameters for a setup using a ^{87}Rb $|43s\rangle$ state with Rabi-frequency $\Omega = 7.8$ kHz, detuning $\Delta = 107$ kHz and van der Waals interaction coefficient $C_6 = 189$ Mhzμm^6. The lowest energy eigenstate then corresponds to the weakly-dressed ground state. Note that the energy-scale of the induced interaction is not visible in (a). (b) Comparison between the numerical diagonalization of (2.3) and the Born Oppenheimer interaction-potential (2.4).

relation $g_{\text{eff}} = 4\pi\hbar^2 a_{\text{s}}/m$. Since low energy corresponds to small momenta q, the problem of finding g_{eff} is equivalent to finding the Fourier-transform of the interaction-potential in the limit $q \to 0$. A straightforward calculation then yields the Fourier-transform of the interaction-potential (2.4),

$$V_{\text{eff}}(q) = \frac{\pi^2}{12}\frac{\hbar\Omega^4}{8|\Delta|^3}\xi_0^3 F(\xi_0 q), \tag{2.5}$$

with the momentum-dependent part

$$F(z) = \frac{e^{-z/2}}{z}\left[e^{-z/2} - 2\cos\left(\frac{\sqrt{3}}{2}z + \frac{\pi}{3}\right)\right]. \tag{2.6}$$

In the low-momentum limit $q \to 0$, the function $F \to 1$, and the effective interaction-potential reduces to

$$g_{\text{eff}} = \frac{\pi^2}{12}\sqrt{\frac{C_6}{2}}\frac{\hbar\Omega^4}{|\Delta|^{7/2}}. \tag{2.7}$$

Despite naive expectations this interaction parameter cannot be arbitrarily tuned by simply lowering the detuning Δ. Indeed, a small detuning will result in an increase in the Rydberg population and thereby an increase in spontaneous emission, and limits the timescale of any coherent experiment. A discussion of how to optimize the s-wave scattering in a realistic experimental setup can be found in appendix 2.C.

In the remaining part of this section, we provide an intuitive picture for the understanding of the Born-Oppenheimer interaction-potential (2.4). For $\Omega/\Delta \ll 1$, we can approximate the low-energy eigenstate $|-\rangle$ adiabatically connected to the ground-state $|g\rangle$ by a series expansion of eq. (2.2), so that

$$|-\rangle \approx \left(1 - \Omega^2/4\Delta^2\right)|g\rangle + \Omega/2\Delta|r\rangle + \mathcal{O}\left((\Omega/\Delta)^3\right). \tag{2.8}$$

Correlations between Rydberg-excitations vanish for large distances x between the atoms. Accordingly, the dressed atoms experience a van der Waals interaction, renormalized by the probability for the respective atom to be in the Rydberg-state. By introducing the notion of the Rydberg-faction, which in the limit of weak dressing reduces to $f = |\langle -|r\rangle|^2 = \Omega^2/4\Delta^2$, the effective interaction-potential can be cast in the compact form

$$V_{\text{eff}} = \langle -|H_{\text{TB}}|-\rangle = 2|E_-| + f^2\frac{C_6}{x^6}, \tag{2.9}$$

and corresponds to a leading order expansion in $1/x$ of eq. (2.4). On the other hand, the blockade-mechanism prevents both atoms to be in the Rydberg-state if their respective distance is small. This explains both the saturation of the interaction-potential on a length-scale given by the two-body blockade radius ξ_0 as well as its independence of the Rydberg interaction parameter, namely C_6. The finite energy shift for close distances is then due to the fact that the blockaded system acquires a collective ac-Stark shift driven by the collective Rabi-frequency $\Omega_N = \sqrt{N}\Omega$, whereas the spatially separated atoms both feel an individual ac-Stark shift. The difference between those two can then be put in the form

$$V_{\text{eff}} = \langle -|H_{\text{TB}}|-\rangle = -\frac{1}{2}\left(|\Delta| + \sqrt{\Delta^2 + 2\Omega^2}\right) \approx -2|E_-| + \frac{\hbar\Omega^4}{|\Delta|^3}, \tag{2.10}$$

again in agreement with eq. (2.4). However, the dependence on the collective Rabi-frequency rises the question of what the small parameter in our perturbation actually is. Indeed, perturbation fails if the ratio of collective Rabi-frequency and detuning $\sqrt{N}\Omega/\Delta$ is too large. Since the number of atoms N inside the blockaded region can be expressed in terms of the atomic density n we find the dimensionless

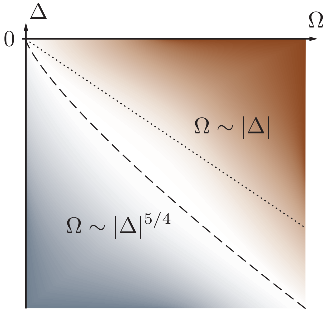

Figure 2.3: Crossover from two-body interaction to the regime with collective many-body interaction. The cross-over line scales like $\Delta \sim -\Omega^{4/5}$ (dashed line) and preempts the onset of three-body interactions that scales like $\Omega \sim |\Delta|$ (dotted line).

parameter $nf\xi_0^3$. In turn, perturbation holds provided that

$$nf\xi_0^3 \ll 1. \tag{2.11}$$

In order to get a more intuitive interpretation of this condition, consider the defining length-scales of the system: As long as $nf\xi_0^3 \ll 1$ the two-body blockade radius ξ_0 is much smaller than the distance $(nf)^{-1/3}$ between Rydberg-excitations and, in turn, perturbation theory holds. Conversely, for $nf\xi_0^3 \gg 1$, the blockaded regions overlap, and the atoms interact in a collective fashion. If we now compare this transition with the onset of three-body interactions we find that those are suppressed by a factor of $\Omega/|\Delta|$, which yields the scaling law $|\Delta| \sim \Omega$. On the other hand, by using the approximate expressions for the Rydberg fraction provided earlier we obtain the expression

$$|\Delta| \sim \left(\frac{C_6 n^2}{2\hbar}\right)^{\frac{1}{5}} \Omega^{4/5}, \tag{2.12}$$

for the transition into the collective regime. The fact of the matter is that the latter transition occurs before three-body interactions play any significant role. Hence the systems translates directly from a regime dominated by two-body interactions into the collective regime.

2.4 Mean-Field/Variational Approach

In the following, we derive an effective model for the collective interaction between Rydberg-dressed atoms. The general idea goes as follows: We assume the external potentials to vary only on length-scales much larger than the two-body blockade-radius ξ_0, and allows for a coarse grained particle distribution in terms of a local density n. The system can hence be described within a generalized Gross-Pitaevskii equation

$$i\hbar\partial_t\psi(t,\mathbf{x}) = \Big[H_0 + g_{\mathrm{s}}n(t,\mathbf{x}) + \partial_n E_{\mathrm{RD}}\left[n(t,\mathbf{x})\right]\Big]\psi(t,\mathbf{x}), \tag{2.13}$$

where $\psi(t,\mathbf{x})$ is the macroscopic condensate wave-function with $n(t,\mathbf{x}) = |\psi(t,\mathbf{x})|^2$ and g_{s} describes the background contact-interaction between the atoms. Further, $H_0 = -\hbar^2\nabla^2/2m + V_{\mathrm{ext}} - \mu$ is the non-interacting Hamiltonian for the external degrees of freedom, V_{ext} the external trapping potential, m the particle mass, and μ the chemical potential. Last, the internal energy $E_{\mathrm{RD}}[n]$ accounts for the interaction induced via Rydberg-dressing and is governed by the eigenvalues of the microscopic Hamiltonian (2.1). Here it is convenient to use a dimensionless form of the microscopic Hamiltonian, namely

$$H = 2|E_-|\left[\sum_i S_x^i \sin\phi + S_z^i\cos\phi + \xi_0^6 \sum_{j\neq i}\frac{P^iP^j}{|\mathbf{x}_i - \mathbf{x}_j|^6}\right], \tag{2.14}$$

with the angular parameter ϕ defined via

$$\Delta = -2|E_-|\cos\phi, \quad \Omega = 2|E_-|\sin\phi. \tag{2.15}$$

Since the internal energy-functional is highly nontrivial, we approximate $E_{\mathrm{RD}}[n]$ via an effective interaction-energy-functional $E_{\mathrm{eff}}[n] \approx E_{\mathrm{RD}}[n]$ determined within a variational mean-field approach, and thereby obtain an effective model for the collective interaction due to Rydberg-dressing. The details of this particular approximation procedure are described in the next subsection.

2.4.1 Variational Ansatz

In contrast to the mean-field approach used to describe phase transitions [53], the blockade-mechanism requires a more general treatment due to strong correlations in between excitations. A variational wave-function that allows us to include strong correlations can be written in the general form

$$|\text{var}\rangle = \frac{1}{\mathcal{N}} \sum_{s_1,\ldots,s_N} \left[\prod_{i\neq j} C_{s_i,s_j}(\mathbf{x}_i - \mathbf{x}_j) \right] |s_1 \ldots s_N\rangle. \tag{2.16}$$

Here, the $s_i \in \{g, r\}$ describe the state of the i-th atom, while the $C_{s,s'}$ account for short-range correlations between the atoms. Note that this ansatz is in close analogy to a paramagnetic phase in a spin-model, with all spins aligned along the $\langle \mathbf{s} \rangle$ direction.

It is instructive to consider the non-interacting case first: In the absence of interactions, the short-range correlations $C_{s,s'}$ factorize like $C_{s,s'} = \zeta_s \zeta_{s'}$, with $\zeta_g = \cos\theta$ and $\zeta_r = \sin\theta$, respectively. In consequence, the spin operator expectation-values take the form

$$\langle S_z \rangle = \frac{1}{2}\cos 2\theta = \frac{1}{2} - f, \quad \langle S_x \rangle = -\frac{1}{2}\sin 2\theta = -\sqrt{f(1-f)}, \tag{2.17}$$

where $f = \sin^2\theta$ is the probability for an atom to be in the Rydberg-state. As a first test for our variational wave-function, we calculate the ground state energy of a single atom interacting with the driving light-field. Upon minimization with respect to the Rydberg-fraction f we obtain the variational ground-state energy

$$\langle \text{var}|H_{\text{micro}}|\text{var}\rangle = E_-. \tag{2.18}$$

in agreement with the exact diagonalization of the single-atom Hamiltonian (2.1).

We now turn towards describing the interaction-part of the Hamiltonian (2.14), which we denote as H_{Ryd}, in terms of a variational problem. To do so, we follow ref. [43] and introduce the pair correlation-function g_2

$$g_2 = \frac{\langle P^i P^j \rangle}{f^2}, \tag{2.19}$$

in order to account for correlations between the Rydberg-excitations. For small inter-atom separation x, the blockade-mechanism prevents the simultaneous excitation of both atoms and yields a vanishing expectation-value $\langle P^i P^j \rangle \approx 0$. Conversely, for large inter-atom separation, interactions and hence correlations vanish and the expectation value of the correlation function factorizes like in the non-interacting case, $\langle P^i P^j \rangle \approx \langle P^i \rangle \langle P^j \rangle = f^2$. We therefore expect the correlation-function g_2 to vanish identically at small distances, whereas it approaches unity at large ones. As is shown in ref. [54], the transition between the two regimes is very sharp. We can hence define a characteristic correlation-length ξ marking the transition between those two regimes and use it as a second variational parameter. Moreover, the variation of ξ allows for the use of the variational ansatz (2.16) without precise knowledge of the short-range correlations $C_{s,s'}$. Next, due to the large number of atoms inside a blockade-volume $\xi_0^3 n \gg 1$, we can replace the summation over surrounding particles by an integration, so that

$$\sum_i \to n \int d^3x. \tag{2.20}$$

It follows that the energy expectation-value of H_{Ryd} expressed in terms of the correlation-function (2.19) and the local density n takes the form

$$\begin{aligned} \langle \text{var}|H_{\text{Ryd}}|\text{var}\rangle &\approx 2|E_-| \int d^3x \int d^3x' \, n^2 f^2 \xi_0^6 \, \frac{g_2(x)}{x^6} \\ &= 2|E_-| \int d^3x \, \frac{4\pi \, n^2 f^2 \xi_0^6}{\xi^3} \int_0^\infty dz \, \frac{g_2(z\xi)}{z^4}, \end{aligned} \tag{2.21}$$

where we have assumed a spherical symmetry of the correlation-function g_2. Rescaling of the spatial coordinate $x = z\xi$ reduces the last integral containing the correlation-function g_2 to a purely numerical constant,

$$2\pi \int dz \, \frac{g_2(z\xi)}{z^4} = Y. \tag{2.22}$$

A change in local form of g_2 yields but a different numerical constant Y, and ultimately a renormalization of the van der Waals coupling constant C_6. Even so, precise knowledge about the explicit form of g_2 is not important for our approch.

By use of the above results, the mean-field energy expectation-value for the interacting many-body system takes the form

$$\begin{aligned} &\langle \text{var}|H|\text{var}\rangle \\ &= 2|E_-| \int d^3x \left[n \left(f - \frac{1}{2} \right) \cos\phi - n \sqrt{f(1-f)} \sin\phi + 2Y \frac{n^2 f^2 \xi_0^6}{\xi^3} \right], \end{aligned} \tag{2.23}$$

Note that this expression still contains the ac-Stark shift due to the light-field, namely

$$E_{\mathrm{ac}} = nE_{-}, \tag{2.24}$$

which is present even in the non-interacting regime. Subtracting this energy shift from the variational energy then yields the effective energy $E_{\mathrm{eff}}[n]$ describing the collective interaction due to the Rydberg-dressing alone in terms of the variational problem

$$E_{\mathrm{eff}}[n] = \left[\min_{\{|\mathrm{var}\rangle\}} \langle \mathrm{var}|H|\mathrm{var}\rangle\right] - E_{\mathrm{ac}}. \tag{2.25}$$

The minimization with respect to the Rydberg-fraction f then follows the equation

$$\partial_f \langle \mathrm{var}|H|\mathrm{var}\rangle = 0, \tag{2.26}$$

and is equivalent to the self-consistency calculation used in ref. [43] to derive critical exponents at the quantum-critical point $\Delta = \Omega = 0$ (see appendix 2.D). On the other hand, the term accounting for the Rydberg-interaction always yields a positive contribution to the expectation-value $\langle \mathrm{var}|H|\mathrm{var}\rangle$. Since this is the only part that contains the correlation-length, it is hence minimized by maximizing the latter. Yet ξ itself is required to satisfy several constraints: First, for $nf\xi^3 \ll 1$

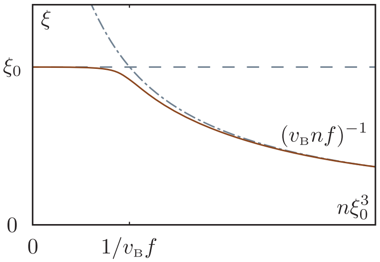

Figure 2.4: Constraints for the correlation-length ξ across the critical density. For $nf\xi_0^3 \ll 1$, correlations are bound by the two-particle blockade length ξ_0. In contrast, for $nf\xi_0^3 \gg 1$ the boundary is given by the distance between Rydberg-excitations $(nf)^{-1/3}$. The red line is a sketch for the expected behavior of the correlation-length.

with large average distances between Rydberg-excitations, correlations are limited by the two-body blockade-radius giving rise to the condition $\xi \leq \xi_0$. Second, for $nf\xi^3 \ll 1$ the characteristic distance between Rydberg-excitations provides a second length-scale that limits correlations. In particular, the normalization condition [43]

$$nf \int d^3x \, (1 - g_2(x)) = 1 \tag{2.27}$$

provides the upper bound $\xi \leq (v_{\mathrm{B}} nf)^{-1/3}$, where $v_{\mathrm{B}} = 4\pi \int dz (1 - g_2(z\xi))$ is the dimensionless blockade volume factor. Quite unfortunately, it remains a free parameter in the theory. Combining the above conditions, the upper bounds for the correlation-length ξ take the piecewise form

$$\xi^3 \leq \xi_0^3 \min \left[\frac{1}{nf v_{\mathrm{B}} \xi_0^3}, 1 \right]. \tag{2.28}$$

For the purpose of minimization, we expect the correlation-length ξ to take values close to this upper bound, with a smooth behavior in the transition region. Indeed, this criterion is consistent with our previous estimate (2.11).

In the low-density limit $nf\xi_0^3 \ll 1$, the variational energy (2.25) is required to reproduce the two-body interaction-parameter g_{eff} derived within the adiabatic Born-Oppenheimer approach (2.4), that is

$$g_{\mathrm{eff}} = \frac{\pi^2}{12} \frac{\hbar \Omega^4}{|\Delta|^3} \xi_0^3. \tag{2.29}$$

Note that the assumption $\Omega \leq \Omega_N \ll \Delta$ obscures the fact that the energy scale of the interaction parameter is proportional to the ac-Stark shift times the square of the Rydberg fraction, namely $g_{\mathrm{eff}} = 8\pi^2 |E_-| f^2 \xi_0^3 / 3$. On the other hand, the two-body interaction-parameter predicted by the variational energy E_{eff} is given by its second-order coefficient of the series-expansion in the atomic density n,

$$E_{\mathrm{eff}}[n] = \frac{4Y|E_-|}{\xi_0^3} n^2 f^2 \xi_0^6 = \frac{g_{\mathrm{var}}}{2} n^2. \tag{2.30}$$

For these two results to agree, it is thus necessary that

$$Y = \int dz \, \frac{g_2(\xi z)}{z^4} = \frac{\pi^2}{3} \approx 3.3. \tag{2.31}$$

As noted before, the parameter v_B cannot be calculated in the same fashion. Yet, under the assumption of a sharp transition between the correlated and uncorrelated regime used in ref. [43], the blockade-volume coefficient reduces to $v_\mathrm{B} = 4\pi/3$, which is the volume of a unit sphere. Yet, under the same assumption the coefficient Y would have taken the value $4\pi/3 \approx 4.2$. Since both results are on the same order of magnitude, this justifies the use of $v_\mathrm{B} = 4\pi/3$.

2.4.2 Rydberg Interaction Energy-Functional

In the deep collective regime with $nf\xi_0^3 \to \infty$, the last term in eq. (2.23) dominates. A leading-order expansion of the condition (2.26) in $1/f$ then yields the scaling behavior of the Rydberg-fraction

$$f \to \left(\frac{(3/4\pi)^2 \sin\phi}{\pi \xi_0^6 n^2} \right)^{\frac{2}{5}}, \tag{2.32}$$

and, in consequence, the Rydberg-fraction goes to zero or $n\xi_0^3 \to \infty$. Accordingly, the effective interaction energy takes the form of a chemical potential, namely

$$E_\mathrm{eff}[n] = 2|E_\mathrm{ac}| \sin^2 \frac{\phi}{2} = n\mu_\mathrm{sat}. \tag{2.33}$$

In particular, the variational interaction-potential $\partial_n E_\mathrm{eff}[n]$ in the deep collective regime is independent of the atomic density, and renders the atoms basically free. This rather counterintuitive behavior is due to the fact that for $nf\xi_0^3 \to \infty$, the number of atoms inside a blockade volume diverges like $n\xi^3 \approx 1/f \sim n^{4/5} \to \infty$. As a result, all atoms in the ensemble up to a non-extensive part are within the blocked region and thereby cannot acquire a Rydberg-dressing, which prevents them to interact via the van der Waals channel. On the other hand, the energy difference between the single-atom and the collective ac-Stark shift leads to a shift in the chemical potential, and explains as to why μ_sat is independent of the van der Waals interaction-energy $C_6 n^2$. Even so, according to eq. (2.32), the total number of Rydberg-excitations $nf \sim n^{1/5}$ still grows with increasing atomic density. The same is true for the internal energy $E_\mathrm{eff}[n] = \mu_\mathrm{sat} n$, which depends linearly on the atomic density n.

In order to get some intuition on what to expect from the general minimization, we make the curdest of estimates imaginable: In the limit $nf\xi_0^3 \ll 1$, the interaction-energy is due to the two-body processes and gives rise to a linear growth of the

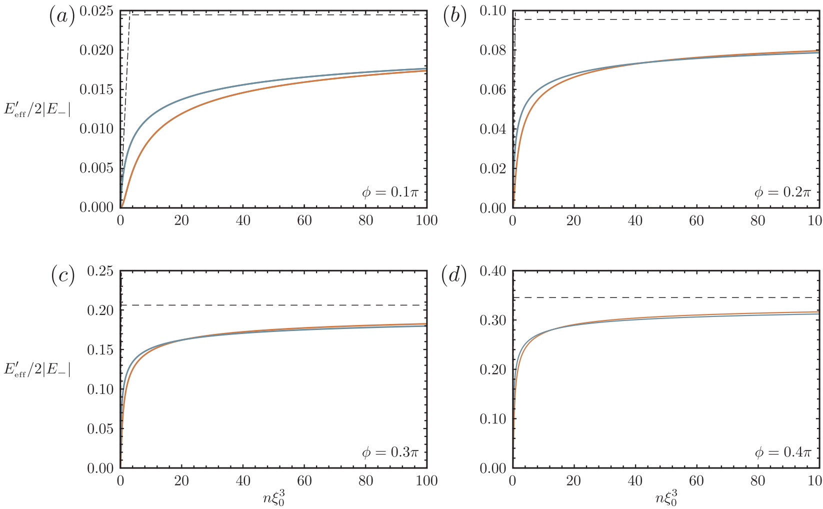

Figure 2.5: Numerical results for the effective interaction-potential $\partial_n E_{\text{eff}}[n]$ for different parameters ϕ. The solid blue line is the minimization-result in the two-body regime with $\xi \approx \xi_0$, whereas the solid orange line is for the collective regime with $\xi \approx (nf)^{-1/3}$. The dashed and dotted lines account for the two-body and deep collective limit of the interaction. Although we used the sharp transition (2.28) for the correlations, the transition between the two regimes is surprisingly smooth.

variational interaction-potential $\partial_n E_{\text{eff}}[n] \approx g_{\text{eff}} n$. On the other hand, the variational interaction-potential saturates at $\partial_n E_{\text{eff}}[n] \approx \mu_{\text{sat}}$ For $nf\xi_0^3 \gg 1$. If we neglect the intermediate region for the time being, we can estimate the variational interaction-potential via

$$\partial_n E_{\text{eff}}[n] = 2|E_-| \min \left[\frac{4\pi^2}{3} \left(\frac{\phi}{2} \right)^4 n\xi_0^3, \sin^2 \frac{\phi}{2} \right]. \tag{2.34}$$

The transition between the two-body and the deep collective regime then takes place at the transition-density n_{t} defined via

$$n_{\text{t}}\xi_0^3 = \frac{3}{4\pi^2} \frac{\sin^2 \phi/2}{(\phi/2)^4}. \tag{2.35}$$

For a fixed angle ϕ, the right hand side of eq. (2.35) is constant, and we are left with a scaling $n_{\mathrm{t}}\xi_0^3 = \sqrt{C_6 n_{\mathrm{t}}^2/4|E_-|}$. Again, this can be interpreted as a competition between the van der Waals energy $C_6 n_{\mathrm{t}}^2$ and the ac-Stark shift E_- and is in rough agreement with the estimate (2.12). The major difference is that eq. (2.34) predicts an applicability of two-body scattering even in the critical region $\Delta = 0$. Yet this comes to no surprise, since eq. (2.12) marks the breakdown of the two-body regime, whereas eq. (2.35) yields the point where two-body and collective interaction result in the same energy.

Unfortunately, there is no general analytic solution for the variational problem (2.25) in the intermediate regime. Still, simple numerics allow us to derive the variational interaction-energy $E_{\mathrm{eff}}[n]$ for arbitrary atomic densities n. For the following calculation, we use a sharp transition between the two-body and collective regime according to eq. (2.28). In consequence, the energy-functional shows a discontinuity in the second derivative at $nf\xi_0^3 v_{\mathrm{B}} = 1$. Although eq. (2.28) is an unphysical approximation, it yields an effective energy-functional E_{eff} that is surprisingly well-behaved (see Fig. 2.5) and shows a very broad crossover between the two-body and the collective regime: Deviations occur already at densities as low as $n\xi_0^3 \approx 0.05$. Conversely, its saturation is very slow, and convergence can only be seen on a logarithmic scale. This gives rise to a wide collective regime, in which the interaction-energy depends nontrivially on the local density n.

2.5 Wave-Function in Thomas-Fermi Approximation

In the Tomas-Fermi approximation [4], the kinetic energy of the particles is assumed to be negligible as compared to the interaction-energy, either due to the external trapping-potential V_{trap} or due to the interaction between atoms. Thereby the Gross-Pitaevskii differential equation (2.13) reduces to a transcendental equation

$$0 = \Big[V_{\mathrm{ext}} - \mu + g_{\mathrm{s}} n(t,\mathbf{x}) + \partial_n E_{\mathrm{eff}}\left[n(t,\mathbf{x})\right]\Big]\psi(t,\mathbf{x}), \tag{2.36}$$

and allows for a simple solution with respect to the local density $n(\mathbf{x}) = |\psi(\mathbf{x})|^2$. In combination with the knowledge of the internal interaction-energy $E_{\mathrm{eff}}[n]$, we are now able to derive the density-profile for a Bose-Einstein condensate in an external trapping-potential V_{ext}. In the two-body regime the internal energy takes the form $E_{\mathrm{eff}} \approx g_{\mathrm{eff}} n^2/2 + \mathcal{O}(n^3)$ and gives rise to a normalized s-wave scattering parameter. In turn, the density-profile follows the external potential $n \approx V_{\mathrm{ext}}/(g_{\mathrm{eff}} + g_{\mathrm{s}})$, and

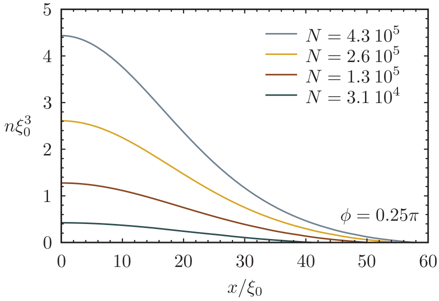

Figure 2.6: Thomas-Fermi Density profile for a ^{87}Rb atoms in a harmonic trap with trap frequency $\omega_{\mathrm{trap}} = 20$ Hz under Rydberg-dressing and background scattering-length $a_{\mathrm{s}} = 5.7$ nm. For increasing atom-numbers we find an accumulation in the center of the harmonic trap.

results in the famous inverted parabola density-profile for a harmonic trapping potential $V_{\mathrm{trap}} = m\omega_{\mathrm{trap}}^2 x^2/2$ [4]. In the deep collective regime, both the internal interaction-energy and the energy due to the trapping potential increase linearly with the particle-density. Hence, the energy for adding an additional particle does no longer depend on the local density, but only on its position due to the spatial dependence of the trapping potential. For a harmonic trap, this yields an accumulation of particles in its center. Even so, the remaining interaction between

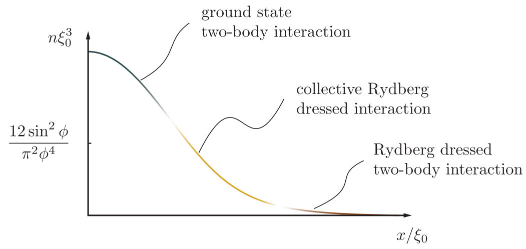

Figure 2.7: Sketch for the different interaction-regimes in the Thomas-Fermi density-profile. For low densities, two-body interaction between the Rydberg dressed atoms dominates. Then, for increasing densities, the system enters the collective regime. Eventually, the interaction-potential for the Rydberg dressed atoms saturates, and two-body interaction between ground state atoms dominates again.

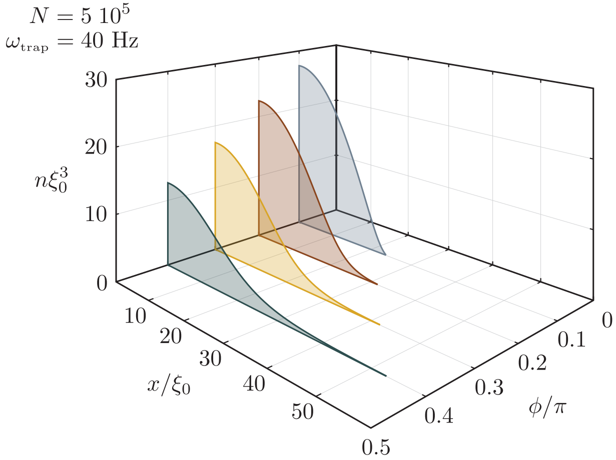

Figure 2.8: Density profile for a Bose-Einstein condensate of ^{87}Rb atoms in a harmonic trap with trap frequency $\omega_{\text{trap}} = 40$ Hz and background scattering length $a_s = 5.7$ nm for $\phi/\pi = 0.1 - 0.4$. For small ϕ, the background scattering dominates, and leads to an inverted-parabola density-profile. In contrast, for large $\phi \approx \pi/2$ the density-profile is more *Gaussian-like* due the collective Rydberg-interaction.

the ground-state atoms prevents the system from collapsing. Instead of an unstable region, we again find a parabolic wave-function with its length-scale governed by the background s-wave scattering length.

2.6 Conclusion

In chapter 2 we have shown that an atomic ensemble dressed with a Rydberg state exhibits long-range interactions that can be tuned to orders of magnitude larger than the s-wave scattering length between ground state atoms. For strong long-range interactions, one usually expects higher orders of the interaction to contribute significantly to the inter-particle interaction-potential. Yet, we have found that the onset three-body interactions associated with the breakdown of the first Born approximation is preempted by a transition into a collective regime, where all orders of the interaction need to be taken into account. The latter is governed by the strong van der Waals interaction between Rydberg atoms and gives rise to a highly correlated state. However, the excitation blockade due to this strong interaction prevents simultaneous excitation of spatially close atoms, and hence reduces the losses such a long-range interaction would suggest.

We showed that such a system can be treated within a variational/mean-field approach, and explicitly calculated the effective interaction-potential between the atoms in a generalized Gross-Pitaevskii energy functional. In turn, we derived the effective interaction energy from the microscopic Hamiltonian describing the ensemble of coherently driven atoms with interacting excited states. For $nf\xi_0^3 \ll 1$, the resulting effective interaction-potential reproduced the two-body interactions in agreement with the first Born-Oppenheimer results, whereas it saturated for large atom densities. This nonlinear behavior is based on the fact that the blockade mechanism limits the number of Rydberg-excitations the ensemble is able to support: Although the number of Rydberg-excitations increases with increasing atom density, we have found that the ratio between excitations and the number of atoms goes to zero for $nf\xi_0^3 \gg 1$ and renders the atoms basically free. Of course, this leads to severe consequences for the shape of the condensate wavefunction: Rather than the inverted Thomas-Fermi parabola we have found that the cloud takes a more *Gaussian-like* form. We have discussed this change for different parameter sets, and have provided experimental parameters for which we expect these effects to occur in current experimental setups.

2.A Suppression of the intermediate state via EIT

In this section we comment on the elimination of the intermediate p-state via electromagnetically induced transparency (EIT). It is instructive to consider a single atom first, before moving on to the full two-body Hamiltonian. In analogy to the far off-resonant coupling we consider a system in which the ground state $|g\rangle$ is coupled to the Rydberg-state $|r\rangle$ via an intermediate state $|p\rangle$. The Rabi frequencies driving the transition from the ground- to the p-state and the p- to the Rydberg-state are denoted Ω_r and Ω_p, respectively. Moreover, the Rydberg state is in two-photon resonance, $\Delta = 0$, so that both ground- and Rydberg state have zero energy in the rotating frame, and the intermediate state is blue-detuned with a detuning $\Delta_p > 0$. The eigenstates and eigenvalues for a single atom interacting

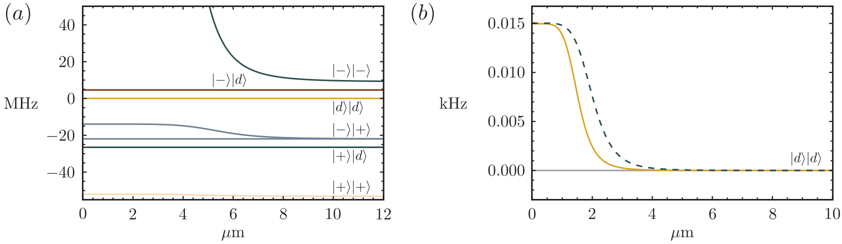

Figure 2.9: (a) Eigenvalues of the two-body EIT Hamiltonian as a function of the relative distance x between the atoms. The plot is for atoms in the ^{87}Rb $|43s\rangle$ state, with a red Rabi-frequency $\Omega_r = 0.7$ MHz, a blue Rabi-frequancy $\Omega_r = 22$ MHz and a blue detuning $\Delta_p = 22$ MHz from the intermediate state $|p\rangle$. Moreover, the van der Waals interaction coefficient is $C_6 = 189$ Mhzμm^6. Note that the energy scale of the induced interaction is not visible in (a). (b) Comparison between the numerical diagonalization and the Born Oppenheimer interaction-potential.

with this particular light-field can be calculated analytically, and take the form

$$
\begin{aligned}
|\pm\rangle &= \frac{\Omega_r}{\sqrt{\Omega_r^2 + \Omega_b^2 + 4E_\pm^2}}|g\rangle + \frac{\pm 2E_\pm}{\sqrt{\Omega_r^2 + \Omega_b^2 + 4E_\pm^2}}|p\rangle + \frac{\Omega_b}{\sqrt{\Omega_r^2 + \Omega_b^2 + 4E_\pm^2}}|r\rangle, \\
|d\rangle &= \frac{\Omega_b}{\sqrt{\Omega_r^2 + \Omega_b^2}}|g\rangle - \frac{\Omega_r}{\sqrt{\Omega_r^2 + \Omega_b^2}}|r\rangle,
\end{aligned}
$$

with eigenenergies $E_\pm = \frac{1}{2}\left(\pm\Delta + \sqrt{\Delta^2 + \Omega_r^2 + \Omega_b^2}\right)$ and $E_d = 0$, respectively. The state $|d\rangle$ corresponding to the eigenvalue $E_d = 0$ is a dark state that no longer couples to the light field. The important point is that it does not contain any contribution of the intermediate p-state. Therefore, the decay is solely governed by the probability of the atom to be in the Rydberg state, i.e.

$$
f = \frac{\Omega_r^2}{\Omega_r^2 + \Omega_b^2}. \tag{2.37}
$$

To limit this population, we choose a weak red coupling laser $\Omega_r \ll \Omega_b$, so that the effective decay rate reduces to

$$
\Gamma = \frac{\Omega_r^2}{\Omega_b^2}\Gamma_r, \tag{2.38}
$$

where we used $\Omega_r^2 + \Omega_b^2 \approx \Omega_b^2$. In order to find the exact interaction potential between the dark states, one has to solve the full two-body Hamiltonian. A matrix representation of this particular Hamiltonian in the basis

$$\{|g,g\rangle, |p,g\rangle, |g,p\rangle, |r,g\rangle, |g,r\rangle, |p,p\rangle, |r,p\rangle, |p,r\rangle, |r,r\rangle\}$$

reads

$$H = \begin{pmatrix} 0 & \Omega_r/2 & \Omega_r/2 & 0 & 0 & 0 & 0 & 0 & 0 \\ \Omega_r/2 & \Delta_p & 0 & \Omega_b/2 & 0 & \Omega_r/2 & 0 & 0 & 0 \\ \Omega_r/2 & 0 & \Delta_p & 0 & \Omega_b/2 & \Omega_r/2 & 0 & 0 & 0 \\ 0 & \Omega_b/2 & 0 & 0 & 0 & 0 & \Omega_r/2 & 0 & 0 \\ 0 & 0 & \Omega_b/2 & 0 & 0 & 0 & 0 & \Omega_r/2 & 0 \\ 0 & \Omega_r/2 & \Omega_r/2 & 0 & 0 & 2\Delta_p & \Omega_b/2 & \Omega_b/2 & 0 \\ 0 & 0 & 0 & \Omega_r/2 & 0 & \Omega_b/2 & \Delta_p & 0 & \Omega_b/2 \\ 0 & 0 & 0 & 0 & \Omega_r/2 & \Omega_b/2 & 0 & \Delta_p & \Omega_b/2 \\ 0 & 0 & 0 & 0 & 0 & 0 & \Omega_b/2 & \Omega_b/2 & V \end{pmatrix}.$$

Numeric diagonalization of this matrix then yields the energy diagram as is shown in Fig. 2.9. Fulfilling our expectations, the induced van der Waals interaction between the Rydberg-dressed atoms saturates at small distances, with the saturation value given by

$$V_{\text{sat}} = \frac{\Omega_r^4}{4\Omega_b^2\Delta_p}. \tag{2.39}$$

This is exactly the light shift $\Omega_r^2/2\Delta$ experienced by a single atom, weighted with the probability $f = \Omega_r^2/\Omega_b^2$ to be in the Rydberg-state. The length-scale defining this transition takes the form

$$\xi_{\text{EIT}} = \left(\frac{2C_6\Delta}{\Omega_b^2}\right)^{1/6} \tag{2.40}$$

which reduces to $\xi_{\text{EIT}} = (2C_6/\Delta_p)^{1/6}$ for $\Delta_p = \Omega_b$. With the use of realistic experimental values like in 2.C, that is $C_6 = 189$ Mhzμm^6, $\Omega_b = \Delta_p = 22$ MHz and $\Omega_r = 0.7$ MHz, we can calculate the saturation of the induced energy potential to be $V_{\text{sat}} \approx 11.6$ Hz compared to 0.4 Hz in the far off-resonant case, while the two-body blockade radius is $\xi_0 \approx 1.61$ μm. The resulting s-wave scattering length is then $a_s \approx 200$ nm, and thus two orders of magnitude larger than in the far off-resonant case, in which $a_\mathrm{s} \approx 5$ nm.

2.B Generalized Gross-Pitaevskii Equation

The Gross-Pitaevskii equation generally used in describing a weakly-interacting Bose-Einstein condensate can be derived *from scratch* via the coherent state path integral formalism. There, the action of a general many-body system is given by

$$S[\phi^*, \phi] = \int_0^{\hbar\beta} d\tau \left[\sum_\alpha \phi_\alpha^*(\tau) \left(\hbar\partial_\tau - \mu\right) \phi_\alpha(\tau) + H\left(\{\phi_\alpha^*(\tau)\}, \{\phi_\alpha(\tau)\}\right) \right], \tag{2.41}$$

where we used imaginary time $\tau = -it$. The coherent state amplitudes are defined via

$$a_\alpha|\phi\rangle = \phi_\alpha|\phi\rangle, \quad |\phi\rangle = \exp\left(\sum_\alpha \phi_\alpha a_\alpha^\dagger\right)|0\rangle. \tag{2.42}$$

Here, we have the following system in mind: Every atom features a kinetic energy H_kin, and individually interacts with an external trapping potential V_ext. In addition, the atoms interact with each other via an arbitrary interaction-potential $E_\mathrm{int}[\phi^*, \phi]$, which we explicitly assume to contain arbitrary orders of ϕ^* and ϕ, respectively. However, since the action has to be of real value, the coherent state amplitudes only occur in the combination $\phi^*\phi$. Neglecting quantum fluctuations, minimization of the action requires that the variation of the action vanishes,

$$0 = \frac{\delta S[\phi^*, \phi]}{\delta\phi^*}. \tag{2.43}$$

Under the above assumptions, this reduces to

$$0 = \left[\sum_\alpha \phi_\alpha^*(\tau) \left(\hbar\partial_\tau - H_0\right) \phi_\alpha(\tau) + V_\mathrm{int}\left(\{\phi_\alpha^*(\tau)\phi_\alpha(\tau)\}\right) \right] \phi_\alpha(\tau), \tag{2.44}$$

where $H_0 = H_\mathrm{kin} + V_\mathrm{ext} - \mu$ and $V_\mathrm{int}(n) = \partial_n E_\mathrm{int}(n)$ is the derivative of the inter-atom interaction-energy with respect to the density.

2.C Optimization of Experimental Parameters

In this section, we provide a scheme for maximizing the induced s-wave scattering-length for the Rydberg-dressed interaction. First, the effective decay-rate γ_{eff} is governed by the decay-rates from the Rydberg-state γ_r and the intermediate p-state γ_p, via

$$\gamma_{\text{eff}} = \frac{\Omega_p^2}{4\Delta_p^2}\left(\gamma_p + \frac{\Omega_r^2}{4\Delta^2}\gamma_r\right). \tag{2.45}$$

The ratios $(\Omega/\Delta)^2$ and $(\Omega_p/\Delta_p)^2$ are the population of the Rydberg- and the p-state in the weak-dressing limit. This allows us to express the population of the p-state $\Omega_p/2\Delta_p$ in the expression for the two-photon Rabi-frequency

$$\Omega = \frac{\Omega_r}{2}\frac{\Omega_p}{|\Delta_p|} = \frac{\Omega_r}{2}2\sqrt{\frac{\gamma_{\text{eff}}\Delta^2}{\gamma_p\Delta^2 + \Omega_r^2\gamma_r/4}} \tag{2.46}$$

in terms of the total detuning Δ and the Rabi-frequency Ω_r driving the transition $|p\rangle \to |r\rangle$ together with the effective decay-rate γ_{eff}. Then, the two-body interaction-parameter reduces to

$$g_{\text{eff}} = \frac{\pi^2}{12}\sqrt{\frac{C_6}{2}}\frac{\sqrt{|\Delta|}\Omega_r^2\gamma^2}{(\gamma_p\Delta^2 + \Omega_r^2\gamma_r/4)^2}. \tag{2.47}$$

Since the effective decay-rate γ_{eff} is limited by experimental requirements and, likewise, the Rabi-frequency Ω_r by the available laser power, the only remaining parameter left is the total detuning Δ. Optimization with respect to Δ yields the optimal detuning $\Delta_{\text{o}} = -|\Omega_r|\sqrt{\gamma_r/28\gamma_p}$, and, as a result, gives rise to the optimal s-wave scattering-length

$$a_{\text{eff}} = \frac{m}{4\pi\hbar^2}g_{\text{eff}}[\Delta_{\text{o}}] = \frac{m}{4\pi\hbar^2}\frac{49\pi^2}{48}\sqrt{\frac{C_6}{2}}\frac{\gamma^2}{\gamma_r^2}\left(\frac{\Omega_r^2\gamma_r}{28\gamma_p}\right)^{1/4}. \tag{2.48}$$

More specifically, in a setup of Rubidium atoms weakly-dressed with a Rydberg-state $|r\rangle = |35s\rangle$, Rabi-frequencies of $\Omega_r = 22$ MHz have been reached. Further, an effective decay-rate $\gamma_{\text{eff}} = 6$ Hz is sufficient for a fast experiment. Together with the decay-rates $\gamma_r = 4$ kHz and $\gamma_p = 6$ MHz and the van der Waals interaction-parameter $C_6 = 189$ Mhzμm^6, the s-wave scattering-length reduces to $a_{\text{eff}} = 49.5$ nm. Note that this is an order of magnitude larger than the s-wave

$\lvert\Omega_c\rvert$	$\lvert\Omega_p/\Delta_p\rvert = \sqrt{\gamma/2\gamma_p}$	Ω	$\Omega/\Delta_c = \sqrt{7\gamma/2\gamma_r}$
107 kHz	$7.8 10^{-4}$	7.8 kHz	0.072

Table 2.1: Optimal parameters for s-wave scattering.

scattering-length of an undressed Rubidium atom, namely $a_\mathrm{s} = 5.7$ nm. In addition, other system parameters are given in Table 2.1.

2.D Connection to Universal Scaling Results

At the quantum critical point $\Delta = \Omega = 0$ the Rydberg-fraction f follows an algebraic scaling-law that can be derived in a mean-field approach [43]. Here we show that our eq. (2.28) which determines the Rydberg-fraction in the variational ansatz yields the same critical exponents. To that means we consider the deep collective regime in which the correlation-function takes the form $\xi^3 = 1/v_\mathrm{B} n f$. Hence, eq. (2.28) takes the form

$$\partial_f \langle \mathrm{var}|H|\mathrm{var}\rangle = 2|E_\mathrm{ac}| \left[\cos\phi - \frac{\frac{1}{2} - f}{\sqrt{f(1-f)}} \sin\phi + 4 v_\mathrm{B} Y \xi_0^6 n^2 f^2 \right] = 0. \quad (2.49)$$

Here it is important to note that we have to evaluate the derivative with respect to f first, and then insert the specific expression for the correlation-function, which thus acts as a Lagrange parameter. In analogy to ref. [43], we now consider the scaling of the Rydberg-fraction in the classical regime in which $\Omega = 0$ as well as in the quantum regime with $\Delta = 0$. First, for $\Omega = 0$ the second term of eq. (2.49) vanishes, and we are thus left with

$$f^2 = \frac{9}{16\pi^3} \frac{1}{\pi^3 n^2 \xi_0^6}. \quad (2.50)$$

Since the first term in eq. (2.50) is always positive, this equation can only be solved for positive detuning Δ. Conversely, for negative detuning, the energy expectation-value (2.23) minimizes for vanishing Rydberg-fraction $f = 0$. To put it another way, the Rydberg-fraction in the classical model is zero for negative detunings Δ, and takes a finite value as soon as the detuning turns positive. Directly at the quantum critical point $\Delta = \Omega = 0$, the Rydberg-fraction scales as

$f \approx (2|E_-|/C_6 n^2)^{1/2}$, which gives rise to the critical exponent $\nu = 1/2$, predicted in ref. [43]. Second, in the quantum regime $\Delta = 0$, the first term in eq. (2.49) vanishes. The resulting minimization condition then takes the form

$$-\frac{\frac{1}{2} - f}{\sqrt{f(1-f)}} \sin\phi + 4 v_{\mathrm{B}} Y \xi_0^6 n^2 f^2 = 0. \tag{2.51}$$

Although a solution always exists due to the negativity of the first term eq. (2.51), the solution cannot be cast in a closed-form expression. Still a leading-order series expansion in $1/f$ yields

$$-\frac{1}{2\sqrt{f}} \sin\phi + 4 v_{\mathrm{B}} Y \xi_0^6 n^2 f^2 = 0, \tag{2.52}$$

and gives rise to the scaling law $f \approx (2|E_-|/C_6 n^2)^{2/5}$. Explicitly, the critical exponent turns out to be $\mu = 2/5$ in agreement with ref. [43].

Chapter 3

Deterministic Single-Photon Subtraction from Arbitrary Light Fields

3.1 Motivation

Photons are a prime candidate for carrying quantum-information due to their weak interaction with atomic systems. Yet, these weak interactions render them difficult to control on a quantum level and require for novel schemes to efficiently couple light and matter. On the other hand, since artificial atoms often show strong optical non-linearities even for weak light-fields, as well as an enhanced photon-coupling [55–57], they offer new possibilities to implement quantum-networks mediated by photons.

The main building blocks for this type of quantum information processing are photon-sources, conditional quantum-gates, and photon-detectors. In a seminal work, Saffmann and Walker [58] proposed to exploit the blockade-mechanism in order for the deterministic generation of single photons. Their design is based on the fact that an ensemble of atoms excited to the Rydberg-state can carry but a single excitation. Implementing such a collective excitation into a four-wave mixing scheme allows for the creation of a super-radiant Dicke-state [59]. In turn, the phase imprinted via four-wave mixing gives rise to a highly directional emission, which is paramount for photonic communication.

The second building block, that is an efficient photonic phase-gate, was demonstrated by Gorshkov et al. [60] in 2011. There, a photon in an optically thick atomic ensemble is converted into a dark-state polariton carrying a single Rydberg excitation. Due to the dipole-dipole interaction between Rydberg atoms a second photon in the atomic ensemble cannot form a polariton state, and, as a result, travels at the speed of light through the blockade-region. The difference in the propagation-velocity between the polariton and the bare photon then yields a phase shift in the two-photon wave-function that can be used to implement a conditional phase-gate. This concept was later generalized by Shahmoon et al. [61] to photons coupled to different Rydberg-states, where an external field induces resonant dipole-dipole interactions.

In this chapter, we present a design for a high-fidelity measurement of individual photons, and represents the last element for efficient quantum-information. The absorption-probability of a single two-state system is quite low and can only be enhanced by precise control over the photon to be absorbed: A π-pulse and its analogue on the single photon level [62] can coherently excite a single atom. Likewise, a stimulated Raman adiabatic passage (STIRAP) as used in ref. [63] allows for a coherent population transfer into an excited state, but needs control over the arrival-time of the probe-field.

Here, we show that a controlled dephasing of individual excited states in an atomic ensemble in combination with excitation-blockade provided by strong interactions yields an enhanced absorption probability that reaches unity in the limit of an infinite number of atoms. Henceforth, we concentrate on the realization based on Rydberg-blockade extensively studied in the past [38–41,64,65]. Yet, an analogous blockade phenomenon occurs for strongly confined quantum-dots, where the interaction between excitons blocks a subsequent excitation [66], and might be used to realise our design within a solid-state system. In addition, we show applications of this setup for a single-photon transistor, a high fidelity n-photon detector, and a scheme for the deterministic creation of non-classical states of light via photon-subtraction.

3.2 Model for a Deterministic Single-Photon Absorber

In order to absorb a single photon, we need a system that can carry exactly one excitation. Here, we consider an ensemble of atoms, in which each atom can be excited into a Rydberg-state via a two-photon process (see Fig. 3.2): a strong control laser with Rabi-frequency Ω_c and detuning $\Delta_c \gg \Omega_c$ couples the Rydberg-state

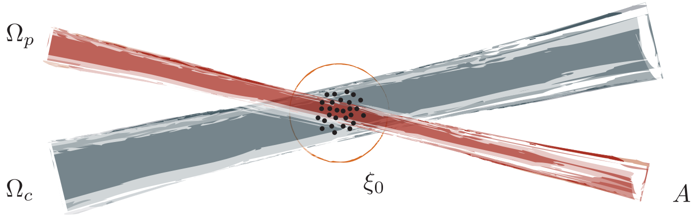

Figure 3.1: Sketch of the single-photon absorber setup: The red beam with Rabi-frequency Ω_p is the weak probe field pulse, whereas the blue control beam with Rabi-frequency Ω_b accounts for both driving of the system as well as the controlled dephasing. The transverse mode volume A of the probe beam is set to be smaller than the extent of atomic ensemble, the latter indicated by the black dots. Moreover, we consider an ensemble that is smaller than a single blockade-radius ξ_0 in order to ensure that the system can support but a single excitation.

$|r\rangle$ to an intermediate state $|p\rangle$, while the transition from ground-state $|g\rangle$ to the p-state is driven by a weak probe-field with Rabi-frequency Ω_p. The detuning of the control and probe-laser is chosen such that the transition from ground- to Rydberg-state is on two-photon resonance, that is $\Delta_p \approx -\Delta_c$. For large detuning from the intermediate p-state, such a three-state system can be reduced to an effective two-state system, giving rise to the two-photon Rabi-frequency $\Omega = \Omega_c \Omega_p / 4\Delta_c$ [51] (see Fig. 3.2). It is important to keep in mind that, despite the description via the single Rabi-frequency Ω, this is actually a two-photon process, as it is a photon from the probe-field we intent to absorb. Therefore, we additionally require the probe beam to be strongly focussed with a transverse mode area A smaller than the size of the transverse trapping of the atomic ensemble (see Fig. 3.1). In the frozen Rydberg-gas approximation [52], the dynamics of an ensemble of strongly interacting Rydberg atoms reduces to the coherent dynamic of a single *super-atom* consisting of a collective ground-state $|G\rangle$ and a collective excited state $|W\rangle$, driven by the collective Rabi-frequency $\Omega_N = \sqrt{N}\Omega$ (see appendix 6.A.4). Accordingly, the Hamiltonian for the atomic ensemble takes the form of an effective two-state system,

$$H_{\text{coh}} = \frac{\hbar \Omega_N}{2} \Big[|W\rangle\langle G| + |G\rangle\langle W| \Big], \tag{3.1}$$

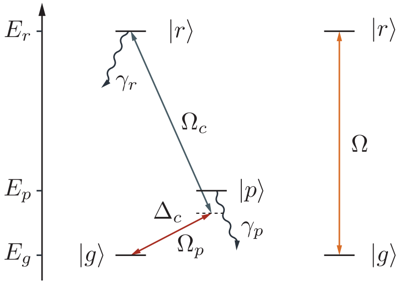

Figure 3.2: Laser configuration for the individual atoms: The ground-state is resonantly coupled to the Rydberg-state via a two-photon process. This is achieved by a weak probe beam with Rabi-frequency Ω_p coupling the ground-state $|g\rangle$ to the intermediate state $|p\rangle$, and a second strong control beam with Rabi-frequency Ω_c coupling the intermediate state to the Rydberg-state $|r\rangle$. In turn, the intermediate state is far detuned, i.e. $\Delta_c \gg \Omega_c$, and allows the reduction to an effective two-state system with two-photon Rabi-frequency $\Omega = \Omega_c\Omega_p/4\Delta_c$.

with collective ground and excited state

$$|G\rangle = \otimes_i |g_i\rangle, \quad |W\rangle = \frac{1}{\sqrt{N}} \sum_i |i\rangle, \tag{3.2}$$

where $|i\rangle = |e_i\rangle \otimes_{j\neq i} |g_j\rangle$ describes a state with an excitation in the i-th atom.

3.2.1 Breaking an Artificial Atom via Noise

The basis of our scheme is the following: The dynamics of a general ensemble of N two-state atoms is described within a 2^N-dimensional Hilbert-space. Even so, the blockade-mechanism only allows for a single excitation in the ensemble, and hence reduces the Hilbert-space dimension to $N+1$. On the other hand, the light-field drives a transition from the collective ground-state $|G\rangle$ to the coherent superposition of excited states $|W\rangle$. This induces a natural decomposition of the Hilbert-space into a bright and dark subspace $\mathcal{B}$ and $\mathcal{D}$, respectively, where only the two-dimensional bright subspace $\mathcal{B}$ couples to the driving light-field. In contrast to the first reduction of the Hilbert-space dimensionality, which is based on an energy argument, the second one is but due to the nature of the light-field coupling, and

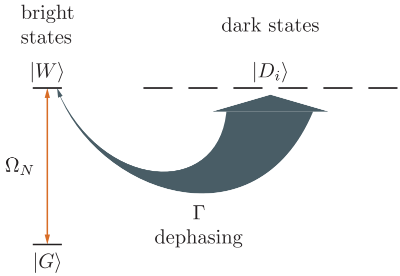

Figure 3.3: Coupling to the dark states via controlled dephasing: The system gives rise to a *super-atom* state $|W\rangle$ with a single Rydberg-excitation shared among the atoms and coupled with collective Rabi-frequency $\Omega_N = \sqrt{N}\Omega$. In addition, the system exhibits $N-1$ dark states $|D_j\rangle$, which are coupled to the *super-atom* state via controlled inhomogeneous dephasing with a characteristic rate Γ.

thus can easily be broken by a secondary coupling between the bright and dark subspace.

3.2.2 Decoherence and Master-Equation

The natural choice for such a coupling is to introduce an appropriate noise term. Henceforth, we assume uncorrelated noise, defined via the relation $\langle \Delta_i(t)\Delta_j(t')\rangle = \Gamma\delta(t-t')$. This allows for a convenient description in terms of a quantum-optical master-equation, as is for instance described in ref. [67]. There are several ways available to design noise that couples the bright and dark subspace. Here we concentrate on fluctuations of the detuning $\Delta(t)$, giving rise to a dephasing of the W-state according to $U|W\rangle = \sum_i e^{-i\Delta_i t}|i\rangle$; Then the Hamiltonian coupling the system to the bath reduces to

$$H_{\text{coupling}} = \sum_i |i\rangle\langle i|\Delta_i(t). \tag{3.3}$$

For a composite system like an artificial atom, we further need to distinguish between homogeneous and inhomogeneous dephasing: For homogeneous dephasing, every constituent of the system experiences the same fluctuation at any given time t, so that $\Delta_i(t) = \Delta(t)$. It follows that there is no particle-dependence in the Hamiltonian coupling the system to the bath, which in turn becomes proportional to the projector onto the W-state,

$$H_{\mathrm{hom}} = \Delta(t)|W\rangle\langle W|. \tag{3.4}$$

Consequently, the bright and dark subspaces stay invariant due to the vanishing commutator between the coherent Hamiltonian and the bath-coupling. This may also be seen in the resulting master-equation

$$\partial_t \rho = -\frac{i}{\hbar}\left[H_{\mathrm{coh}}, \rho\right] + \frac{\Gamma}{2}\left(c_W \rho c_W^\dagger - \frac{1}{2}c_W^\dagger c_W \rho - \frac{1}{2}\rho c_W^\dagger c_W\right), \tag{3.5}$$

where the jump-operator takes the form $c_W = |W\rangle\langle W|$ and projects onto the W-state. In contrast, inhomogeneous dephasing yields an individual energy shift $\Delta_i(t)$ for every atom in the ensemble. More specifically, the jump-operator $c_i = |i\rangle\langle i|$ yields the relation $c_i|W\rangle \notin \mathcal{B}$, and induces transitions between the bright and dark subspace. A straightforward calculation then yields the master-equation for inhomogeneous dephasing,

$$\partial_t \rho = -\frac{i}{\hbar}\left[H_{\mathrm{coh}}, \rho\right] + \frac{\Gamma}{2}\sum_i \left(c_i \rho c_i^\dagger - \frac{1}{2}c_i^\dagger c_i \rho - \frac{1}{2}\rho c_i^\dagger c_i\right), \tag{3.6}$$

which no longer allows for a description in the bright subspace alone.

3.2.3 Symmetries of the Master-Equation

The above master-equation (3.6) for an N-atom ensemble consists of $(N{+}1)^2$ first-order differential equations describing the time-evolution of the individual density-matrix components. Despite breaking the bright subspace invariance, those equations are still highly symmetrical due to the statistical nature of the fluctuations $\Delta_i(t)$. Indeed, the equations for two different atoms i and j are still interchangeable from a mathematical point of view. This allows for a reduction of the $(N{+}1)^2$ differential equations to merely two, and is most conveniently done by projecting eq. (3.6) onto the ground and W-state,

$$\langle G|\dot{\rho}|G\rangle = -i\Omega_N\left(\langle W|\rho|G\rangle - \langle G|\rho|W\rangle\right), \tag{3.7}$$

$$\langle W|\dot{\rho}|G\rangle = -i\Omega_N\left(\langle G|\rho|G\rangle - \langle W|\rho|W\rangle\right) - \frac{\Gamma}{2}\langle W|\rho|G\rangle, \tag{3.8}$$

$$\langle W|\dot{\rho}|W\rangle = -i\Omega_N\left(\langle G|\rho|W\rangle - \langle W|\rho|G\rangle\right) - \Gamma\left(\langle W|\rho|W\rangle + \frac{\langle G|\rho|G\rangle - 1}{N}\right). \tag{3.9}$$

Eq. (3.9) and the time derivative of eq. (3.7) may be expressed in terms of the expectation values $G = \langle G|\rho|G\rangle$ and $W = \langle W|\rho|W\rangle$ alone, and lead us to the reduced set of equations

$$\begin{aligned}\ddot{G} &= -2\Omega_N^2 G + 2\Omega_N^2 W - \frac{\Gamma}{2}\dot{G},\\ \dot{W} + \dot{G} &= -\Gamma\left(W + \frac{G-1}{N}\right).\end{aligned} \tag{3.10}$$

The transition from first- to second-order differential equation requires an additional initial condition for the time derivative of the ground-state probability $\dot{G}$. Although this seems to defy the deterministic time-evolution of the density-matrix, the initial condition is already covered by eq. (3.8), and reduces to $\dot{G}(t=0) = 0$ in the case of an uncorrelated artificial atom in the ground-state. The probability to absorb a photon is then proportional to the probability $E = 1 - G$ to find an excitation in the system. Expressed in terms of E the reduced master-equation (3.10) takes its final form

$$\begin{aligned}\ddot{E} &= -2\Omega_N^2(E-1) - 2\Omega_N^2 W - \frac{\Gamma}{2}\dot{E},\\ \dot{W} - \dot{E} &= -\Gamma\left(W - \frac{E}{N}\right).\end{aligned} \tag{3.11}$$

Before we continue with the numerical solution of the above equation, it is instructive to consider some analytic limits. First, for a single atom the master-equation (3.11) reduces to

$$\begin{aligned}\ddot{E} &= -2\Omega^2(E-1) - 2\Omega^2 W - \frac{\Gamma}{2}\dot{E},\\ \dot{W} - \dot{E} &= -\Gamma\left(W - E\right).\end{aligned} \tag{3.12}$$

Since $W = E$ for $N = 1$, the second equation is trivially fulfilled, and the system dynamics is governed by the first equation,

$$\ddot{E} = -4\Omega^2 E + 2\Omega^2 - \frac{\Gamma}{2}\dot{E}, \tag{3.13}$$

which is formally equivalent to a damped harmonic oscillator under the constant *force* $2\Omega^2$. The excitation probability corresponds to a displacement of the oscillator, whereas the Rabi-frequency is the spring constant. As one might expect from this analogy, the equilibrium solution indeed is $E = G = 1/2$.

In the steady-state with vanishing time-derivatives, the master-equation (3.11) takes the form of an algebraic equation,

$$\begin{aligned} 0 &= -2\Omega_N^2(E-1) - 2\Omega_N^2 W, \\ 0 &= -\Gamma\left(W - \frac{E}{N}\right). \end{aligned} \tag{3.14}$$

Via a straightforward calculation we find the steady-state solutions $E = NW = N/(N+1)$. The probability E for the system to carry an excitation approaches unity in the limit of a large number of atoms $N \gg 1$ inside the blockade-volume, and, in that sense, beats the rule that population inversion cannot be achieved in a two-state system. Since this is equivalent to the probability to absorb a photon, such a system behaves like a perfect absorber. Yet, the exact number of atoms $N \gg 1$ is not important, and only renormalizes the absorption timescale via the collective Rabi-frequency $\Omega_N = \sqrt{N}\Omega$.

An intuitive picture of the population inversion can be drawn via Fermi's golden rule: First, we assume that the transition from ground-state to collective W-state occurs at a rate $k_{G\to W}$, which is equal to the reverse process $k_{G\to W} = k_{W\to G}$. Likewise, the dephasing Γ induces transition-rates between $k_{W\to D_i}$ and $k_{D_j\to D_i}$ all the excited states, that is the W-state and all the dark states. The actual population-transfer per time-step is given by the rate times population in the respective state. In equilibrium, all rates cancel each other, and we find an equal population $G = W = E/N = 1/(N+1)$ in all states.

3.2.4 Numerical Solution of the Master-Equation

The full eqs. (3.11) can be solved numerically within a Runge-Kutta routine, with results shown in Fig. 3.4. As one might expect from the dynamics of a *super-atom* without dephasing (see appendix 6.A.4), the characteristic timescale of the oscillations is governed by the collective Rabi-frequency Ω_N. On the other hand, the probability E for the system to be in the excited state grows with a characteristic rate Γ_{eff}. For small dephasing-rates $\Gamma \ll \Omega_N$, E exhibits damped oscillations. Conversely, in the limit of large dephasing $\Gamma \gg \Omega_N$, the system enters an over-damped regime and is in close analogy to the behavior of a damped harmonic oscillator. Although the dephasing-rate Γ governs the timescale on which the system enters its steady-state, the collective Rabi-frequency sets a lower boundary for this to happen: Since the dephasing only accounts for a transfer of population from the

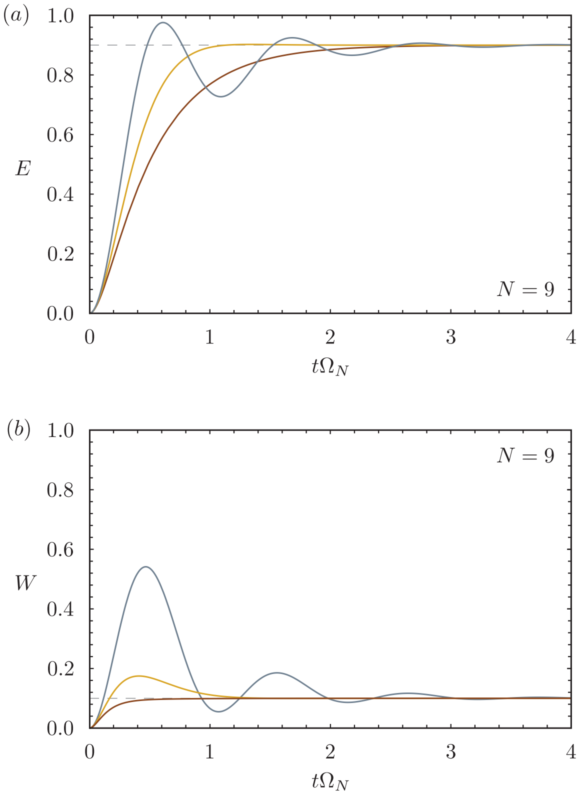

Figure 3.4: Numerical time-evolution of the master-equation (3.11) for the experimental relevant case of $E(0) = \dot{E}(0) = W(0) = 0$. (a) The probability E for the atomic system to be in the excited state saturates exponentially up to the final value $E(t \to \infty) = N/(N{+}1)$ with a characteristic rate Γ_{eff}. The plot shows the numerical integration for $N = 9$ atoms in the overdamped regime for $\Gamma = 7\Omega_N$ (red line), as well as in the underdamped regime with $\Gamma = \Omega_N$ (green line), and in the crossover regime $\Omega_N = 3\Gamma$ (blue line). (b) In comparison, the bright W-state shows the same initial time-evolution. Yet, the dephasing Γ accounts for a probability transfer to the dark states, and leads to a damping of W to the steady-state value $E(t \to \infty) = 1/(N{+}1)$. The color-code matches the one in (a).

W-state into the dark subspace, the ground-state is unaffected. Yet, population transfer from ground to W-state is governed by the collective Rabi-frequency, which thus acts as a bottleneck for the system dynamics. A more in-depth discussion of the effective saturation-rate will follow in the next subsection.

In the scaling-limit $t\Omega_N \to \infty$, the probability to be in the excited state E saturates at $N/(N+1)$, independently of both the dephasing-rate and the collective Rabi-frequency. Again, this is in perfect agreement with the previous analytic results.

3.2.5 Approximate Analytical Solution of the Master-Equation

A major drawback of the equations (3.11) is that they do not allow for a closed-form analytic solution. However, we can make an intuitive approximation by

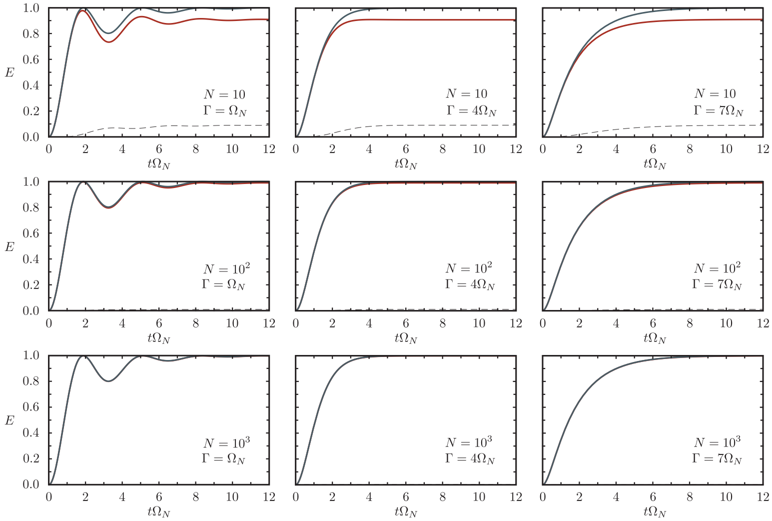

Figure 3.5: Comparison between the numerical solution of the exact equations for the probability E (3.11) (solid red lines) and the analytical solution of the approximate equations (3.15) (solid blue lines) and their respective difference (black dashed lines) for different system sizes N and dephasing-rates Γ.

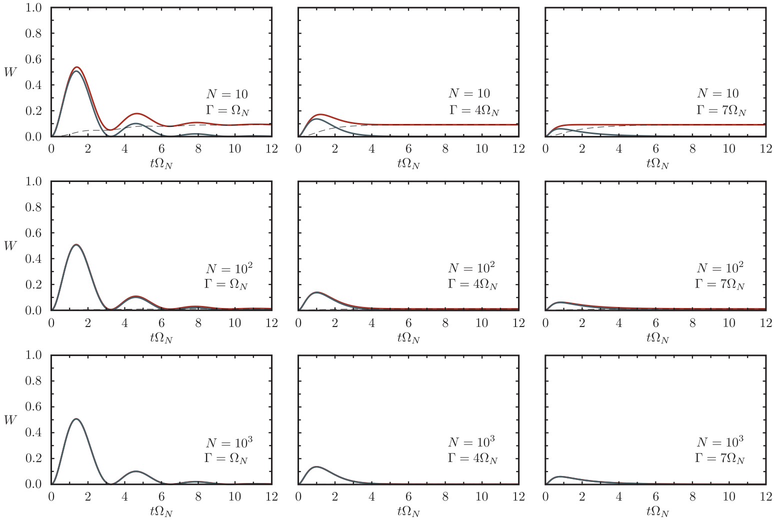

Figure 3.6: Comparison between the numerical solution of the exact equations for the probability W (3.11) (solid red lines) and the analytical solution of the approximate equations (3.15) (solid blue lines) and their respective difference (black dashed lines) for different system sizes N and dephasing-rates Γ.

neglecting the factor $E/N < 1/N$ in the large-N limit, which simplifies the master-equation (3.11) to

$$\begin{aligned} \ddot{E} &= -2\Omega_N^2(E-1) - 2\Omega_N^2 W - \frac{\Gamma}{2}\dot{E}, \\ \dot{W} - \dot{E} &= -\Gamma W. \end{aligned} \tag{3.15}$$

These equations can then be solved by an exponential ansatz. For the experimental relevant initial conditions $E(0) = \dot{E}(0) = W(0) = 0$ describing an uncorrelated gas in the electronic ground-state the solution to the approximate equations read

$$\begin{aligned} E(t) &= 1 - e^{-\frac{\Gamma}{2}t}\left[\cosh\gamma t + \frac{\Gamma}{4\gamma}\sinh\gamma t\right]^2, \\ W(t) &= \frac{\Omega_N^2}{\gamma^2} e^{-\frac{\Gamma}{2}t}\sinh^2\gamma t, \end{aligned} \tag{3.16}$$

with $\gamma = \sqrt{(\Gamma/4)^2 - \Omega_N^2} \in \mathbb{C}$. A comparison between the analytic solution of the approximate equations and numerical solution of the exact equations is shown in Fig. 3.2.5 and 3.2.5 for E and W, respectively. As one might expect from the approximation scheme we find deviations to be on the order of $1/N$. With the number of atoms inside a blockade-radius easily exceeding 10^2 even in a hot gas Rydberg experiment [68], such an approximation is well justified. We can therefore use the solution (3.16) in order to derive the effective saturation-rate Γ_{eff} via a leading order expansion of the exponent, namely $2\cosh t \approx -2\sinh t \approx e^{-\Re t}$. The resulting saturation-rate takes the form

$$\tilde{\Gamma}_{\text{eff}} = \Gamma/2 - 2\Re\gamma. \tag{3.17}$$

For small dephasing-rates $\Gamma \ll \Omega_N$ the square root is purely imaginary, and the effective saturation-rate is given by $\tilde{\Gamma}_{\text{eff}} = \Gamma/2$. Increasing the dephasing-rate Γ, the aforementioned formula predicts a transition to the over-damped regime at a critical dephasing-rate $\tilde{\Gamma}_c = 4\Omega_N$. However, this naive derivation does not yield the correct effective saturation-rate in the transition region: According to eq. (3.17), the system exhibits an effective saturation-rate $\tilde{\Gamma}_{\text{eff}} > \Omega_N$. As mentioned before, the characteristic timescale of the system excitation is governed by the collective Rabi-frequency Ω_N, not the dephasing-rate Γ. Therefore, an effective saturation rate larger than the collective Rabi-frequency is just not possible. This intuitive behavior is also confirmed by a numeric evaluation of the system dynamics via

$$1/\Gamma_{\text{eff}} = G^{-1}(1/e), \tag{3.18}$$

and shows a transition into the over-damped regime already at $\Gamma_c \approx 2\Omega_N$ (see Fig. 3.7). The disparity between the naive analytic calculation and the numeric evaluation is due to the neglected interference effects between the cosh- and sinh-terms in eq. (3.16). These lead to a slower saturation, with an effective saturation-rate that is always smaller than the collective Rabi-frequency. On the other hand, we find that the saturation-rate follows $\Gamma_{\text{eff}} \approx 4\Omega_N^2/\Gamma$ for strong damping $\Gamma \gg \Omega_N$, predicted by both eq. (3.17) and (3.18), although from opposing limits. Note that this slow-down of the system dynamics is in analogy to the quantum Zeno effect [69], where a constant measurement effectively freezes the system.

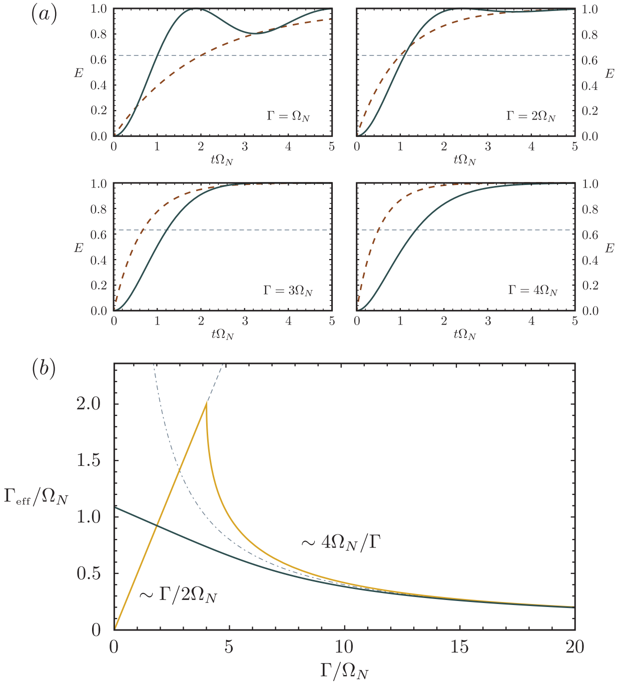

Figure 3.7: (a) Numerical time-evolution of the approximate master-equation (3.15) for different dephasing-rates Γ in the cross-over regime $\Gamma \approx \Omega_N$ (solid blue lines). The system shows a faster transition into the over-damped regime as compared to the naive saturation-rate $\tilde{\Gamma}_{\text{eff}}$ defined in eq. (3.17) (dashed brown line). The dashed blue line is a guide to the eye and indicates $1 - 1/e$. (b) Plot of the effective saturation rate eq. (3.17) (solid yellow line) and the $1/E$ definition from eq. (3.18) (solid green line). The plot clearly shows that eq. (3.17) overestimates the saturation-rate, and suggests dynamics faster than the collective Rabi-frequency Ω_N. The dashed and dash-dotted black lines are the scaling-limits for $\Gamma \ll \Omega_N$ and $\Gamma \gg \Omega_N$, respectively, and agree well with the numerical results.

3.3 Absorption Properties of the Artificial Atom

3.3.1 Optical Density

For the setup to work, we need to ensure that the time it takes a photon to pass through the system is large as compared to the time it takes to absorb it. The first timescale may be captured by the coherence-time of a photon τ, while the second one is given by the effective saturation-rate $1/\Gamma_{\text{eff}}$. In turn, the above condition reduces to $\Gamma_{\text{eff}}\tau > 1$. The coherence-time τ of a single photon with frequency ω_p and transverse model volume A can be expressed in terms of the single-photon Rabi-frequency [62]

$$\Omega_p = \sqrt{\frac{2\pi\omega_p d_p^2}{\varepsilon_0 c\tau A}}, \tag{3.19}$$

where d_p is the dipole matrix-element for the transition $|g\rangle \to |p\rangle$, ε_0 the vacuum permeattivity and c the speed of light. By use of the two-photon Rabi-frequency $\Omega = \Omega_p\Omega_c/4\Delta_c$ and the effective saturation-rate in the over-damped regime $\Gamma_{\text{eff}} = 4\Omega_N^2/\Gamma$, we find

$$\Gamma_{\text{eff}}\tau = \kappa = 2\pi N \frac{d^2}{\hbar\varepsilon_0 cA}\frac{\omega_p}{2\Gamma}\frac{\Omega_c^2}{4\Delta_c^2} = \frac{\Omega_c^2}{8\Delta_c^2}\frac{\gamma_p}{\Gamma}\,\kappa_p, \tag{3.20}$$

where κ is the total optical density and $\kappa_p = 6\pi\lambda^2 N/A$ is the resonant optical thickness for the transition $|g\rangle \to |p\rangle$. Here it is important to note that for the setup to work, the spontaneous emission $\Omega_c^2\gamma_p/8\Delta_c^2$ from the intermediate p-state needs to be smaller than the dephasing Γ of the W-state, which results in the condition $\Omega_c^2\gamma_p/8\Delta_c^2\Gamma \ll 1$. Hence, the full absorption has to take place on a timescale shorter than the spontaneous emission from the Rydberg-state.

The above conditions can easily be satisfied within a cold Rydberg setup: A ^{87}Rb Bose-Einstein condensate with $N = 10^3$ atoms in a small trap with trapping-frequency 1 kHz has a Thomas-Fermi radius of $r_{\text{TF}} \approx 1\ \mu$m. The resonant optical thickness thus reduces to $\kappa_p \approx 350$. In consequence, this provides a wide range to adjust the spontaneous emission from the p-state via the detuning Δ_c and control Rabi-frequency Ω_c. Indeed, assuming $\Omega_c^2\gamma_p/8\Delta_c^2\Gamma \approx 0.1$ yields an optical thickness $\kappa \gtrsim 10$.

3.3.2 Dynamics of a Saturating Absorber

Under the assumption that the saturation-rate Γ_{eff} is the dominating energy-scale of the system we can neglect any photon re-emission and coherent dynamics, and are left with the effective master-equation

$$\partial_t \rho = \Gamma_{\text{eff}} \left[c\rho c^\dagger - \frac{1}{2} \left(c^\dagger c \rho + \rho c^\dagger c \right) \right], \tag{3.21}$$

describing the time-evolution of a composite system of absorber and light-field with density-matrix ρ. Here, the jump-operator $c = a|E\rangle\langle G|$ accounts for the transition from an excitation in the light-field to one in the two-state system, with a the photon annihilation-operator defined via $a|n\rangle = \sqrt{n}|n-1\rangle$.

There are two important points to make about eq. (3.21): First, the jump-operator satisfies $c^2 = 0$ due to the factor $|E\rangle\langle G|$ and accounts for the fact that a single photon saturates the absorber. Without this condition eq. (3.21) would lead to an exponential decay of the light-field intensity as, for instance, is observed in glass. Second, the description within this master-equation differs from a simple application of the photon annihilation-operator onto a state of light: The latter describes an instantaneous process like the reflection of a photon on a beamsplitter [70], whereas the former describes absorption over a time large compared to the coherence-time of a single photon [71].

Here we concentrate on the experimental relevant case in which the absorber is in the ground-state $|G\rangle$. Thus the initial density-matrix reduces to $\rho_0 = |G\rangle\langle G| \otimes \chi$, where χ describes an arbitrary light-field. It turns out that the time-evolution super-operator $U(t)$ for the density-matrix ρ of the composite system can be calculated analytically (see appendix 3.B) and the application of $U(t)$ onto the initial density-matrix yields

$$\begin{aligned} U(t)|G\rangle\langle G| \otimes \chi = {} & |E\rangle\langle E| \otimes \sum_{n,n'} \chi_{n,n'} \frac{2\sqrt{nn'}}{n+n'} \left(1 - e^{-\frac{\Gamma_{\text{eff}} t}{2}(n+n')}\right) |n-1\rangle\langle n'-1| \\ & + |G\rangle\langle G| \otimes \sum_{n,n'} \chi_{n,n'} e^{-\frac{\Gamma_{\text{eff}} t}{2}(n+n')} |n\rangle\langle n'|. \end{aligned} \tag{3.22}$$

The first term is proportional to the excited state $|E\rangle\langle E|$, and grows exponentially on a timescale given by the effective saturation–rate times the number of photons in the respective light-state. The difference to the simple application of a photon annihilation-operator is the factor of $1/(n+n')$. Even so, in the short time limit with $e^{-\frac{\Gamma_{\text{eff}} t}{2}(n+n')} \approx 1 - \frac{\Gamma_{\text{eff}} t}{2}(n+n')$ we recover the same expression a simple application of a would yield. On the other hand, the second term proportional to the ground-state $|G\rangle\langle G|$ shows an exponential decay on a corresponding timescale. In the scaling-limit $\Gamma_{\text{eff}} t \gg 1$, the resulting state takes the form

$$U(t \to \infty)|G\rangle\langle G| \otimes \chi = |E\rangle\langle E| \otimes \sum_{n,n'} \chi_{n,n'} \frac{2\sqrt{nn'}}{n+n'} |n-1\rangle\langle n'-1| + |G\rangle\langle G| \otimes \chi_{0,0} |0\rangle\langle 0|, \tag{3.23}$$

where the probability for the two-state system to be in the excited state is thus given by $1 - \chi_{0,0}$. Note that this is the fundamental quantum limit for any photon absorption: Without any photon present, none may be absorbed.

3.4 Experimental Implementation of Noise

There are several microscopic mechanisms that can lead to decoherence and dephasing in a *super-atom*. While fluctuations in phase and intensity of the driving lasers are definitely one of the major sources of decoherence, those are generally on a length-scale much larger than the inter-atom separation. Yet, for our purpose it is paramount that spatial correlations are on the order of the inter particle distance, so every atom experiences its individual noise.

3.4.1 Speckle Pattern of Light

To create such a strong and controlled inhomogeneous decoherence, the method of choice would be to induce an ac-Stark shift on the Rydberg-state. This may be achieved by a speckle-pattern of light, in close analogy to experiments done in the context of Anderson-localization [22]. In contrast to the aforementioned experiment, where a random but static potential was created, we envisage the use of white light to remove temporal correlations. The combination of strong-field white light pulses and a diffusive plate that accounts for the speckle-pattern via diffraction creates the required decoherence. Then, the detuning for each atom fulfills $\langle \Delta_i(t) \Delta_j)(t') \rangle = \Gamma \delta_{ij} \delta(t - t')$, and allows for the derivation of the master-equation (3.6) by standard methods [67].

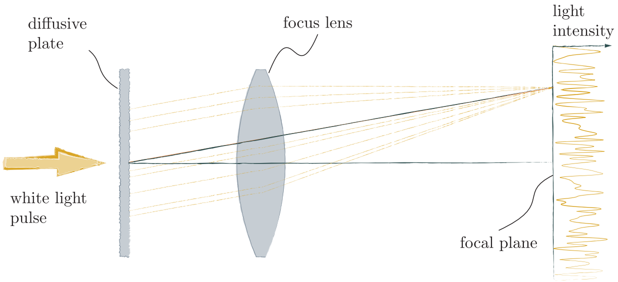

Figure 3.8: A white light pulse shines on a diffusive plate, which induces a spatially random phase shift. As a result, interference between the light creates a random potential landscape on the focal plane.

3.4.2 Pulsed Dephasing

Another way to create dephasing of the W-state is to employ a random but static detuning Δ_i for each of the excited states $|i\rangle$. The time-evolution for the i-th excited state takes the form $U_\Delta(t)|i\rangle = e^{-i\Delta_i t}|i\rangle$, leading to a decrease of the overlap between the initial W-state and its time-evolved counterpart $U_\Delta(t)|W\rangle$, like

$$|\langle W|U(t)|W\rangle|^2 = \frac{1}{N} + \frac{1}{N^2}\sum_{i\neq j} e^{i(\Delta_i - \Delta_j)t}. \tag{3.24}$$

In consequence, such a time-evolution coherently drives the system into the subspace of the dark states. In the limit of a large number of atoms N we can replace the summation over random detunings by an integral over their probability distribution. It follows that the dephasing-rate is determined by the characteristic properties of the probability-distribution. For instance, a gaussian distribution of width $\bar{\Delta}$ yields a decay of the W-state like $|\langle W|U(t)|W\rangle|^2 = |e^{-\bar{\Delta}t}|^2$, and consequently $E = 1 - |e^{-\bar{\Delta}t}|^2$. However, this scheme will not work for a coherent coupling of the W-state to the collective ground-state $|G\rangle$: If the Rabi-frequency is large compared to the characteristic detuning, the coherent time-evolution will de-excite the system before any relevant dephasing can occur. Conversely, if the characteristic detuning is large compared to the Rabi-frequency, the coupling to some of the excited states $|i\rangle$ is far off-resonant, and strongly suppresses their population. A way out is to use a pulsed Rabi-frequency to effectively decouple the timescales of dephasing $1/\bar{\Delta}$ and coherent pumping $1/\Omega$. A detailed analysis of this scheme is described in the appendix 3.C.

3.5 Applications

3.5.1 Photon Counter

The combination of several absorbers into a chain of individually addressable cells opens the way for high fidelity n-photon detection. With every cell absorbing only a single photon, a n-photon light state passes through the chain up to the n-th cell where the last photon is absorbed. Probing for a Rydberg-excitation in each cell then provides a deterministic photon-number detection of the absorbed state. By use of a robust detection-scheme for the Rydberg-excitation, the setup allows for single-photon detection with near unit fidelity. In analogy to the many-body Rydberg-gate [72,73], we can use electromagnetic induced transparency (EIT) [50] in order to detect a Rydberg-excitation: With no Rydberg-excitation present, a detection beam just passes through the system. Conversely, as soon as an atom is excited into the Rydberg-state, the EIT condition is violated and the detection beam acquires a phase-shift $\phi = \Omega_c^2/4\Delta_c$ due to the real part in the dielectric response function [50]. This phase shift can then be detected by a subsequent homodyne measurement, thus creating a near perfect single-photon detector. In addition, this setup also allows for the realization of a classical single photon transistor: A single

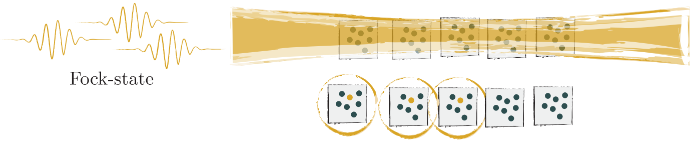

Figure 3.9: Setup for a high fidelity k-photon detector: Illustration of the incoming probe-field with three photons on a chain of several cells, each with a deterministic single photon absorber. Each cell absorbs exactly one photon, while the remaining beam propagates to the next cell. In the first three cells exactly one photon is absorbed and an atom is excited to the Rydberg-state, which in turn is subsequently detected: The position of the last Rydberg-excitation provides the number of photons within the beam.

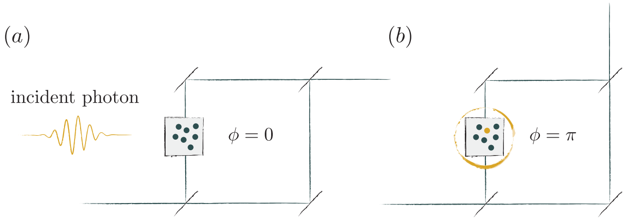

Figure 3.10: In gate operation language, the absorber can act as a single photon transistor: The induced phase shift of $\phi = \Omega_c^2/4\Delta_c$ can trigger a macroscopic light beam via a Mach-Zender interferometer.

photon in the probe-beam can switch several photons in the homodyne detector (see Fig. 3.10).

3.5.2 Creation of Non-Classical States of Light

Subtracting a single photon from a squeezed-vacuum state allows for the creation of non-classical states of light [70]. This idea has previously been explored both theoretically and experimentally in the context of creating photonic cat-states from a squeezed vacuum [74–77]. However, the means applied to absorb single photons in these experiments were highly probabilistic, resulting in a low efficiency of the setup. Here, our scheme provides a major advantage, as it allows for the subtraction of photons with near unit probability. As shown in section 3.3.2, the density-matrix for a photon-subtracted state of light can be calculated analytically. Starting from an initial squeezed-vacuum state [78] with density matrix

$$\chi_{\text{sv}} = \sum_{n,n'=0} C_r^*(n)|n\rangle\langle n'|C_r(n'), \tag{3.25}$$

$$C_r(n) = \frac{1}{\sqrt{\cosh r}}\,\frac{\sqrt{m!}\cos\frac{\pi}{2}m}{2^{-m/2}\left(\frac{m}{2}\right)!}\tanh^{m/2} r, \tag{3.26}$$

and squeezing factor r, the absorption of a single photon yields for $\Gamma_{\text{eff}}t \gg 1$ the non-classical state

$$\chi_{\text{falsecat}} = \sum_{n,n'=1} C_r^*(n)|n-1\rangle\frac{2\sqrt{nn'}}{n+n'}\langle n'-1|C_r(n'). \tag{3.27}$$

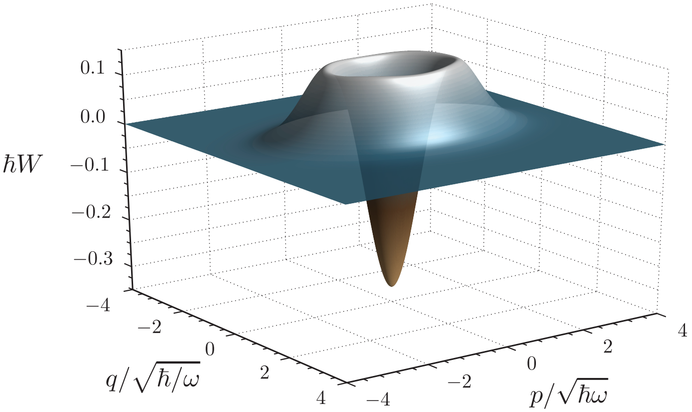

Figure 3.11: Non-classical states of light: Wigner-function of the outcoming photon state after the deterministic absorption of a photon within the cell. The incoming state is characterized by a coherent state ($\alpha = 0$) with subsequent amplitude squeezing ($w = -0.3$).

The negative values of the resulting Wigner-function are a clear sign of the non-classical nature of this particular state of light. It is important to mention that the creation of cat-states in ref. [79] is based on reflection of photons, and only takes the short time limit of the time-evolution U into account. Indeed, the time-evolution operator takes the approximate form

$$U = e^{\Gamma_{\text{eff}}(\hat{J}+\hat{L})t} \approx 1 + \Gamma_{\text{eff}}(\hat{J}+\hat{L})t + \mathcal{O}\left((\Gamma_{\text{eff}}t)^2\right). \tag{3.28}$$

In contrast to eq. 3.27 the resulting light state reads $a\chi_{\text{sv}}a^\dagger$. The difference is the factor of $2/(n+n')$, and stems from higher orders of $\Gamma_{\text{eff}}t$ in the time-evolution operator. Even so, for small cats $\alpha \ll 1$, large photon-numbers play a minor role, and the overlap between the cat-state in both methods of creation is close to unity (see Fig. 3.13).

3.6 Conclusion

We have shown in chapter 3 that the absorption properties of an artificial atom can be strongly enhanced by inducing a controlled dephasing for the excited states. Such an additional coupling lead to an induced coupling between the previously

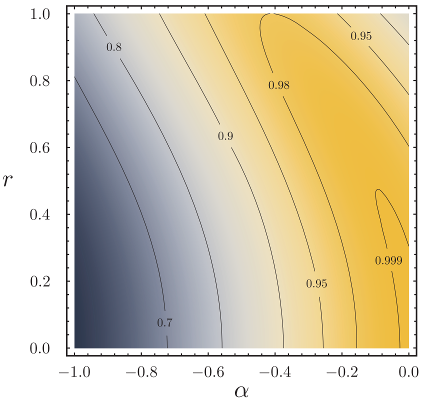

Figure 3.12: Density plot showing the overlap between a photon-subtracted state (3.27) created from an initial squeezed-vacuum with squeezing factor r and an odd cat $|\text{odd cat}\rangle = |\alpha\rangle - |-\alpha\rangle$.

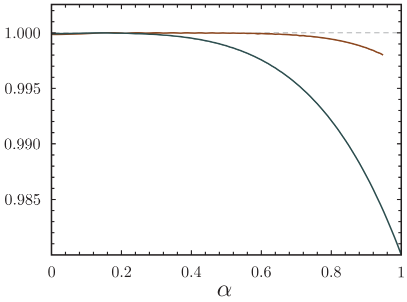

Figure 3.13: Optimal overlap between a photon subtracted state (3.27) created from an initial squeezed-vacuum with squeezing factor r and an odd cat $|\text{odd cat}\rangle = |\alpha\rangle - |-\alpha\rangle$ (orange line). In comparison we plotted the optimal overlap between the non-classical state created via photon reflection ($a\chi_{\text{sv}}a^\dagger$) and an odd cat $|\text{odd cat}\rangle = |\alpha\rangle - |-\alpha\rangle$ (blue line), as was demonstrated in ref. [70].

dark states and the bright states, and therefore strongly increased the density of states for the excited level. The resulting asymmetry between ground- and excited states then accounted for the enhanced absorptive properties of the artificial atom, while the strong interaction between the excitations prevented the system to carry more than a single excitation simultaneously, and rendered the system invisible after the first photon had been absorbed.

We have derived a theoretical description of this single-photon absorber in terms of a quantum-optical master-equation and have shown that the symmetry of the artificial atom allowed for a reduction of these $(N+1)^2$ differential equations to just two. Moreover, we have provided both a full numerical solution as well as an approximate analytical solution for the density-matrix time-evolution in the limit of large atom numbers. This allowed us to thoroughly analyze the absorptive properties of such a medium, and identify a regime where deterministic single-photon absorption can be achieved within an ensemble of cold atoms coherently coupled to a Rydberg-state. In addition, we discussed possible implementation schemes for the controlled dephasing. By neglecting the coherent dynamics of the system in the limit of strong dephasing $\Gamma \gg \Omega_N$, we were able to derive the effect of single-photon absorption on arbitrary states of light, and calculated an analytic expression for the density-matrix of a photon-subtracted state. Moreover, we explored possible applications of our design as a n-photon detector, a single-photon phase gate and a device capable to deterministically create non-classical states of light. Further work needs to be, and actually, is done in the context of pulse propagation through the sample, an issue we generously neglected in the current work. This, of course, is related to the question whether such a medium reflects an incoming probe beam, and hence would nullify our efforts in fabricating a deterministic single-photon absorber. However, preliminary studies indicate that reflection can be strongly suppressed by using an appropriate density profile for the absorbing ensemble.

3.A Effective Master-Equation in the Overdamped Regime

The master-equation for inhomogeneous dephasing reads

$$\partial_t \rho = -\frac{i}{\hbar}[H_{\mathrm{coh}}, \rho] + \Gamma \mathcal{L}(\rho), \tag{3.29}$$

where $\mathcal{L}(\rho)$ and H_{coh} describe the inhomogeneous dephasing and the coherent time-evolution driven by the laser coupling, respectively,

$$\mathcal{L}(\rho) = \sum c_i \rho c_i^\dagger - \frac{1}{2}\left\{c_i^\dagger c_i, \rho\right\}, \quad H_{\text{coh}} = \Omega \sum_i \left[|i\rangle\langle G| a_i + |G\rangle\langle i| a_i^\dagger\right]. \tag{3.30}$$

It is convenient to go to the Laplace-space, in which this equation takes the form

$$sR(s) - R(0) = -\frac{i}{\hbar}[H_{\text{coh}}, R(s)] + \Gamma\mathcal{L}(R(s)), \tag{3.31}$$

with $R(s)$ the Laplace-transform of the density-matrix ρ. Henceforth, we assume that (i) the number of atoms N is large and (ii) the dephasing-rate Γ is the dominating energy scale. In particular, the coherent time-evolution of the density-matrix is much slower than the incoherent dephasing, so that $\Omega \ll \Gamma$. Additionally, we restrict our discussion to the case in which the atomic ensemble is in the collective ground state $|G\rangle$ and thus $R(0) = |G\rangle\langle G|$. For the following analysis it is convenient to define the projection operators P_D, $P_{\bar{W}}$, and P_C that project the density-matrix onto its diagonal D, the coherences between the excited states $\bar{W}$ and the coherences between the excited and the ground state C, respectively, as well as the projection P_Q via $P_Q = \text{id} - P_C$. By applying the projection operator P_C on the master-equation (3.31), we obtain

$$P_C sR(s) = -\frac{i}{\hbar} P_C[H_{\text{coh}}, P_Q R(s)] - \frac{\Gamma}{2} P_C R(s), \tag{3.32}$$

where we have used $P_C R(0) = 0$. Under the assumption that $\Gamma/2 + s \approx \Gamma/2$ we may solve this equation with respect to $P_C R(s)$, and find

$$P_C R(s) \approx -\frac{i}{\hbar}\frac{2}{\Gamma} P_C[H_{\text{coh}}, P_Q R(s)]. \tag{3.33}$$

Likewise, the master-equation projected onto the subspace Q takes the form

$$P_Q(sR(s) - R(0)) = -\frac{1}{\hbar^2}\frac{2}{\Gamma} P_Q[H_{\text{coh}}, P_C[H_{\text{coh}}, P_Q R(s)]] - \Gamma P_{\bar{W}} R(s). \tag{3.34}$$

To further reduce this equation we use $P_Q = P_D + P_{\bar{W}}$ in order to split the double-commutator into its diagonal part D and the coherences between excited states $\bar{W}$.

The projection onto the latter then reads

$$\begin{aligned}&[H_{\text{coh}}, [H_{\text{coh}}, R_Q]_C]_{\bar{W}} \\ &\quad= \left[2\sum_{i,j} |i\rangle a_i \langle G|R_Q|G\rangle a_j^\dagger \langle j| - \sum_{i,l} \left\{ |i\rangle a_i a_l^\dagger \langle l|, R_Q \right\} \right]_{\bar{W}}, \end{aligned} \tag{3.35}$$

where latin indices run over all excited states and, again, $s + \Gamma \approx \Gamma$ applies. Additionally we have used the short-hand notation $R_Q = P_Q R$. The first term on the right-hand side of eq. (3.35) describes transitions from the ground state to the coherences between the excited states, whereas the second is due to transition in between the latter. The first term is clearly dominating since initially $\langle i|R|j\rangle = 0$, and any change is suppressed by a factor Ω^2/Γ^2. (Note that neglecting s does, in fact, spoil the relation $\langle i|R|j\rangle = 0$ in eq. (3.35).) Indeed, a simple model that assumes all coherences to be of the same value proofs this assumption to be correct. Thus, the coherences between the excited states do follow the ground-state occupation,

$$P_{\bar{W}} R(s) = \frac{4\Omega^2}{\Gamma^2} \sum_{i \neq j} |i\rangle a_i \langle G|R_Q|G\rangle a_j^\dagger \langle j|, \tag{3.36}$$

as is the case for the coherences between the ground and the excited states (see eq. (3.33)). On the other hand, the time-evolution of the diagonal part of eq. (3.34) is solely governed by the double-commutator with characteristic time-scale Ω^2/Γ, as may be seen directly in the projection,

$$\begin{aligned}&[H_{\text{coh}}, [H_{\text{coh}}, R_Q]_C]_D \\ &\quad= \Bigg[2\sum_{i,j} |G\rangle a_i^\dagger \langle i|R_Q|j\rangle a_j \langle G| - \sum_{i} \left\{ |G\rangle a_i^\dagger a_i \langle G|, R_Q \right\} \\ &\qquad + 2\sum_{i} |i\rangle a_i \langle G|R_Q|G\rangle a_i^\dagger \langle i| - \sum_{i} \left\{ |i\rangle a_i a_i^\dagger \langle i|, R_Q \right\} \Bigg]_D . \end{aligned} \tag{3.37}$$

Following the argument above we may neglect any contributions due to off-diagonal elements by replacing the double sum in the first term with a simple one. To an accuracy of Ω^2/Γ^2 the master-equation in time-domain hence reduces to

$$\dot{\rho}_D = \frac{1}{\hbar^2}\frac{2\Omega^2}{\Gamma}\sum_i \left[2C_i^\dagger \rho_Q C_i - \left\{ C_i^\dagger C_i, \rho_Q \right\} + 2C_i \rho_Q C_i^\dagger - \left\{ C_i C_i^\dagger, \rho_Q \right\} \right]_D , \quad (3.38)$$

with the effective jump operator $C_i = a_i|i\rangle\langle G|$. The first and the last term in the square bracket induce transitions from the excited states back to the ground state. Their contribution is proportional to the probability to be in the excited state, which increases from zero to $1/(N+1)$. Conversely, the two middle terms are proportional to the ground state occupation number that decreases from its initial value of one to $1/(N+1)$. Hence, the former, back-action terms only become relevant close to the steady-state in which, by definition, no time-evolution occurs, and may thus be neglected. Such an approximation results in a slightly modified steady-state, meaning that the ground-state occupation number approaches zero as compared to $1/(N+1)$. We therefore find the approximate master-equation for the diagonal entries of the density matrix

$$P_D \dot{\rho} = \frac{4\Omega^2}{\Gamma} P_D \sum_i \left[C_i P_Q \rho C_i^\dagger - \frac{1}{2}\left\{ C_i^\dagger C_i, P_Q \rho \right\} \right]. \quad (3.39)$$

All off-diagonal elements can be expressed in terms of the diagonal elements by use of the eqs. (3.33) and (3.36), meaning that eq. (3.39) is sufficient to describe the system dynamics. For all intents and purposes the individual states $|i\rangle$ are equivalent except for their spatial position. The latter difference is however unimportant as long as all the atoms are situated within a blockade volume. We may hence introduce a dummy-sate $|E\rangle$ that describes any of the atoms to carry an excitation. With that the master-equation reduces to

$$P_D \dot{\rho} = \frac{4\Omega^2 N}{\Gamma} P_D \left[C P_Q \rho C^\dagger - \frac{1}{2}\left\{ C^\dagger C, P_Q \rho \right\} \right], \quad (3.40)$$

where $C = a|E\rangle\langle G|$ is the dummy jump-operator. Note that the characteristic time-scale is Ω_N^2/Γ, in agreement to the analysis presented in subsection 3.2.5. Moreover, it is important to stress that the dummy-state is, in fact, not a coherent superposition but an incoherent mixture due to the strong dephasing. Indeed, a coherent superposition would be a W-state, and to prevent it was the sole purpose of the deterministic single-photon absorber in the first place.

3.B Dynamics of a Saturating Absorber

In this section, we derive the influence of a single-photon absorber on a weak probe-field χ. The single-photon absorber is described by a two-state system with collective ground- and exited state denoted by $|G\rangle$ and $|E\rangle$, respectively. Under the assumption that the absorption-rate Γ_{eff} is the dominating energy-scale we can neglect any photon emission and coherent dynamics. Then the time-evolution for a density-matrix ρ describing the composite system of absorber and light-field takes the form

$$\partial_t \rho = \Gamma_{\text{eff}} \left[c\rho c^\dagger - \frac{1}{2} \left(c^\dagger c\rho + \rho c^\dagger c \right) \right]. \tag{3.41}$$

Here, the jump-operator $c = a|E\rangle\langle G|$ accounts for the transition from an excitation in the light-field to one in the two-state system, with the photon annihilation-operator denoted by a. An important aspect is that the jump-operator satisfies $c^2 = 0$, and corresponds to the fact that a single photon saturates the absorber. It is convenient for the following discussion to express the master-equation in the compact form

$$\partial_t \rho = \Gamma_{\text{eff}} (\hat{J} + \hat{L})\rho, \tag{3.42}$$

with the super-operators $\hat{J}$ and $\hat{L}$ are defined via

$$\hat{J}\rho = c\rho c^\dagger, \quad \hat{L}\rho = -\frac{1}{2} \left(c^\dagger c\rho + \rho c^\dagger c \right). \tag{3.43}$$

Then, a formal solution to the above master-equation takes the form of a time-evolution operator U, so that

$$\rho(t) = U\rho_0 = e^{\Gamma_{\text{eff}}(\hat{J}+\hat{L})t} \rho_0, \tag{3.44}$$

where ρ_0 is the initial state of the system at $t = 0$. The saturation-condition $c^2 = 0$ allows for a decomposition of the exponential in the time-evolution operator,

$$U = \hat{J} \sum_n \frac{\hat{L}^{n-1}}{n!} (\Gamma_{\text{eff}} t)^n + e^{\Gamma_{\text{eff}} \hat{L} t}. \tag{3.45}$$

First, note that for any light-field χ, the density-matrix $\rho = |E\rangle\langle E| \otimes \chi$ is an eigenstate of the time-evolution operator due to the relation $\hat{J}|E\rangle\langle E| = \hat{L}|E\rangle\langle E| = 0$.

To put it in a more physical context, the excited absorber no longer couples to the light-field, and is thus invisible. Consequently, we can reduce our discussion to the experimentally relevant initial states $\rho = |G\rangle\langle G| \otimes \chi$, where the two-state system is in the ground-state. Second, the summation in the time-evolution operator may be written in the more compact form

$$\sum_{n=1} \frac{\hat{L}^{n-1}}{n!}(\Gamma_{\text{eff}} t)^n = \frac{1}{\hat{L}}\left(e^{\Gamma_{\text{eff}}\hat{L}t} - 1\right) = \Gamma_{\text{eff}} \int_0^t dt\, e^{\Gamma_{\text{eff}}\hat{L}t}. \tag{3.46}$$

In consequence, the full time-evolution operator reads

$$U = \left(\hat{J}\left[\Gamma_{\text{eff}} \int_0^t dt\right] + 1\right) e^{\Gamma_{\text{eff}}\hat{L}t}. \tag{3.47}$$

Within a Fock-basis $\{|n\rangle\}$, the operator $e^{\Gamma_{\text{eff}}\hat{L}t}$ can be expressed as

$$\begin{aligned} e^{\Gamma\hat{L}t}\chi &= \sum_{n,n'} \chi_{n,n'} e^{\Gamma_{\text{eff}}\hat{L}t}|n\rangle\langle n'| = \sum_{n,n'} \chi_{n,n'} e^{-\Gamma_{\text{eff}}c^\dagger ct/2}|n\rangle\langle n'|e^{-\Gamma_{\text{eff}}c^\dagger ct/2} \\ &= \sum_{n,n'} \chi_{n,n'} e^{-\frac{\Gamma_{\text{eff}}t}{2}(n+n')}|n\rangle\langle n'|, \end{aligned} \tag{3.48}$$

and thus predicts an exponential decay proportional to the photon-number carried by the respective density-matrix component. The integral in the $\hat{J}$ term then yields an exponential saturation of the exited state according to

$$\begin{aligned} \Gamma_{\text{eff}} \int_0^t dt\, e^{\Gamma_{\text{eff}}\hat{L}t}\chi &= \Gamma_{\text{eff}} \sum_{n,n'} \chi_{n,n'} \int_0^t dt\, e^{-\frac{\Gamma_{\text{eff}}t}{2}(n+n')}|n\rangle\langle n'| \\ &= \sum_{n,n'} \chi_{n,n'} \frac{2}{n+n'}\left(1 - e^{-\frac{\Gamma_{\text{eff}}t}{2}(n+n')}\right)|n\rangle\langle n'|. \end{aligned} \tag{3.49}$$

Finally, the time-evolution of an initial product density-matrix $\rho = |G\rangle\langle G| \otimes \chi$ is given by

$$\begin{aligned} U(t)|G\rangle\langle G| \otimes \chi = |E\rangle\langle E| \otimes \sum_{n,n'} \chi_{n,n'} \frac{2\sqrt{nn'}}{n+n'}\left(1 - e^{-\frac{\Gamma_{\text{eff}}t}{2}(n+n')}\right)|n-1\rangle\langle n'-1| \\ + |G\rangle\langle G| \otimes \sum_{n,n'} \chi_{n,n'} e^{-\frac{\Gamma_{\text{eff}}t}{2}(n+n')}|n\rangle\langle n'|. \end{aligned} \tag{3.50}$$

The first term proportional to the excited state $|E\rangle\langle E|$ increases exponentially on a timescale governed by the number of photons in the respective light state. Conversely, the second term proportional to the ground-state $|G\rangle\langle G|$ shows an exponential decay on a corresponding timescale. In the scaling-limit, this results in a state

$$U(t\to\infty)|G\rangle\langle G|\otimes\chi = |E\rangle\langle E|\otimes\sum_{n,n'}\chi_{n,n'}\frac{2\sqrt{nn'}}{n+n'}|n-1\rangle\langle n'-1| + |G\rangle\langle G|\otimes\chi_{0,0}|0\rangle\langle 0|, \qquad (3.51)$$

where the probability for the two-state system to be in the excited state turns out to be $1-\chi_{0,0}$. In general, the resulting density-matrix does no longer correspond to a pure state due to the factor $1/(n+n')$ that prevents a decomposition according to $\chi=|\chi\rangle\langle\chi|$. Still, deviations from the initial state are small for large average photon-numbers. For instance, absorption of a single photon from a coherent state of light $|\alpha\rangle$ with density-matrix

$$\chi_0 = e^{-|\alpha|}\sum_{n,n'}\frac{\alpha^{*n}}{\sqrt{n!}}\frac{\alpha^{n'}}{\sqrt{n'!}}|n\rangle\langle n'|, \qquad (3.52)$$

results in a state

$$\chi_\infty = e^{-|\alpha|^2}\sum_{n,n'}\frac{2}{n+n'+2}\frac{\alpha^{n}\alpha^{*n'}}{\sqrt{n!n'!}}|n\rangle\langle n'|, \qquad (3.53)$$

which in general cannot be decomposed. Yet, in the limit of large α corresponding to a large average photon-number $n\approx|\alpha|^2$, this particular state closely resembles a coherent state with $\alpha'=\sqrt{\alpha^2-1}$. On the other hand, strong deviations occur for small $\alpha\approx 1$ (see Fig. 3.14). This fact also shows in the purity of the resulting state, which, renormalized by $\operatorname{tr}\chi_E$, takes the general form

$$\frac{\operatorname{tr}\chi_E^2}{\operatorname{tr}\chi_E} = \frac{1}{1-\chi_{0,0}}\sum_{n,m=0}|\chi_{n+1,m+1}|^2\left[1-\left(\frac{n-m}{n+m+2}\right)^2\right]. \qquad (3.54)$$

Again, for a coherent state $|\alpha\rangle$, this expression reduces to

$$\frac{\operatorname{tr}\chi_E^2}{\operatorname{tr}\chi_E} = \frac{1}{e^{\alpha^2}(e^{\alpha^2}-1)}\left(e^{2\alpha^2}-1+\gamma+\Gamma(0,-2\alpha^2)+\log(-2\alpha^2)\right), \qquad (3.55)$$

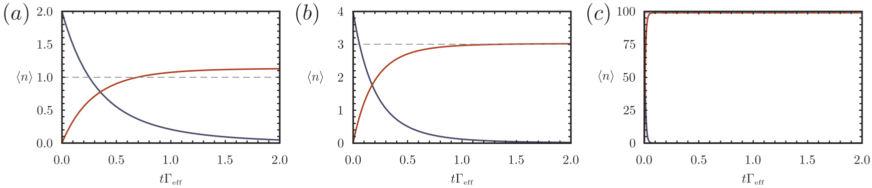

Figure 3.14: Average photon-number of a coherent state $|\alpha\rangle$ over time. The solid blue line is the part proportional to the ground-state of the absorber, whereas the solid red line is the part proportional to the excited state. The black dashed line depicts the naive expectation that the photon-number decrease by one, when a single photon is absorbed. The plot clearly shows that this naive estimate fails for small values α.

where $\Gamma(x, y)$ and γ denote the incomplete Gamma function and the Euler-Mascheroni constant, respectively. As one might expect, eq. (3.55) approaches unity for $\alpha \gg 1$. In addition, the calculation for a two-state saturating absorber can easily be generalized for an n-state system: The time-evolution is then given by $U_n(t) = [U(t)]^n$, and yields $n-1$ exponentially decaying states, and a single exponentially increasing state which carries n excitations.

3.C Pulsed Rabi-Frequency

A possible way to realise a system featuring inhomogeneous dephasing is to use a random but static detuning for each atom in combination with a pulsed Rabi-frequency. The main idea goes as follows: While the coupling laser is on, the collective ground-state is excited into the W-state with little dephasing due to the random detunings. On the other hand, the dead-time in between the pulses allows the W-state to acquire a large enough overlap with the dark subspace before the coherent driving de-excites the system again. More specifically, in a setup where a single pulse coherently transfers a fraction f of the collective ground-state population into the W-state, perfect dephasing accounts for a second transfer of a fraction $f(1 - 1/N)$ from the W-state population into the dark subspace. A subsequent pulse excites another fraction f of the remaining ground-state population, while only a fraction f^2/N is transferred back. The asymmetric transfer hence creates an exponential decay of the collective ground-state population for $f^2/N \ll 1$, where the effective decay-rate $\Gamma_{\text{pulse}} = -p \log(1 - f)$ is determined by the pulse-rate p

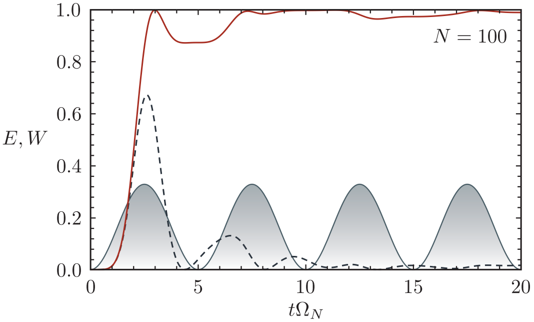

Figure 3.15: Time evolution for a system with static random detuning $\Delta \in [-\Omega, \Omega]$ and pulse-times $\Delta_{\text{pulse}} = 5\Omega_N$. The solid red line shows the probability E to be in the excited state, whereas the dashed blue line shows the probability to be in the W-state. The pulse-shape is sinusoidal, and indicated by the filled blue line. In the dead-time between the pulses, the dephasing accounts for a probability transfer from the W-state into the dark states, as can be seen around $t\Omega_N \approx 4$.

and the transfer fraction f. Such behavior can be studied by a straightforward numerical integration of the coherent dynamics with a pulsed control-laser. The amount of population transfer within each pulse is determined by the pulse-area $\int_0^T dt\, \Omega_N(t)$; optimal transfer is achieved for a π-pulse with $\Omega_N \approx \pi/T$, while the shape of the pulse plays a minor role. On the other hand, it is desirable that within each pulse individual states acquire a phase-shift $\psi_i = \Delta_i t$ that is on the order of π. Indeed the numerical analysis confirms these expectation (see Fig. 3.15) and even a sinusoidal modulation of the coupling laser leads to a very fast dephasing.

CHAPTER 4

Quantum-Motion of a Topological Defect

4.1 Motivation

Efforts to demonstrate quantum-behavior of macroscopic objects, especially ones that can be seen by the naked eye, have attracted considerable interest [80–83]. The fundamental difficulty in observing quantum-effects on a macroscopic scale is due to the huge number of degrees of freedom involved [84]. Those all individually couple to the environment and, as a result, experience a slightly different interaction that is responsible for a loss of coherence in between the constituents and thereby their capability to interfere [85]. Yet, a topological excitation is not characterized by its local degrees of freedom [86], but rather by a non-trivial topology of a macroscopic order-parameter. The latter represents a non-local quantity that features an extensive energy gap, and is thus stable despite local perturbations. In concert with the remarkable progress in the control over cold atomic gases this opens the path to realise such states in an idealized environment [1]. Here we ask the simple question whether a macroscopic object such as a topological excitation can show quantum-behavior. In particular, we consider a quantum vortex in a cold atomic gas confined to an optical lattice, and show that it can exhibit interference-effects.

The application of classical hydrodynamic considerations in describing vortex-dynamics in a continuous superfluid has proven to be remarkably successful even for a low number of vortices [87]. This is mostly due to the fact that the vortex de Broglie wavelength decreases with decreasing interaction between the superfluid particles [88]. As a result, the healing-length for a weakly interacting system such as a cold atomic gas is much larger than its de Broglie wavelength and, accordingly, so is the spatial dimension of the vortex-core. Moreover, the vanishing superfluidity in the core gives rise to dissipation and hence quantum effects are further suppressed [89–91]. On the other hand, strongly-correlated systems such as d-wave superconductors [92] or cold atoms in an optical lattice close to the Mott-insulator transition might exhibit quantum-motion of vortices [90, 93]. Indeed, the latter system allows for near arbitrary tuning of the healing-length via external fields, and is thus a prime candidate for observing quantum-effects of topological excitations. If we assume the vortex core to be smaller than the lattice spacing, the vortex itself is pinned to the plaquettes of the lattice [94–96], and dissipative effects due to the finite core size vanish. On the other hand, the vortex is allowed to tunnel from one pinning-site to the other, with the tunneling rate being governed by the global properties of the superfluid phase rather than a local one [93]. The tunneling of vortices in cold atoms has been investigated previously in both a homogeneous system with two pinning-sites [97–99] as well as in a lattice in the context of hall conductivity of hard-core bosons [91, 100, 101]. Yet a thorough investigation that focuses on the signatures of quantum-motion of individual vortices is missing so far.

In this chapter we study the behavior of quantum vortices in a cold atomic gas confined to an optical lattice. In concert with a Feshbach-resonance the latter allows us to tune the interactions between the superfluid particles and thereby control their fluctuations. We are particularly interested in the regime close to the Mott-insulator transition, with a large average number of superfluid particles per lattice site. In combination these conditions lead to a small vortex-core as well as negligible density-fluctuations, and thus drive the vortices into the quantum-regime. In turn, the vortices are confined to the plaquettes of the optical lattice. Starting from a two-dimensional Bose-Hubbard model with repulsive interactions we derive an effective theory for the vortex degrees of freedom in terms of a tight-binding model on the dual lattice sites associated with the plaquettes of the original lattice. In analogy to the classical hydrodynamic theory we find that a moving vortex acquires a Berry-phase due to the superfluid filling and exhibits a logarithmic interaction-potential for other vortices. The former then leads to an effective magnetic field and in turn to a Lorentz-like force acting on a moving vortex. In addition, the finite tunneling-amplitude gives rise to a finite vortex mass induced by the underlying lattice, for which we provide an analytic expression. Last, we discuss the fundamental differences between classical and quantum vortex motion and comment on the possibility to realise a vortex interference-experiment within a cold atomic setup.

4.2 Mapping from Bose-Hubbard to Vortex Degrees of Freedom

4.2.1 Gauged Bose-Hubbard Model

We start with the two-dimensional gauged Bose-Hubbard model [102, 103],

$$H = -w \sum_{\langle i,j \rangle} a_i^\dagger a_j e^{iA_{ij}} + a_j^\dagger a_i e^{-iA_{ij}} + \frac{U}{2} \sum_i n_i(n_i - 1) + \mu \sum_i n_i, \tag{4.1}$$

where $a_i^\dagger$ (a_i) creates (annihilates) a bosonic particle on site i of the two-dimensional lattice and $n_i = a_i^\dagger a_i$ counts the number of superfluid particles on site i. The operators need to be supplemented with an algebra that constitutes the appropriate commutation relation, namely $[a_i, a_j^\dagger] = \delta_{i,j}$. Moreover, w and U are the particle hopping rate and on-site interaction parameter, respectively, whereas μ is a global chemical potential. The phase A_{ij} acquired at every hop is due to an artificial external magnetic field B_I perpendicular to the plane, and thus fulfills the relation

$$\sum_{\square} A_{ij} = B_I, \tag{4.2}$$

where $\sum_\square$ denotes the summation around a plaquatte I of the lattice. This magnetic field will later act as a chemical potential for the vortices. Such a system can easily be realised within a cold atomic setup [103], where either rotation [104] or external lasers in concert with internal degrees of freedom [105] are used in order to create the effective magnetic field for the neutral atoms. For our intents it is convenient to express the Hamiltonian (4.1) in terms of a coherent state path-integral [106], where we use a basis

$$|\{\psi_i\}\rangle = \exp\left[\sum_i \psi_i a_i^\dagger\right] |\text{vac}\rangle. \tag{4.3}$$

Here, ψ_i is the probability-amplitude to find a particle in the Wannier state created by the operator $a_i^\dagger$. In imaginary time $\tau \to -it$, the action of the Bose-Hubbard model (4.1) reads

$$\begin{aligned} S_{\mathrm{BH}}^{\psi} &= \int_0^{\hbar\beta} d\tau \sum_i \psi_i^*(\hbar\partial_\tau - \mu)\psi_i - w \sum_{\langle i,j\rangle} \psi_i^*\psi_j e^{iA_{ij}} + c.c. + \frac{U}{2}\sum_i |\psi_i|^2(|\psi_i|^2 - 1) \\ &= \int_0^{\hbar\beta} d\tau\, \mathcal{L}(\{\psi_i\}). \end{aligned} \tag{4.4}$$

In the following we provide a transformation that shifts our point of view from the particle description in (4.1) towards a vortex description.

4.2.2 Quantum Phase Model

A vortex is a point defect in the phase of a superfluid carrying a non-zero winding number q [86], where the singular point of the phase then marks the position of the vortex core. In order to derive an effective model for the dynamics of these topological quasi-particles, we need to cast the gauged Bose-Hubbard (4.1) model in terms of this very phase variable ϕ. According to ref. [107], this can be achieved via the relation $\psi_i = \sqrt{\bar{n} + \delta n_i}\, e^{i\phi_i}$, giving rise to the action

$$\begin{aligned} S_{\mathrm{QPM}}^{n\phi} = \int_0^{\hbar\beta} d\tau \sum_i \left[\frac{1}{2}\hbar\dot{\delta n_i} + i\hbar\dot{\phi}_i(\delta n_i + \bar{n})\right] \\ - 2w \sum_{\langle i,j\rangle} \sqrt{\bar{n} + \delta n_i}\,\sqrt{\bar{n} + \delta n_j}\cos(\phi_{ij} + A_{ij}) + \frac{U}{2}\sum_i \delta n_i^2, \end{aligned} \tag{4.5}$$

with $\phi_{ij} = \phi_i - \phi_j$. Moreover, we split the local superfluid filling n_i into an average filling $\bar{n}$ and local fluctuations δn_i under the assumption that $\sum_i \langle \delta n_i \rangle = 0$. Note that the phase ϕ_i and the superfluid fluctuations δn_i are conjugate variables and, in quantized form, their operators fulfill the commutation relation $[\phi_i, \delta n_j] = i\delta_{ij}$. The factor $\dot{\delta n}$ in the first term of eq. (4.5) is a total time-derivative and hence can be dropped, whereas the topological term $i\dot{\phi}\bar{n}$ accounts for the Magnus-force for non-integer $\bar{n}$, as is shown in section 4.3.3.

At this point we need to apply the first of two approximations, namely that the fluctuations of the superfluid δn are much smaller than the average superfluid

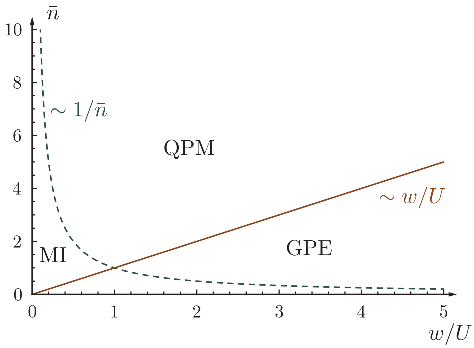

Figure 4.1: Regime of validity for the Quantum Phase model. Below the dashed-blue line, the system enters the Mott-insulating regime, where phase-coherence between different lattice sites is lost. The solid red line marks the transition into the Galilei-invariant Gross-Pitaevskii regime. There, the healing-length exceeds the lattice-spacing, and strong density-fluctuations on the individual lattice sites occur.

filling $\bar{n}$. This allows us to replace the non-local factor in the second term by a global one, that is $\sqrt{\bar{n}+\delta n_i}\sqrt{\bar{n}+\delta n_j} \rightarrow \bar{n}$, and ultimately leads to the definition of the superfluid stiffness $K = 2w\bar{n}$. As is shown in ref. [107], the regime of validity for this approximation is given by

$$\frac{1}{\bar{n}^2} \ll \frac{U}{\bar{n}w} \ll 3. \tag{4.6}$$

The lower boundary of eq. (4.6) is the transition into the Galilei-invariant regime, where the lattice is but a small perturbation. In this regime, one needs not refer to the Bose-Hubbard model for an adequate description, but rather use the Galilei-invariant Gross-Pitaevskii equation. Conversely, the upper boundary marks the transition to the Mott-insulator, where any phase-correlations in between lattice sites is lost [14]. Even so, for large enough superfluid filling factors $\bar{n}$, there is an intermediate regime where the above approximation is justified.

The next step is then to integrate over the remaining superfluid fluctuations δn_i, and yields the action of the reduced Quantum-Phase model (rQPM),

$$S^{\phi}_{\mathrm{rQPM}} = \int_0^{\hbar\beta} d\tau \sum \frac{\hbar^2 \dot{\phi_i}^2}{2U} + \sum_i i\hbar\dot{\phi}_i\bar{n} - K\sum_{\langle i,j\rangle}\cos(\phi_{i,j} + A_{i,j}). \tag{4.7}$$

Here it is important to note that the only dynamical variable is the local phase ϕ_i and its time-derivatives. Yet the non-linear cosine-term accounts for the highly non-trivial features of the model, and in particular allows for multivalued solutions such as vortex excitations. In order to deal with the cosine-term we follow the ideas developed in solid-state theory in the context of the XY-model, and perform a duality-transformation [108]. The first step is a Villain-transformation (see ref. [109])

$$e^{K\cos\phi} \to \sum_{l=-\infty}^{\infty} e^{-\frac{1}{2K}l^2 - il\phi}, \tag{4.8}$$

which marks the second approximation in this calculation. It allows us to remove the non-linear cosine-term at the cost of an additional field l that we interpret as the superfluid current. The applicability of the Villain-transformation is based on large prefactors K. Since $K \sim \bar{n}$, this condition is equivalent to the lower boundary of the validity of the Quantum Phase model (see eq. (4.6)). By carrying out the Villain-transformation on every lattice link $\langle i,j\rangle$, the resulting action takes the form

$$\begin{aligned} S^{l\phi}_{\mathrm{rQPM}} = \int_0^{\hbar\beta} d\tau \sum_i \frac{1}{2U}\left(\hbar\dot{\phi}_i + iU\bar{n}\right)^2 + \frac{1}{2K}\sum_{\langle i,j\rangle} l^2_{i,j} \\ + \sum_i i\phi_i\left(\sum_{j\in i} l_{i,j}\right) + \sum_{\langle i,j\rangle} il_{i,j}A_{i,j}, \end{aligned} \tag{4.9}$$

where we dropped the constant term $\sim Un^2$. The short-hand notation $\sum_{j\in i}$ describes the summation over all lattice sites j adjacent to site i, and is thus the lattice equivalent to the divergence for the l's. A subsequent integration over the phase variables ϕ_i yields the action in terms of the superfluid currents l alone,

$$\begin{aligned} S^{l}_{\mathrm{rQPM}} = \int_0^{\hbar\beta} d\tau \sum_i \sum_{j\in i} l_{i,j}\left(-\frac{U}{2\hbar^2\partial_\tau^2}\right)\sum_{j'\in i} l_{i,j'} + \sum_i \frac{U\bar{n}\tau}{\hbar}\left(\sum_{j\in i} l_{i,j}\right) \\ + \frac{1}{2K}\sum_{\langle i,j\rangle} l^2_{i,j} + \sum_{\langle i,j\rangle} il_{i,j}A_{i,j}. \end{aligned} \tag{4.10}$$

In analogy to common electrodynamics [110], we now rewrite the superfluid currents l corresponding to the electromagnetic field in terms of potential-derivates $l_{i,j} = h_I - h_J - \hbar\partial_\tau f_{JI}$. Here, h_I and f_{JI} are a scalar- and vector-potential, respectively, and are defined on the plaquettes I and their respective links $\langle IJ \rangle$. A geometric interpretation of this mapping is a $\pi/2$-rotation of every lattice current $l_{i,j}$, with the rotation axis center situated on the links of the original lattice, see Fig. (4.2). For the sake of brevity, we again denote $h_I - h_J = h_{IJ}$. A consequence of this particular mapping is that the divergence-term $\left(\sum_{j\in i} l_{i,j}\right)$ on the original lattice turns into a curl-term on the dual lattice, as

$$\left(\sum_{j\in i} l_{i,j}\right) = -\hbar\partial_\tau \sum_{\square} f_{JI}, \tag{4.11}$$

and the $\square$ denotes summation over the edges of one lattice plaquette. Note that only the link variables f_{JI} contribute to eq. (4.11), whereas the local field h_I drops out.

An integration by parts allows us to remove the inconvenient time-derivatives $\partial_\tau f$, which, in retrospect, justifies the definition of f as a time-derivative in the first place. In particular, for the term coupling the magnetic vector-potential A_{JI} to the vector-potential $\partial_\tau f_{JI}$ this yields the expression $f_{JI}\partial_\tau A_{JI}$. In Weyl gauge, the time-derivative of the vector-potential is an electric field for the superfluid particles, namely $\partial_\tau A_{ij} = F$. Since the superfluid particles have unit charge, the external electric field is equivalent to an external force F. Yet, for the sake of clarity, we henceforth assume $F = 0$. On the other hand, we can use the definition of the magnetic field eq. (4.2) in order to express the summation of the A_{JI} over one plaquette as $\sum_{J\in I} A_{IJ} = B_I$, which explicitly shows the gauge invariance of the theory with respect to the external field. Upon dropping a constant term $\sim U\bar{n}^2$ that arises due to a completion of the square, we are thus left with the discrete electromagnetic action

$$\begin{aligned} S^{hf}_{\mathrm{rQPM}} = \int_0^{\hbar\beta} d\tau \, \frac{U}{2} \sum_I \left(\bar{n} + \sum_{\square} f_{JI}\right)^2 \\ + \frac{1}{2K} \sum_{\langle I,J\rangle} \left(h_{IJ} - \hbar\partial_\tau f_{JI}\right)^2 + i \sum_I h_I B_I. \end{aligned} \tag{4.12}$$

Last, we perform a poisson summation which renders the action in terms of the

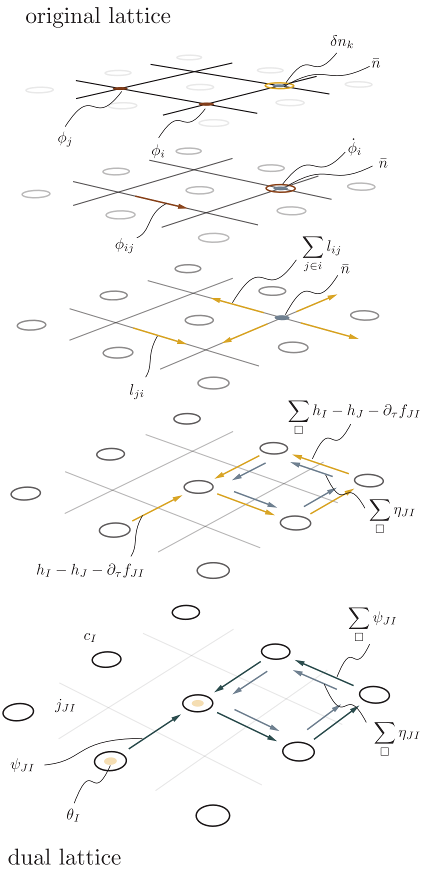

Figure 4.2: Diagrammatic representation of the mapping. We start from the Bose-Hubbard model described by the phase and density on the individual lattice sites. The density-fluctuations can then be integrated out, and give rise to a dependence on the time-derivative of the local phases ϕ_i. A subsequent Villain-transformation allows us to replace the phases ϕ_i by superfluid currents l_{ij} defined on the links of the lattice. In analogy to electrodynamics, we introduce the discrete scalar- and vector-potential h_I and f_{JI}, respectively. In order to remove the discreteness from the fields, we apply a Poisson-summation, and obtain continuous fields θ_I and ψ_{JI} at the cost of discrete charges q_I and currents j_{JI} representing the vorticity and the vortex current, respectively.

continuous potentials $\tilde{\theta}$ and $\tilde{\psi}$ as well as the discrete charges q_I and their respective currents j_{IJ},

$$S_{\text{rQPM}}^{\tilde{\theta}\tilde{\psi}} = \int_0^{\hbar\beta} d\tau \, \frac{U}{2} \sum_I \left(\bar{n} + \sum_{\Box} \tilde{\psi}_{JI} \right)^2 + \frac{1}{2K} \sum_{\langle I,J \rangle} (\tilde{\theta}_{IJ} - \hbar\partial_\tau \tilde{\psi}_{JI})^2$$
$$- 2\pi i \sum_I \tilde{\theta}_I \left(q_I - \frac{B_I}{2\hbar\pi} \right) - 2\pi i\hbar \sum_{\langle I,J \rangle} \tilde{\psi}_{JI} j_{JI}. \qquad (4.13)$$

The charges q_I and currents j_{JI} will be interpreted as vortex-density and -current later on. Note that the magnetic field B_I modifies the coupling of the vortex *charge* (vorticity) to the scalar potential $\tilde{\theta}_I$, and thus acts as a chemical potential for the vortices.

It is convenient for the following treatment to define a field η_{IJ} via $\bar{n} = \sum_{\Box} \eta_{JI}$. We can then write eq. (4.13) in the compact notion $\sum_{\Box} \psi_{JI}$, with $\psi_{JI} = \tilde{\psi}_{JI} + \eta_{JI}$, and find a coupling of the current j_{JI} to the background superfluid η_{JI} that leads to a phase shift for a vortex moving from one site to another. As will be shown in section 4.4.2, this term creates an effective magnetic field for the vortices. Yet, since $\bar{n}$ and hence η_{JI} are constant in time, $\partial_\tau \tilde{\psi}_{JI} = \partial_\tau \psi_{JI}$. It follows that the action of the vortex model then takes the final form

$$S_{\text{rQPM}}^{\theta\psi} = \int_0^{\hbar\beta} d\tau \, \frac{U}{2} \left[\sum_I \left(\sum_{\Box} \psi_{JI} \right)^2 + \sum_{\langle I,J \rangle} (\theta_{IJ} - \partial_{c_s\tau} \psi_{JI})^2 \right]$$
$$- 2\pi i\hbar \sum_I \theta_I c_s \left(q_I - \bar{B} \right) - 2\pi i\hbar \sum_{\langle I,J \rangle} (\psi_{JI} - \eta_{JI}) \, j_{JI}, \qquad (4.14)$$

where we further absorbed the sound-velocity $c_s = \sqrt{UK}/\hbar$ in the definition of $\theta_I = \tilde{\theta}_I / c_s$. Since the lattice spacing is a dimensionless quantity, the effective chemical potential $\bar{B}_I = B_I / 2\pi\hbar$ is but the magnetic flux B_I divided by the flux-quantum $2\pi\hbar$. As already mentioned above, the action (4.14) is formally equivalent to a theory of charged particles on a two-dimensional lattice. The vortices play the role of the positive or negative charges, depending on their respective vorticity, whereas the superfluid phonon modes correspond to the electromagnetic fields mediating the interaction [111]. In analogy to electrodynamics, one can cast the action (4.14) in terms of (2+1)-vectors

$$\chi_I = \begin{pmatrix} \theta_I \\ \psi_I^{\hat{x}} \\ \psi_I^{\hat{y}} \end{pmatrix}, \quad j_I = \begin{pmatrix} c_{\mathrm{s}}(q_I - \bar{B}_I) \\ j_I^{\hat{x}} \\ j_I^{\hat{y}} \end{pmatrix}, \tag{4.15}$$

where $\hat{x}$ and $\hat{y}$ are mere directional indices. In this covariant form, the action (4.14) reads

$$S_{\mathrm{rQPM}}^{\chi} = \int_0^{\hbar\beta} d\tau \, \frac{U}{2} \sum_{I,J} \chi_I \Delta_{I,J} \chi_J - 2\pi i\hbar \sum_I \chi_I j_I + 2\pi i\hbar \sum_I \eta_I j_I, \tag{4.16}$$

where $\Delta_{I,J}$ is the coupling-matrix between the phonon-fields χ_I. Since we are only interested in the vortex degrees of freedom, we can integrate over the phonon field χ_I, and are left with

$$S_{\mathrm{rQPM}}^{j} = -\frac{(2\pi\hbar)^2}{2U} \int_0^{\hbar\beta} d\tau \int_0^{\hbar\beta} d\tau' \sum_{I,J} j_I \Delta_{I,J}^{-1} j_J + 2\pi i\hbar \int_0^{\hbar\beta} d\tau \sum_I \eta_I j_I. \tag{4.17}$$

The explicit form of the Green's-function $\Delta_{I,J}^{-1}$ will be discussed in the next section.

4.2.3 Lattice Green's-Function

We now turn towards our actual goal, that is to calculate the vortex-action on a square lattice. Unfortunately, the relatively short continuum calculation (see appendix 4.A) turns quite extensive and rather cumbersome on a lattice, and is thus banished to appendix 4.B. We find that the interaction-matrix on the lattice may be written as

$$\Delta_{IJ} = \int d\omega \, e^{i\omega\tau} \int \frac{d^2k}{(2\pi)^2} e^{i\mathbf{k}(\mathbf{x}_I - \mathbf{x}_J)} \Delta_{\mathbf{k},\omega}^{\mathrm{reg}}, \tag{4.18}$$

with the regularized interaction-matrix (see appendix 4.B)

$$\Delta_{\mathbf{k},\omega}^{\mathrm{reg}} = \left(\frac{\omega^2}{c_{\mathrm{s}}^2} + 4 \left[\sin^2 \frac{k_x}{2} + 4 \sin^2 \frac{k_y}{2} \right] \right) \mathrm{id}, \tag{4.19}$$

and the identity matrix id. Since $\Delta^{\mathrm{reg}}_{\mathbf{k},\omega}$ is diagonal, it can easily be inverted. The resulting lattice Green's-function is then given by

$$\Delta^{-1}_{IJ}(\tau) = \mathrm{id}\,\Lambda^{-1}_{IJ}(\tau), \tag{4.20}$$

with the one-dimensional propagator

$$\Lambda^{-1}_{IJ}(\tau) = \int \frac{d\omega}{2\pi} \int \frac{d^2k}{(2\pi)^2} \, \frac{e^{i\mathbf{k}(\mathbf{x}_I - \mathbf{x}_J) + i\omega\tau}}{\omega^2/c_{\mathrm{s}}^2 + 4\left[\sin^2\frac{k_x}{2} + \sin^2\frac{k_y}{2}\right]}. \tag{4.21}$$

4.3 Effective Vortex Lattice Model

4.3.1 Definition of the Vortex Current

Analog to the expression for the vortex current in the continuum provided by D. Lee and M.P.A. Fisher [112], the vortex current on a lattice takes the form

$$j^0_I = c_{\mathrm{s}} \sum_{i,n_i} q^i \delta_{I,I_{n_i}} \left[\Theta(\tau - \tau_{n_i}) - \Theta(\tau - \tau_{n_i+1})\right], \tag{4.22}$$

$$j_{JI} = \sum_{i,n_i} q^i \delta_{\langle IJ\rangle,\langle I_{n_i-1} I_{n_i}\rangle} \delta(\tau - \tau_{n_i}). \tag{4.23}$$

Here, $q^i = \pm 1$ is the integer vorticity, Θ is the Heaviside step-function and τ_{n_i} is the time when the n_i-th hop from site I_{n_i-1} to site I_{n_i} occurs. The particular site I_{n_i} can be written as a sum over all previous jumps,

$$I_{n_i} = I_{0_i} + \sum_{m_i=0}^{n_i} \hat{\mu}_{m_i}, \tag{4.24}$$

with $\hat{\mu} = \hat{x}, \hat{y}$ denoting the direction of the n-th jump. Therefore, I_{n_i} is the lattice trajectory of a vortex. This rather complicated form of the lattice current as compared to the continuum version is due to the current being defined on the lattice links, in contrast to the density that is defined on the lattice itself. Fortunately, we will only need the most basic versions of this expression, namely the *current* of two static vortices sitting at sites Y and Z, respectively, and the current of a vortex which performs a single jump from one site to another.

4.3.2 Vortex-Vortex Interaction

In order to calculate the vortex-vortex interaction potential on a lattice, we assume two vortices to sit at sites Y and Z, respectively. Thus, the constant (2+1)-current takes the trivial form

$$j_I = \begin{pmatrix} c_{\mathrm{s}} q_Y \delta_{I,Y} + c_{\mathrm{s}} q_Z \delta_{I,Z} \\ 0 \\ 0 \end{pmatrix}. \tag{4.25}$$

We can write the action for such a configuration by the use of the eqs. (4.17) and (4.20), and find the action

$$S_{\mathrm{int}} = \frac{(2\pi\hbar)^2 c_{\mathrm{s}}^2 q_Y q_Z}{U} \int d\tau d\tau' \Delta^{-1}_{YZ}(\tau - \tau'), \tag{4.26}$$

under the assumption that fluctuations do not contribute [106]. Moreover, we neglect any self-interaction terms, since those would be present regardless of the presence of a second vortex, and only keep track of the cross-terms describing the interaction between the vortices (thus, the factor of 2). The time-integral over the Green's-function then reduces to

$$\int d\tau d\tau' \bar{\Delta}^{-1}_{YZ}(\tau - \tau') = \left(\int d\tau\right) \int \frac{d^2k}{(2\pi)^2} \frac{e^{i\mathbf{k}(\mathbf{x}_Y - \mathbf{x}_Z)}}{4\left[\sin^2\frac{k_x}{2} + \sin^2\frac{k_y}{2}\right]}. \tag{4.27}$$

The integral over time in the brackets yields the time interval of our observation, whereas the integral over the momentum k gives the actual interaction energy. According to ref. [113], the latter integral can be well approximated via

$$\int \frac{d^2k}{(2\pi)^2} \frac{e^{i\mathbf{k}(\mathbf{x}_Y - \mathbf{x}_Z)}}{4\left[\sin^2\frac{k_x}{2} + \sin^2\frac{k_y}{2}\right]} \approx 2\pi \log|\mathbf{x}_Y - \mathbf{x}_Z| + const. \tag{4.28}$$

for large inter-vortex distances as compared to the (dimensionless) lattice spacing, i.e. $|\mathbf{x}_1 - \mathbf{x}_2| \gg 1$. We therefore recover the logarithmic interaction potential between vortices as is found in the continuum hydrodynamic description. By neglecting the constant terms, we are left with the action

$$S_{\mathrm{int}} = \left(\int d\tau\right) 4\pi^2 q_Y q_Z \bar{n} w 2\pi \log|\mathbf{x}_Y - \mathbf{x}_Z|, \tag{4.29}$$

where we used $c_\mathrm{s}^2 = UK/\hbar^2 = \bar{n}wU/\hbar^2$. Note that this is in agreement with the model used in ref. [101].

4.3.3 Instanton Action

The current generated by a single vortex hopping at time $\tau = 0$ from site Y to site $Y + \hat{x}$ cast in terms of the $(2+1)$-vector notation takes the form

$$j_I = q \begin{pmatrix} c_\mathrm{s} \left[\delta_{I,Y}\Theta(-\tau) + \delta_{I,Y+\hat{x}}\Theta(\tau)\right] \\ \delta_{I,Y}\delta(\tau) \\ 0 \end{pmatrix}. \tag{4.30}$$

If we neglect any fluctuations in the bounce, the instanton-action reads

$$S_\mathrm{inst}^\mathrm{phonon} = \frac{(2\pi\hbar)^2}{2U} \int d\tau d\tau' \sum_{I,J} j_I(\tau) \Delta_{IJ}^{-1}(\tau - \tau') j_J(\tau'). \tag{4.31}$$

It is important to note that this action only takes phase-fluctuations into account, whereas it neglects density-fluctuations as well as the structure of the vortex core. However, the former approximation is justified since we are interested in the regime close to the Mott-insulator transition, where density-fluctuations are suppressed. For the sake of clarity we split the below calculation into its spatial- and time-component.

By inserting a single vortex tunneling from Y to $Y + \hat{x}$ in the spatial component of the general instanton-action (4.31), we find the the expression

$$S_\mathrm{inst}^\mathrm{space} = \frac{(2\pi\hbar)^2 q^2}{2U} \int d\tau d\tau' \delta(\tau)\delta(\tau') \Delta_{YY}^{-1}(\tau - \tau') = \frac{(2\pi\hbar)^2 q^2 c_\mathrm{s}}{2U} \bar{\Lambda}_{YY}^{-1}(0). \tag{4.32}$$

Here we introduced the rescaled Green's-function $\bar{\Lambda}_{YY}^{-1}(\tau/c_\mathrm{s}) = \Lambda_{YY}^{-1}(\tau)/c_\mathrm{s}$ in the last step. Explicitly, the rescaled Green's-function takes the form

$$\bar{\Lambda}_{YY}^{-1}(0) = \int \frac{d\omega/c_\mathrm{s}}{2\pi} \int \frac{d^2k}{(2\pi)^2} \frac{1}{\omega^2/c_\mathrm{s}^2 + 4\left[\sin^2\frac{k_x}{2} + \sin^2\frac{k_y}{2}\right]}, \tag{4.33}$$

and is but a numerical constant. Numerical integration yields the approximate value of $\bar{\Lambda}^{-1}_{YY}(0) \approx 1/3$, with which the action (4.32) reads

$$S^{\text{space}}_{\text{inst}} \approx \frac{2\pi^2\hbar}{3}\sqrt{\frac{K}{U}}. \tag{4.34}$$

The time component of the instanton-action (4.31) for a tunneling vortex (4.30) is more involved: First, note that the instanton-action takes the form

$$\begin{aligned} S^{\text{time}}_{\text{inst}} = \frac{(2\pi\hbar)^2}{2U}\int d\tau d\tau' c_{\text{s}}^2 q^2 c_{\text{s}} \Big[&\Theta(-\tau)\Theta(-\tau')\bar{\Lambda}_0^{-1} + \Theta(-\tau)\Theta(\tau')\bar{\Lambda}^{-1}_{-\hat{x}} \\ &+ \Theta(\tau)\Theta(-\tau')\bar{\Lambda}_{\hat{x}}^{-1} + \Theta(\tau)\Theta(\tau')\bar{\Lambda}_0^{-1}\Big], \end{aligned} \tag{4.35}$$

where we have introduced the short-hand notation for the scalar Green's-functions $\bar{\Lambda}_0^{-1} = \bar{\Lambda}^{-1}_{Y,Y}(\tau - \tau')$ and $\bar{\Lambda}_{\hat{x}}^{-1} = \bar{\Lambda}^{-1}_{Y+\hat{x},Y}(\tau - \tau')$ in order to conserve space. From this we need to subtract the action created by a stationary vortex, namely a vortex that sits on site Y for the entire time of observation,

$$S^{\text{time}}_{\text{stationary}} = \frac{(2\pi\hbar)^2}{2U}\int d\tau d\tau' \sum_{I,J} c_{\text{s}}^2 q^2 c_{\text{s}} \bar{\Lambda}_0^{-1}. \tag{4.36}$$

Since the Green's-function is translationally invariant, $\bar{\Lambda}^{-1}_{YY}(\tau - \tau') = \bar{\Lambda}^{-1}_{Y+\hat{x},Y+\hat{x}}$, subtracting the action of a stationary vortex cancels the first and last term in eq. (4.35). In consequence, we obtain the regularized instanton-action

$$\begin{aligned} \bar{S}^{\text{time}}_{\text{inst}} &= S^{\text{time}}_{\text{inst}} - S^{\text{time}}_{\text{stationary}} \\ &= \frac{(2\pi\hbar)^2}{2U}\int d\tau d\tau' c_{\text{s}}^2 q^2 c_{\text{s}} \Big[\Theta(-\tau)\Theta(\tau')(\bar{\Lambda}^{-1}_{-\hat{x}} - \bar{\Lambda}_0^{-1}) \\ &\qquad + \Theta(\tau)\Theta(-\tau')(\bar{\Lambda}_{\hat{x}}^{-1} - \bar{\Lambda}_0^{-1})\Big]. \end{aligned} \tag{4.37}$$

The difference $\bar{\Lambda}^{-1}_{-\hat{x}} - \bar{\Lambda}_0^{-1}$ between the two Green's-functions can easily be calculated, and gives rise to the explicit expression

$$\begin{aligned} [\bar{\Lambda}^{-1}_{-\hat{x}} - \bar{\Lambda}_0^{-1}](\tau - \tau') = &\int \frac{d\omega/c_{\text{s}}}{2\pi}\, e^{c_{\text{s}}(\tau-\tau')\frac{\omega}{c_{\text{s}}}} \\ &\times \int \frac{d^2k}{(2\pi)^2} \frac{e^{+i\mathbf{k}\hat{x}} - 1}{\omega^2/c_{\text{s}}^2 + 4\left[\sin^2\frac{k_x}{2} + \sin^2\frac{k_y}{2}\right]}. \end{aligned} \tag{4.38}$$

Integration over the respective time domains ($\tau > 0, \tau' < 0$ or $\tau < 0, \tau' > 0$; Note that both domains give the same contribution, and in turn allows us to add both in eq. (4.37) in order to get rid of the imaginary parts) yields

$$\bar{S}_{\text{inst}}^{\text{time}} = \frac{(2\pi\hbar)^2 q^2 c_{\text{s}}}{2U} \int \frac{d^2k}{(2\pi)^2} \frac{-\sin^2\frac{k_x}{2}}{4\left(\sin^2\frac{k_x}{2} + \sin^2\frac{k_y}{2}\right)^{3/2}}. \tag{4.39}$$

Again, the integral in eq. (4.39) is a purely numerical factor that, surprisingly, is half of $-\bar{\Lambda}_{YY}^{-1}(0)$ (on a numerical precision of 10^{-9}). This intriguing relation hints on a hidden symmetry between the two contributions, which has proven to be elusive so far. In total, the time-component of the instanton-action takes the form

$$\bar{S}_{\text{inst}}^{\text{time}} \approx -\frac{\pi^2\hbar}{3}\sqrt{\frac{K}{U}}. \tag{4.40}$$

The full phonon instanton action then reads

$$S_{\text{inst}}^{\text{phonon}} = S_{\text{inst}}^{\text{space}} + \bar{S}_{\text{inst}}^{\text{time}} \approx \frac{\pi^2\hbar}{3}\sqrt{\frac{K}{U}}. \tag{4.41}$$

and marks the main result of this section.

The coupling between the vortex current j and the background superfluid density $\bar{n}$ expressed in terms of the vector-potential η gives rise to a phase shift for a vortex hopping from one site to another. In particular, the phase shift of a single hopping process is

$$S_{\text{inst}}^{\text{Magnus}} = 2\pi\hbar i \int d\tau \sum_I \eta_I j_I = 2\pi\hbar i \int d\tau \sum_I \eta_{JI} j_{JI}. \tag{4.42}$$

Henceforth, we assume η to be given in Landau-gauge $\eta_{I,I+\hat{y}} = \bar{n}(\mathbf{x}_I \cdot \hat{x}) = \bar{n}x_I$ and $\eta_{I,I+\hat{x}} = 0$. A hopping process from site I to site $I + \hat{y}$ therefore yields the instanton-action

$$S_{\text{inst}}^{\text{Magnus}} = 2\pi\hbar i \int d\tau \sum_I \eta_{I,I+\hat{y}} q_Y \delta_{I,Y} \delta(\tau) = 2\pi\hbar i \bar{n} q_Y x_Y. \tag{4.43}$$

The i in this action ensures that the contribution due to the superfluid coupling is indeed a phase factor, and accounts for the *effective magnetic field* felt by a vortex. The *field strength* is then equal to the average particle filling $\bar{n}$, as can easily be seen by calculating the accumulated phase of a vortex moving around a single plaquette of the dual lattice. For integer $\bar{n}$, the phase is a multiple of 2π, and yields an overall factor of one due to $x_I \in \mathbb{Z}$. As a matter of fact, the effective magnetic field is only defined modulo 2π. This simple fact has but sever consequences for both the effective magnetic field felt by the vortices as well as the Hall-conductivity of the superfluid particles [114], and will be discussed in section 4.4.2.

Note that in the above calculation, we neglected any contribution due to the vortex core. We justified this approximation *a priori* by assuming that the healing-length is much smaller than the lattice spacing, $\xi \ll 1$. A rigorous proof of this assumption can be obtained by following Feigelman et al. [115], who estimated the instanton-action of a tunneling vortex core to be $S_{\text{inst}}^{\text{core}} \sim \hbar\bar{n}\xi^2$. In turn, this leads to the condition

$$1 \ll \frac{S_{\text{inst}}^{\text{phonon}}}{S_{\text{inst}}^{\text{core}}} \approx \frac{\sqrt{\bar{n}w/U}}{\bar{n}\xi^2} = \frac{\sqrt{\bar{n}w/U}}{\bar{n}\frac{w}{U\bar{n}}} = \sqrt{\frac{U\bar{n}}{w}}. \tag{4.44}$$

Incidentally, eq. (4.44) is the lower bound of eq. (4.6), and validates the treatment of the Bose-Hubbard model in terms of the Quantum-Phase model.

4.3.4 Effective Vortex Mass

The finite instanton-action acquired by a vortex moving from one site to another induces an effective mass m_{v} to these topological excitations. In this section we will give an analytic expression for the mass in terms of the original parameters of the Bose-Hubbard model. According to ref. [106], the instanton-action for a massive particle tunneling across a barrier $V(x)$ takes the form

$$S_{\text{inst}} = \int dx\, \sqrt{2mV(x)}. \tag{4.45}$$

By splitting the potential-barrier $V(x) = V_0 v(x)$ into a constant prefactor V_0 a dimensionless coordinate-dependent part $v(x) \sim \mathcal{O}(1)$, we can write the above equation like

$$S_{\text{inst}} = \sqrt{2mV_0} \int dx\, \sqrt{v(x)}. \tag{4.46}$$

The integral in eq. (4.46) is then but a numerical factor that depends implicitly on the shape of the barrier $v(x)$. Here, we are only interested in how the vortex mass depends on the microscopic Bose-Hubbard parameters, and will hence neglect any numerical factors on the order of one. Since we know the instanton-action from our previous discussion we can solve the eq. (4.46) for the mass m_v neglecting any numerical factors (in particular the numerical integral itself), which then yields the explicit expression

$$m_\mathrm{v} \approx \frac{S_\mathrm{inst}^2}{V_0}. \tag{4.47}$$

For a vortex, V_0 is the strength of the pinning due to the depletion of the superfluid. An analytic expression for the vortex-pinning-potential was calculated in ref. [96], and yields

$$V_0^\mathrm{vortex} \approx \frac{\hbar^2}{m_\mathrm{S}} \bar{n} Q(k\xi), \tag{4.48}$$

where m_S is the mass of the superfluid particles and $\xi = \sqrt{w/U\bar{n}}$ is the healing length. The function $Q(z)$ is defined via $Q(z) = \frac{J_1(2z)}{2z} + \int_1^\infty dx\, \frac{J_0(2xz)}{x}$, where $J_i(z)$ is the i-th Bessel-function of the first kind. By use of eq. (4.47) in combination with (4.48) and (4.41), we find that the vortex mass takes the analytic form

$$m_\mathrm{v} = \frac{m_\mathrm{S}}{Q(k\xi)} \frac{w}{U}. \tag{4.49}$$

In the relevant region of $k\xi \ll 1$ the function Q can be approximated by

$$Q(z) \approx -0.0772 - \log z. \tag{4.50}$$

This shows that Q depends but weakly on $k\xi$, and takes values on the order of one. We then find the final expression for the approximate vortex mass

$$m_\mathrm{v} = \frac{m_\mathrm{S}}{-\log(k\xi)} \frac{w}{U}. \tag{4.51}$$

Note that since $k\xi \ll 1$, $\log(k\xi) < 0$ and hence cancels the minus sign, so that $m_\mathrm{v} > 0$ for all parameters.

4.3.5 Validity of the Model

In the following, we want to discuss the limitations of our model with regard to the approximations made and thus provide an intuitive understanding of the validity of our approach. In addition, we compare our findings to previous works regarding that particular problem in order to provide a wider picture.

Our derivation of the vortex-model and the induced vortex-mass is based on the assumption that the system is in a regime where the lattice spacing is the dominating length scale. From a more physical point of view this means that the lattice always plays a significant role, and cannot be considered as a small perturbation to the otherwise continuous superfluid. This basically leaves us with two boundaries to obey: First, we require phase-coherence between the individual lattice sites in order to create a vortex excitation. The loss of phase-coherence and the associated transition into the Mott-insulating regime occurs at a critical interaction strength $U_\mathrm{c} = 8w\bar{n}$ and hence sets an upper boundary for the lattice depth. Second, the coherence-length ξ needs to be smaller than the lattice spacing in order to ensure that the vortex core does not extend over several lattice sites. A violation of this condition causes a (topological) transition into a Galilei-invariant regime [107], in which the healing-length is far larger than the lattice spacing. In turn, this gives rise to dissipative vortex motion as well as significant density-fluctuations and, as a result, leads to a frequency-dependence of the vortex-mass. The very same frequency-dependence was already found by Arovas and Freire [116] by starting from a Ginzburg-Landau Lagrangian. They obtained an explicit expression for the frequency-dependent vortex-mass, which exhibits both an infrared and ultraviolet divergence. The latter was found to be due to the vortex-core, and can be treated by introducing an ultraviolet temporal cutoff ξ/c_s. The finite frequency ω suppresses the infrared divergence and leads to the low-frequency approximation for the vortex-mass,

$$m_\mathrm{v} = m_\mathrm{s}\pi n_\mathrm{s}\xi^2 \left[\frac{1}{2\delta}\ln\frac{\delta+1}{\delta-1} + \operatorname{sign}\omega\,\frac{i\pi}{2\delta}\right], \tag{4.52}$$

with $\delta = \sqrt{1+\omega^2\xi^2/c_\mathrm{s}^2}$. Here, the factor $m_\mathrm{s}\pi n_\mathrm{s}\xi^2$ can be considered as the mass of the vortex core. It is important to stress that although this expression diverges logarithmically as $\omega \to 0$, its Fourier-transform is causal. Such logarithmic divergence has previously been found by Eckern and Schmid [117] in the context of vortices in granular films as well as Stamp et al. [118] for magnetic domain-walls.

Wang et al. [89] confirm these results and show that one can understand the vortex mass as a coupling-effect of the many-body vortex-excitation to the environmental modes. They derive an effective action for a single vortex in a superfluid by integrating out the fluctuations of the environmental modes, where they consider both phase- and density-fluctuations. Furthermore, they identify a regime in which a vortex moves dissipationless, and find a well-defined expression for the vortex-mass in the continuum, namely

$$m_{\mathrm{v}} = m_{\mathrm{s}} \pi n_{\mathrm{s}} \xi^2 \left[\frac{\pi^2}{32} + \frac{\ln R/\xi}{2} \right]. \tag{4.53}$$

The first term in the brackets accounts for phase fluctuations, whereas the second is due to density-fluctuations with the spatial cutoff R taking the value of the smaller of the system size and the distance between the vortices. The validity of their approach is based on the assumption that the vortex cyclotron-frequency ω_{c} is much smaller than the temporal cutoff c_{s}/ξ associated with the vortex core structure. Although hard to achieve in the continuum, they claim that this condition can be met within an optical lattice, in which the condition $\omega_{\mathrm{c}} \ll c_{\mathrm{s}}/\xi$ then translates to $\xi \ll 1$. Together with the condition $U < U_{\mathrm{c}}$ that ensures phase coherence between the different lattice sites they find but for notational differences

$$1 \gg \frac{w}{U\bar{n}} \gg \frac{1}{\bar{n}^2}. \tag{4.54}$$

However, this is exactly the condition (4.6) which marks the validity of the quantum phase model (see section 4.2.1 and ref. [107]). In that sense, this justifies our assumption of instantaneous vortex hopping, since any dissipative term would be due to finite hopping times. By a simple translation of the continuum vortex mass (4.53) they derive an equivalent expression for the lattice,

$$m_{\mathrm{v}} = m_{\mathrm{S}} \frac{\pi w}{U} \left[\frac{\pi^2}{32} + \frac{1}{4} \log \frac{U}{w\bar{n}} \right]. \tag{4.55}$$

Again, the first term in the brackets accounts for phase fluctuations, whereas the second is due to density-fluctuations. Comparing eq. (4.55) with our findings (4.51) we see that the two results agree in leading order, although our result does not show the logarithmic dependence on the coherence length. This is hardly surprising, since this term is due to density-fluctuations which we explicitly neglected in the approximation $\delta n \ll \bar{n}$. In turn, Wang et al. [89] do not find the weak dependence

$Q(\xi) \approx -\log \xi$ that originates from the effective vortex potential. The reason for that might be the very nature of how they translate their continuum results to the lattice, which is based on the correspondence $w \leftrightarrow \hbar^2/2m_{\mathrm{s}}$ and $U \leftrightarrow 4\pi a_{\mathrm{s}}\hbar^2/m_{\mathrm{s}}$, with a_{s} the scattering length.

4.3.6 Vortex-Hubbard Model

The previous results allow us to write an effective tight-binding Hamiltonian for vortices hopping between dual lattice sites

$$\begin{aligned} H_{\mathrm{VH}} = w_{\mathrm{v}} \sum_{\langle I,J\rangle} \left(v_I^\dagger v_J e^{i2\pi q_J \eta_{IJ}} + v_J^\dagger v_I e^{-i2\pi q_I \eta_{IJ}} \right) \\ + \pi K \sum_{I \neq J} (2\pi q_I)(2\pi q_J) \log |\mathbf{x}_I - \mathbf{x}_J| \, . \end{aligned} \tag{4.56}$$

Here, $v_I^\dagger$ (v_I) creates (annihilates) a vortex with vorticity q_I on the dual site I and $K = \bar{n}w$ is the superfluid stiffness. In turn, the vortex hopping rate is given by the vortex mass derived in eq. (4.51), i.e. $w_{\mathrm{v}} = \hbar^2/m_{\mathrm{v}}$. Eq. (4.56) is the generic model for two-dimensional charged particles on a lattice under the influence of both an external magnetic and electric field. The ratio between the hopping-rate and the interaction-strength is

$$\frac{w_{\mathrm{v}}}{K} = \frac{\hbar^2}{m_{\mathrm{v}} 2\bar{n}w} = \frac{\bar{n}\hbar^2}{m_{\mathrm{S}} U} \left[\frac{U}{w\bar{n}} \right]^2 , \tag{4.57}$$

and marks the balance between kinetic and interaction energy. Increasing the mobility of the superfluid particles decreases the mobility of the vortices and, as a result, drives them into the classical regime. Conversely, strong interactions in the superfluid leads to a quantum-mechanical behavior of the vortices. According to eq. (4.6), the term in brackets has to take values between $1/\bar{n}^2$ and 3 and, hence, the ratio (4.57) takes values

$$\frac{w_{\mathrm{v}}}{K} \in \frac{\hbar^2}{mU} \left[\frac{1}{\bar{n}^3}, \bar{n} \right] . \tag{4.58}$$

For large enough average superfluid filling $\bar{n}$, this gives rise to a huge regime in which the interaction energy can be tuned respective to the kinetic energy. Even so, one needs to keep in mind that the interaction is long-range and shows no screening effect, as for instance occurs in dipolar gases. In that sense, the interaction between vortices is always strong.

4.4 Vortex Dynamics

In section 4.3 we derived a fully quantum-mechanical model for vortices in an optical lattice. Our main result in section 4.3.3 was that vortices in an optical lattice become massive quantum-particles and hence should behave accordingly. The immediate question that arises is: What are the signatures for a quantum-motion of massive vortices as compared to their massless counterparts?

4.4.1 Classical Vortex Motion

It is instructive to begin with a semiclassical description of vortex motion in a continuous superfluid. Such a massless vortex is well described as a massless quasiparticle subject to two different kinds of forces: The interaction between the superfluid flow and the velocity-field of a vortex with vorticity q gives rise to the so-called Magnus force,

$$F_{\mathrm{M}} = -2\pi\hbar q n_{\mathrm{S}} \mathbf{v}_{\mathrm{S}} \wedge \hat{z}, \tag{4.59}$$

that is proportional to the local superfluid density n_{S} and the superfluid velocity $\mathbf{v}_{\mathrm{S}}$. On the other hand, a vortex moving around a closed loop of area A picks up a Berry-phase $\phi_{\mathrm{Berry}} = 2\pi\alpha A$, where α is a proportionality factor that depends on the particular microscopic Hamiltonian of the superfluid. This phase is in analogy to the Aharonov-Bohm-phase picked up by a charged particle in a magnetic field, and leads to the equivalent of the Lorentz-force, namely the Berry-force

$$F_{\mathrm{B}} = 2\pi\hbar q\alpha \mathbf{v}_{\mathrm{v}} \wedge \hat{z}. \tag{4.60}$$

Similar to the Magnus-force, the Berry-force acts perpendicular to the vortex velocity $\mathbf{v}_{\mathrm{v}}$. The dynamics of a vortex in a continuous superfluid is hence governed by the equation of motion

$$0 = F_{\mathrm{B}} + F_{\mathrm{M}} = 2\pi\hbar q(\alpha \mathbf{v}_{\mathrm{v}} - n_{\mathrm{S}} \mathbf{v}_{\mathrm{S}}) \wedge \hat{z}, \tag{4.61}$$

where the zero on the left-hand side stems from the lack of an inertial term for a classical vortex. If we assume the vortex and the superfluid to be stationary in a given reference-frame, both the Magnus- and the Berry-force vanish and, therefore, $v_\mathrm{v} = v_\mathrm{s} = 0$ is a solution to eq. (4.61). Galilei-invariance tells us that this is true for any reference frame moving at a constant velocity $\mathbf{v}_\mathrm{G}$. Yet the Galilei-transform of the stationary solution is only a solution itself if $\alpha = n_\mathrm{S}$, as can easily be seen by $0 = \alpha(-\mathbf{v}_\mathrm{G}) - n_\mathrm{s}(-\mathbf{v}_\mathrm{G}) = \alpha\mathbf{v}'_\mathrm{v} - n_\mathrm{s}\mathbf{v}'_\mathrm{S}$. Therefore, a classical vortex follows the superfluid velocity at its core position. On the other hand, if one explicitly breaks Galilei-invariance, this symmetry-argument no longer holds and the relation $\alpha = n_\mathrm{s}$ is allowed to change.

A different interpretation of the forces acting on a vortex can be given in terms of the Josephson-relation [114]. A moving vortex creates a time-dependent jump in the superfluid phase $\Delta\phi$ due to its non-trivial winding number q. The Josephson-relation $\Delta\mu = \hbar\partial_t\Delta\phi$ then relates such a jump to a change in the chemical potential $\Delta\mu$ perpendicular to the vortex velocity, and in turn leads to a superfluid flow. The resulting change in momentum of the superfluid particles is then transferred to the moving vortex, and, according to Newton, yields a force proportional to the relative velocity $\mathbf{v}_\mathrm{v} - \mathbf{v}_\mathrm{S}$.

Massive Vortices

Henceforth we consider the case in which the vortex turns massive. However, we do not specify the nature of this vortex mass, nor do we remove the Galilei-invariance of the system. Obviously, this is a rather naive approach, since the vortex mass derived in section 4.3.3 is rooted in the underlying lattice structure. On the other hand, it is instructive to consider the fundamental differences in the dynamics of

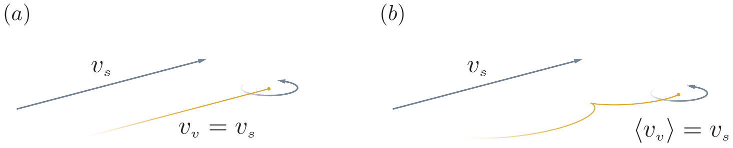

Figure 4.3: (a) Trajectory of a classical massless vortex. The balance between Magnus- and Berry-force in the Galilei-invariant system requires the vortex to follow the superfluid flow. Hence, we obtain $v_\mathrm{v} = v_\mathrm{s}$. ($b$) For a massive vortex in a Galilei-invariant system, the vortex-motion is no longer uniform, but exhibits oscillations. Still, on average a massive vortex follows the superfluid flow, $\langle v_\mathrm{v} \rangle = v_\mathrm{s}$.

a massive classical vortex as compared to its massless equivalent as well as its quantum counterpart. The addition of an inertial term to eq. (4.61) leaves us with the modified equations of motion

$$m_{\mathrm{v}} \partial_t \mathbf{v}_{\mathrm{v}} = F_{\mathrm{B}} + F_{\mathrm{M}} = 2\pi\hbar q \alpha (\mathbf{v}_{\mathrm{v}} - \mathbf{v}_{\mathrm{S}}) \wedge \hat{z}. \tag{4.62}$$

For a vortex in a superfluid with initial velocity $\mathbf{v}_{\mathrm{v}}^0$, the solution to eq. (4.62) reads

$$\mathbf{x}_{\mathrm{s}} = t\mathbf{v}_{\mathrm{s}} + \frac{\mathbf{v}_{\mathrm{v}}^0 - \mathbf{v}_{\mathrm{s}}}{\omega_{\mathrm{c}}} \left(\mathrm{id} \cos \omega_{\mathrm{c}} t - \varepsilon \sin \omega_{\mathrm{c}} t \right), \tag{4.63}$$

where $\omega_{\mathrm{c}} = 2\pi\hbar q n_{\mathrm{s}} / m_{\mathrm{v}}$ is the classical cyclotron frequency, $\mathbf{v}_{\mathrm{s}}$ is the superfluid velocity and ε is the totally antisymmetric tensor. Since the equation of motion is now of second order, the vortex no longer reacts instantaneously to a change of the superfluid flow. In addition, the wedge admixes parallel and orthogonal velocity components, and leads to a non-vanishing vortex velocity perpendicular to the superfluid flow. Rather than to accelerate in that direction, the vortex oscillates with an amplitude

$$a_{\mathrm{osc}} = \frac{m_{\mathrm{v}} v_{\mathrm{s}}}{2\pi\hbar q n_{\mathrm{s}}}. \tag{4.64}$$

Averaging over the oscillating term in eq. (4.63) still yields a vortex that follows the superfluid flow, regardless of the initial conditions. Hence, a mass-term in itself does not change in the fundamental dynamics of a vortex, but only adds an additional texture to its trajectory. Indeed, for a classical vortex in a weakly interacting superfluid, the oscillation amplitude is much smaller than the core-radius, $\xi \gg a_{\mathrm{osc}} = v_{\mathrm{s}} / \omega_{\mathrm{c}} \approx c_{\mathrm{s}} / \omega_{\mathrm{c}}$, and is thus obscured.

4.4.2 Vortex Motion on a Lattice

The introduction of a lattice explicitly breaks the Galilei-invariance and thus the balance between Magnus- and Berry-force. In order to derive the lattice-version of the continuum-relation $\alpha = n_{\mathrm{s}}$, we start from our vortex lattice model (4.56). For a single vortex the interaction term drops out, and we are left with a generic Hamiltonian of a gauged particle on a lattice,

$$H_{\mathrm{VH}} = -w_{\mathrm{v}} \sum_{\langle I,J \rangle} \left(v_I^\dagger v_J e^{i2\pi q_J \eta_{IJ}} + v_J^\dagger v_I e^{-i2\pi q_I \eta_{IJ}} \right). \tag{4.65}$$

Here, the gauge-field $2\pi\eta_{IJ}$ due to the superfluid filling $n_\mathrm{S} = \sum_\square \eta_{IJ}$ accounts for the non-vanishing commutation relation between the translational operators $\mathcal{T}_\mu$, namely

$$\mathcal{T}_x \mathcal{T}_y = \mathcal{T}_y \mathcal{T}_x e^{i2\pi n_\mathrm{S}}. \tag{4.66}$$

Formally, the addition of the phase factor is a transition from a linear representation of the translation group to a projective representation that is linear up to scalar factor. The Berry-phase of a vortex-state $|\psi_I\rangle$ moving around a lattice site with superfluid filling n_s takes the form

$$\phi_\mathrm{Berry} = 2\pi\alpha = \arg\langle\psi_I|\mathcal{T}_{-\hat{y}}\mathcal{T}_{-\hat{x}}\mathcal{T}_{\hat{y}}\mathcal{T}_{\hat{x}}|\psi_I\rangle = 2\pi n_\mathrm{s} \bmod 2\pi. \tag{4.67}$$

Yet, due to the 2π ambiguity of this expression the Berry phase is not uniquely defined and allows for a whole set of solutions $\alpha = n_\mathrm{S} + \mathbb{Z}$. A better understanding of the physics behind this ambiguity can be obtained by considering the change in momentum. Transporting a vortex along the y-direction yields a momentum-change $\Delta P_x = 2\pi n_\mathrm{S}\Delta y$. Since the motion takes place on a lattice, the momentum is only defined up to a reciprocal lattice vector. The simple 2π ambiguity has but severe consequences for the Hall-conductivity of the charged superfluid and, accordingly, for the Hall-conductivity of the vortices. Namely, the addition of the reciprocal lattice vector $2\pi\mathbb{Z}$ in principle allows for a change of sign in the Hall-conductivity for monotonously increasing superfluid filling n_s. As it turns out, this is indeed what happens. In a series of papers N. Lindner, A. Auerbach, D. Arovas and S. Huber [100,101,114,119] provided a comprehensive picture of the Hall-conductivity in lattice systems and found a topological transition from the alternating Hall-conductivity close to the Mott-insulator to the uniformly increasing classical expression in the Galilei-invariant Gross-Pitaevskii limit (see ref. [114] for further details).

Semiclassical Equations of Motion

As long as the Berry-phase ϕ_Berry remains small, the vortex only experiences a Lorentz-force leading to a cyclotron motion in the (lowest) energy-band. However, for large Berry-phase contributions $\alpha \bmod 1 \gg 0$ the effective magnetic field changes the Bloch-band itself. Indeed, for $n_\mathrm{s} = p/q \in \mathbb{Q}$ we are left with q magnetic subbands, the so-called magnetic Bloch-bands. This yields a fractional structure for the energy bands, which, due to its distinguished form, is called the Hofstadter butterfly [120]. The charged particle then only feels the excess magnetic field $\delta n = n_{\mathrm{s}} - \mathbb{Q}$, whereas n_{s} is included in the dispersion relation. In turn, the charged particle performs a cyclotron motion in the magnetic Bloch-band. Xiao et al. [121] derived semi-classical equations of motion for this particular system. In a two-dimensional lattice with orthogonal magnetic field the semiclassical equations are

$$\hbar\dot{\mathbf{k}} = \mathbf{F} - \dot{\mathbf{x}} \wedge \delta n_{\mathrm{s}} \hat{z}, \quad \hbar\dot{\mathbf{x}} = \frac{\partial E_M}{\partial \mathbf{k}} - \hbar\dot{\mathbf{k}} \wedge \hat{z}\Omega(\mathbf{k}). \tag{4.68}$$

Here, $E_M = E_{p/q}(k) - m(k)\delta n_{\mathrm{s}}$ is the magnetic Bloch band $E_{p/q}(k)$ with an additional Zeeman splitting $m(k)\delta n_{\mathrm{s}}$ due to the rotation of the wave-packet [121], whereas $\delta n_{\mathrm{s}} = n_{\mathrm{s}} - \mathbb{Q}$ is the excess magnetic field. Moreover, $\Omega(\mathbf{k})$ is the Berry-curvature

$$\boldsymbol{\Omega}(\mathbf{k}) = i\langle \nabla_{\mathbf{k}} u(\mathbf{k})| \wedge |\nabla_{\mathbf{k}} u(\mathbf{k})\rangle, \tag{4.69}$$

that acts as the momentum-space equivalent of a magnetic field. In a two-dimensional setup with orthogonal magnetic field, one can show that the Berry-curvature is perpendicular to the plane. Since the Berry-curvature explicitly depends on the vortex wave-function, we are not able to derive the equations of motion for general superfluid filling factors explicitly.

The Most Simple Interference Experiment

To circumvent the problem of calculating the Berry-curvature, we exploit the fact that the underlying vortex Hamiltonian (4.65) is periodic in the effective magnetic flux, that is the superfluid filling n_{s}. Accordingly, for integer superfluid filling $n_{\mathrm{s}} \in \mathbb{N}$ we find that (4.65) is invariant under time-reversal. The same has to be true for the corresponding equations of motion, which for $n_{\mathrm{s}} \in \mathbb{N}$ take the form

$$\hbar\dot{\mathbf{k}} = \mathbf{F}, \quad \hbar\dot{\mathbf{x}} = \frac{\partial E_M}{\partial \mathbf{k}} - \mathbf{F} \wedge \boldsymbol{\Omega}(\mathbf{k}). \tag{4.70}$$

Time-reversal of eq. (4.70) then gives rise to the condition $\Omega(-k) = -\Omega(k)$. Yet the spatial inversion symmetry of the underlying square lattice requires $\Omega(-k) = \Omega(k)$. To fulfill both these conditions, the Berry-curvature has to vanish identically throughout the Brillouin-zone. Therefore, the effective equations of motion at integer superfluid filling take the simple form

$$\hbar\dot{\mathbf{k}} = \mathbf{F}, \quad \hbar\dot{\mathbf{x}} = \frac{\partial E_0(\mathbf{k})}{\partial \mathbf{k}}, \tag{4.71}$$

where the magnetic Bloch-band reduces to the cosine-band suggested by the nearest-neighbor hopping in the Hamiltonian (4.65). The remaining quantum-property of these equations is the non-trivial dispersion relation $E_0(\mathbf{k}) = -2w_{\mathrm{v}}[\cos k_x + \cos k_y]$. Given the trivial solution of the first of the eqs. (4.71) under a constant force, namely $\hbar\mathbf{k} = \mathbf{F}t + \mathbf{k}_0$, the second equation reduces to

$$\dot{\mathbf{x}} = \left.\frac{\partial E_0(\mathbf{k})}{\partial \hbar\mathbf{k}}\right|_{\hbar\mathbf{k}=\mathbf{F}t+\mathbf{k}_0} = \frac{2w_{\mathrm{v}}}{\hbar}\left[\hat{x}\sin\frac{F_x t}{\hbar} + \hat{y}\sin\frac{F_y t}{\hbar}\right]. \tag{4.72}$$

Here, the periodic structure of the energy-band gives rise to Bloch-oscillations of the vortex velocity and in turn to the vortex position. The important point is that these oscillations are due to interference between the different eigenfunctions the wave-packet is composed of and hence are a hallmark for quantum properties of the vortex. In contrast to the oscillations of a classical massive vortex, the Bloch-oscillation amplitude is now parallel to the external force F. Moreover, the Hall-motion perpendicular to the external force vanishes completely due to the lack of an effective magnetic field.

The easiest way to apply a constant force on a vortex is to generate a constant superfluid current which, according to eq. (4.59), gives rise to a Magnus-force. A classical vortex would then just follow the superfluid flow, whereas the massive quantum vortex oscillates perpendicular to the superfluid current (see Fig. 4.4).

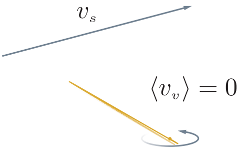

Figure 4.4: Trajectory of a quantum vortex on a lattice. For integer superfluid filling $\bar{n} \in \mathbb{N}$, which is equivalent to a vanishing effective magnetic field, the vortex experiences no Berry-force. However, the periodic dispersion-relation due to its induced mass leads to Bloch-oscillations of the vortex perpendicular to the superfluid flow v_{s}. Yet the vortex basically stays localized since $\langle v_{\mathrm{v}} \rangle = 0$.

The oscillation-amplitude and -frequency can be obtained directly from the equation of motion (4.72), and, by use of $w_\mathrm{v} = \hbar^2/m_\mathrm{v}$, take the respective form

$$a_\mathrm{BO} = \frac{\hbar^2}{m_\mathrm{v} 2\pi\hbar q \bar{n} v_\mathrm{s}} = \frac{-U\hbar \log \xi}{w m_\mathrm{s} 2\pi q \bar{n} v_\mathrm{s}}, \tag{4.73}$$

$$\omega_\mathrm{BO} = \frac{F}{\hbar} = 2\pi q \bar{n} v_\mathrm{s}. \tag{4.74}$$

Last, we want to give a rough estimate for the expected amplitude of such Bloch-oscillations. According to eq. (4.6), the factor of $U/w\bar{n}$ in a_BO takes values in $[1/\bar{n}^2, 3]$. That leaves us with $\hbar/m_\mathrm{s} v_\mathrm{s}$, which we expect to be much smaller than the recoil momentum $p_\mathrm{R} = 2\pi\hbar$. For $m_\mathrm{s} v_\mathrm{s} = p_\mathrm{s} \approx 0.01 p_\mathrm{R}$, $U/w\bar{n} \approx 0.1$ and all other factors on the order of one, we find that the oscillation-amplitude is roughly on the order of $a_\mathrm{BO} \approx 10$ and can easily be observed.

4.4.3 Experimental Realization

Our results can be directly verified in a system of cold atoms. The creation of superfluid vortices is achieved by the use of an optically synthesized magnetic field for ultra-cold neutral atoms [122], that in turn acts a chemical potential for the vortices. Alternatively, there is the possibility to directly transfer orbital angular momentum from a holographically generated light beam using a two-photon stimulated Raman process [123]. The fundamental difference in the vortex trajectory as described in the previous section can then be measured via interference with a second condensate, as is described in ref. [124]. Although an *in situ* technique [125] would be desirable, it suffers from a major advantage in this particular regime: Since the vortex core is much smaller than the lattice spacing in the strongly interacting regime, one has to ramp the parameters to the weakly interacting regime in order to make the vortex visible.

4.5 Conclusion

In this chapter, we have considered vortex-excitations in a cold atomic gas confined to an optical lattice. By use of a coherent-state path-integral approach we were able to map the superfluid degrees of freedom onto the vortex degrees of freedom, and thus derive an effective action for the vortices. The basis of this derivation has been the assumption that the lattice-spacing is the dominating length-scale, and that the system is in the strongly-interacting regime. Therefore, the vortex-core that is much smaller than the lattice-spacing and, as a result, the vortex is confined to a single lattice-plaquette. By neglecting fluctuations around the semiclassical path, we have derived an analytic expression for the instanton-action of a single vortex hopping from one plaquette to another. We have found that the imaginary part of the instanton-action is due to the interaction between the velocity-field of the vortex and the superfluid density, and yields the lattice-equivalent of the Magnus-force. Conversely, the real contribution stems from the vortex interacting with its own phonon-field. By integration over the latter we have obtained an explicit expression for the vortex hopping rate, and, accordingly, for the vortex mass. In turn, we have derived an effective tight-binding model for the vortex degrees of freedom with nearest-neighbor hopping as well as logarithmic interaction, as was found earlier in the context of vortex lattice melting. Last, we have provided a semiclassical equation of motion for the massive quantum vortices, and have compared those to the hydrodynamic equation of motion of a classical vortex. Rather than to follow a superfluid flow, quantum lattice vortices can exhibit Bloch-oscillations perpendicular to it, and thus provide clear evidence for quantum-interference.

4.A Continuum Limit of the Vortex Action

In this section we derive the continuum version of the action (4.14) and establish its connection to the electrodynamic field theory in analogy to ref. [116]. Our starting point is the action

$$\begin{aligned} S_{\mathrm{rQPM}}^{\theta\psi} = \int_0^{\hbar\beta} d\tau \, \frac{U}{2} \left[\sum_I \left(\sum_\square \psi_{JI} \right)^2 + \sum_{\langle I,J \rangle} \left(\theta_{IJ} - \partial_{c_{\mathrm{s}}\tau} \psi_{JI} \right)^2 \right] \\ - 2\pi i \sum_I \theta_I c_{\mathrm{s}} \left(q_I - \bar{B} \right) - 2\pi i \hbar \sum_{\langle I,J \rangle} \left(\psi_{JI} - \eta_{JI} \right) j_{JI}. \end{aligned} \tag{4.75}$$

The first term in eq. (4.75), namely the *magnetic* term $\sum_\square \psi_{JI}$, reduces to

$$\begin{aligned} \sum_\square \psi_{JI} &= -(\psi_{(I,I+\hat{x})+\hat{y}} - \psi_{I,I+\hat{x}}) + (\psi_{(I,I+\hat{y})+\hat{x}} - \psi_{I,I+\hat{y}}) \\ &\approx \partial_x \psi^{\hat{y}} - \partial_y \psi^{\hat{x}} = \nabla \wedge \psi(\mathbf{x}). \end{aligned} \tag{4.76}$$

Note that this is indeed in analogy to the magnetic field in common electrodynamics, and thus justifies our notation. Likewise, the second, *electric* term $\theta_{IJ} - \partial_{c_{\mathrm{s}}\tau} \psi_{JI}$

in eq. (4.75) takes the form

$$\theta_{IJ} - \partial_{c_s\tau}\psi_{JI} \approx \nabla\theta(\mathbf{x}) - \partial_{c_s\tau}\psi(\mathbf{x}). \tag{4.77}$$

The full action (4.75) in the continuum-limit then reads

$$S^{\text{cont}}_{\text{rQPM}} = \int_0^{\hbar\beta} d\tau d^2x \, \frac{U}{2}\left[(\nabla\wedge\psi(\mathbf{x}))^2 + (\nabla\theta(\mathbf{x}) - \partial_{c_s\tau}\psi(\mathbf{x}))^2 \right] - 2\pi i\hbar\theta(\mathbf{x})(c(\mathbf{x}) - \bar{B}(\mathbf{x})) - 2\pi i\hbar(\psi(\mathbf{x}) - \eta)j(\mathbf{x}). \tag{4.78}$$

Here, the term in the square brackets is the well-known Lagrangian of a free electromagnetic field, that is $\mathcal{L}_{\text{EM}} = 1/4\,(e^2 + c_s^2 b^2)$. The disturbing plus-sign arises due to the imaginary time, and can easily be seen in Weyl-gauge, where the electric field is but a time-derivative of the vector-potential. As in the lattice-calculation above, we can introduce the covariant notation by using the (2+1)-vector χ. In this notion, the continuum vortex action takes the compact form

$$S^{\text{cont}}_{\text{rQPM}} = \int_0^{\hbar\beta} d\tau d^2x \, \frac{U}{2}\chi(\mathbf{x})\Delta\chi(\mathbf{x}) - 2\pi i\hbar(\chi(\mathbf{x}) - \eta)j(\mathbf{x}), \tag{4.79}$$

where the coupling-matrix Δ is given by

$$\Delta = \begin{pmatrix} -\partial_x^2 - \partial_y^2 & \partial_x\partial_{c_s\tau} & \partial_y\partial_{c_s\tau} \\ \partial_x\partial_{c_s\tau} & -\partial_{c_s\tau}^2 - \partial_y^2 & \partial_x\partial_y \\ \partial_y\partial_{c_s\tau} & \partial_x\partial_y & -\partial_{c_s\tau}^2 - \partial_x^2 \end{pmatrix}. \tag{4.80}$$

This very expression was already found by Arovas and Freire [116]. They started from the standard Ginzburg-Landau Lagrangian density in the presence of an external gauge field, and derived eq. (4.79) via a Hubbard-Stratonovich transformation. In order to derive an effective theory for the vortices we integrate over the phonon degrees of freedom, and are left with the effective vortex action

$$S^{\text{cont}}_{\text{rQPM}} = -\frac{(2\pi\hbar)^2}{2U}\int d\tau d^2x \, d\tau' d^2x' \, j(\mathbf{x},\tau)\Delta^{-1}(\mathbf{x}-\mathbf{x}',\tau-\tau')j(\mathbf{x}',\tau') + 2\pi i\hbar\int d\tau d^2x \, \eta(\mathbf{x})j(\mathbf{x},\tau). \tag{4.81}$$

As is expected from the analogy to electrodynamics, or, more specifically, $U(1)$ gauge theory, the coupling-matrix Δ is singular, and has to be regularized in order to obtain the explicit expression for the vortex Green's-function. By choosing the Lorentz-gauge, namely $\partial\chi = 0$, the non-zero part of Δ takes the simple form $\Delta = -\mathrm{id}\,\partial^2$, which, in turn, can be easily inverted. We are thus left with the trivial propagator for the phonon field,

$$\Delta^{-1} = -\mathrm{id}\,\frac{1}{\partial^2} = -\mathrm{id}\,\frac{1}{\partial^2_{c_\mathrm{s}\tau} + \partial^2_x + \partial^2_y}. \tag{4.82}$$

In the static limit, the Green's-function Δ^{-1} gives rise to a logarithmic interaction between the vortices in agreement with the classical hydrodynamic theory. Taking retardation effects into account one finds a frequency-dependent mass term which diverges in both the UV and IR limit (see subsection 4.3.5 and ref. [116]).

4.B Lattice Green's-Function

It is convenient to calculate the Green's-function on the lattice in Fourier-space, in which the phonon-fields θ_I and ψ_{JI} take the respective form

$$\theta_I = \int d\omega\, e^{i\omega\tau} \sum_{\mathbf{k}} e^{i\mathbf{k}\mathbf{x}_I} \theta_{\mathbf{k},\omega} \tag{4.83}$$

and

$$\psi_{JI} = \int d\omega\, e^{i\omega\tau} \sum_{\mathbf{k}} e^{i\mathbf{k}\frac{\mathbf{x}_J+\mathbf{x}_I}{2}} \psi^{JI}_{\mathbf{k},\omega}. \tag{4.84}$$

For the sake of convenience, we split the free action for the phonons into the *electric* term $(\theta_{IJ} - \partial\psi_{JI})^2$ and the *magnetic* term $(\sum_{\square} \psi_{JI})^2$. The Fourier-transform of the electric term then reads

$$\begin{aligned}
&\int d\tau \sum_{\langle I,J\rangle} (\theta_{IJ} - \partial\psi_{JI})^2 \\
&= \sum_I \sum_{\llcorner} \sum_{\mathbf{k},\mathbf{k}'} \int d\omega \Bigg[\theta_{\mathbf{k},\omega}\theta_{\mathbf{k}',-\omega} \left(e^{i\mathbf{k}\mathbf{x}_I} - e^{i\mathbf{k}\mathbf{x}_J}\right) \left(e^{i\mathbf{k}'\mathbf{x}_I} - e^{i\mathbf{k}'\mathbf{x}_J}\right) \\
&\qquad + \theta_{\mathbf{k},\omega} i \frac{\omega}{c_\mathrm{s}} \psi^{JI}_{\mathbf{k}',-\omega} \left(e^{i\mathbf{k}\mathbf{x}_I} - e^{i\mathbf{k}\mathbf{x}_J}\right) e^{i\mathbf{k}'\frac{\mathbf{x}_J+\mathbf{x}_I}{2}} + \frac{\omega^2}{c_\mathrm{s}^2} \psi^{JI}_{\mathbf{k},\omega} \psi^{JI}_{\mathbf{k}',-\omega} e^{i(\mathbf{k}+\mathbf{k}')\frac{\mathbf{x}_J+\mathbf{x}_I}{2}} \Bigg],
\end{aligned}$$

where the summation $\sum_{\text{L}}$ denotes the two links in the positive direction situated at the dual lattice site I. For the sake of brevity we henceforth only consider a link in the $\hat{x}$-direction, so that $I = J + \hat{x}$. A link in the $\hat{y}$-direction yields an analog result, however with $\hat{x}$ and $\hat{y}$ interchanged. Moreover, we will split the above summation into its three components, in the vain hope to achieve something resembling a clear calculation.

(i) First term:

$$\begin{aligned}\sum_{J}\sum_{\mathbf{k},\mathbf{k}'}\theta_{\mathbf{k},\omega}\theta_{\mathbf{k}',-\omega}\left(e^{i\mathbf{k}(\mathbf{x}_J+\hat{x})}-e^{i\mathbf{k}\mathbf{x}_J}\right)\left(e^{i\mathbf{k}'(\mathbf{x}_J+\hat{x})}-e^{i\mathbf{k}'\mathbf{x}_J}\right)\\ =\sum_{\mathbf{k}}|\theta_{\mathbf{k},\omega}|^2 4\sin^2\frac{k_x}{2},\end{aligned}$$

with the short-hand notation $|\theta_{\mathbf{k},\omega}|^2 = \theta_{\mathbf{k},\omega}\theta_{-\mathbf{k},-\omega}$.

(ii) Second term:

$$\begin{aligned}\sum_{J}\sum_{\mathbf{k},\mathbf{k}'}\theta_{\mathbf{k},\omega}i\frac{\omega}{c_{\text{s}}}\psi^{JI}_{\mathbf{k}',-\omega}\left(e^{i\mathbf{k}(\mathbf{x}_J+\hat{x})}-e^{i\mathbf{k}\mathbf{x}_J}\right)e^{i\mathbf{k}'\frac{\mathbf{x}_J+\mathbf{x}_{J+\hat{x}}}{2}}\\ =-\sum_{\mathbf{k}}\theta_{\mathbf{k},\omega}\psi^{JI}_{-\mathbf{k},-\omega}2\frac{\omega}{c_{\text{s}}}\sin\frac{k_x}{2},\end{aligned}$$

and, of course, the conjugate counterpart.

(iii) Third term:

$$\sum_{J}\sum_{\mathbf{k},\mathbf{k}'}\frac{\omega^2}{c_{\text{s}}^2}\psi^{JI}_{\mathbf{k},\omega}\psi^{JI}_{\mathbf{k}',-\omega}e^{i(\mathbf{k}+\mathbf{k}')\frac{\mathbf{x}_J+\mathbf{x}_{J+\hat{x}}}{2}}=\sum_{\mathbf{k}}\frac{\omega^2}{c_{\text{s}}^2}|\psi^{JI}_{\mathbf{k},\omega}|^2.$$

The overall result may then be written in the *compact* form

$$\begin{aligned}&\int d\tau\sum_{\langle I,J\rangle}\left(\theta_{IJ}-\partial\psi_{JI}\right)^2\\ &=\int d\omega\sum_{\mathbf{k}}\begin{pmatrix}\theta_{-\mathbf{k},-\omega}\\ \psi^{JI}_{-\mathbf{k},-\omega}\end{pmatrix}\begin{pmatrix}4\sin^2\frac{k_x}{2} & -2\frac{\omega}{c_{\text{s}}}\sin\frac{k_x}{2}\\ -2\frac{\omega}{c_{\text{s}}}\sin\frac{k_x}{2} & \frac{\omega^2}{c_{\text{s}}^2}\end{pmatrix}\begin{pmatrix}\theta_{\mathbf{k},\omega}\\ \psi^{JI}_{\mathbf{k},\omega}\end{pmatrix},\end{aligned}$$

together with the equivalent expression in which x and y are interchanged.

In Fourier-space, the lattice version of the curl reads

$$\begin{aligned}\sum_{\square}\psi_{JI} &= \psi_{I,I+\hat{x}}+\psi_{I+\hat{x},I+\hat{x}+\hat{y}}-\psi_{I+\hat{y},I+\hat{x}+\hat{y}}-\psi_{I,I+\hat{y}}\\ &=\sum_{\mathbf{k}} e^{i\frac{k_x+k_y}{2}}2i\Big[-\psi^{\hat{x}}_{\mathbf{k},\omega}\sin\frac{k_y}{2}+\psi^{\hat{y}}_{\mathbf{k},\omega}\sin\frac{k_x}{2}\Big]e^{i\mathbf{k}\mathbf{x}_I}.\end{aligned}$$

Omitting the factor of $(2i)^2=-4$, the magnetic term reduces to

$$\begin{aligned}&\sum_I\sum_{\mathbf{k},\mathbf{k}'} e^{i(\mathbf{k}+\mathbf{k}')\mathbf{x}_I}e^{i\frac{k_x+k_y}{2}}e^{i\frac{k'_x+k'_y}{2}}\Big[-\psi^{\hat{x}}_{\mathbf{k},\omega}\sin\frac{k_y}{2}+\psi^{\hat{y}}_{\mathbf{k},\omega}\sin\frac{k_x}{2}\Big]\\ &\qquad\times\Big[-\psi^{\hat{x}}_{\mathbf{k}',-\omega}\sin\frac{k'_y}{2}+\psi^{\hat{y}}_{\mathbf{k}',-\omega}\sin\frac{k'_x}{2}\Big]\\ &=\sum_{\mathbf{k}}\Big[\psi^{\hat{x}}_{\mathbf{k},\omega}\psi^{\hat{x}}_{-\mathbf{k},-\omega}\sin^2\frac{k_y}{2}-\psi^{\hat{x}}_{\mathbf{k},\omega}\psi^{\hat{y}}_{-\mathbf{k},-\omega}\sin\frac{k_x}{2}\sin\frac{k_y}{2}\\ &\qquad-\psi^{\hat{y}}_{\mathbf{k},\omega}\psi^{\hat{x}}_{-\mathbf{k},-\omega}\sin\frac{k_x}{2}\sin\frac{k_y}{2}+\psi^{\hat{y}}_{\mathbf{k},\omega}\psi^{\hat{y}}_{-\mathbf{k},-\omega}\sin^2\frac{k_x}{2}\Big].\end{aligned}$$

Thus, we are left with the identity

$$\begin{aligned}&\int d\tau\sum_I\Big(\sum_{\square}\psi_{JI}\Big)^2\\ &=4\int d\omega\sum_{\mathbf{k}}\begin{pmatrix}\psi^{\hat{x}}_{-\mathbf{k},-\omega}\\ \psi^{\hat{y}}_{-\mathbf{k},-\omega}\end{pmatrix}\begin{pmatrix}\sin^2\frac{k_y}{2} & -\sin\frac{k_x}{2}\sin\frac{k_y}{2}\\ -\sin\frac{k_x}{2}\sin\frac{k_y}{2} & \sin^2\frac{k_x}{2}\end{pmatrix}\begin{pmatrix}\psi^{\hat{x}}_{\mathbf{k},\omega}\\ \psi^{\hat{y}}_{\mathbf{k},\omega}\end{pmatrix}.\end{aligned}$$

Cast in terms of the (2+1)-vector notation $\chi_{\mathbf{k},\omega}=(\theta_{\mathbf{k},\omega},\psi^{\hat{x}}_{\mathbf{k},\omega},\psi^{\hat{y}}_{\mathbf{k},\omega})$, we find the Fourier-transform of the interaction-matrix for the phonon field as

$$\Delta_{IJ}=\int d\omega\, e^{i\omega\tau}\int\frac{d^2k}{(2\pi)^2}e^{i\mathbf{k}(\mathbf{x}_I-\mathbf{x}_J)}\Delta_{\mathbf{k},\omega},\tag{4.85}$$

with

$$\Delta_{\mathbf{k},\omega}=\begin{pmatrix}4\sin^2\frac{k_x}{2}+4\sin^2\frac{k_y}{2} & -2\frac{\omega}{c_\mathrm{s}}\sin\frac{k_x}{2} & -2\frac{\omega}{c_\mathrm{s}}\sin\frac{k_y}{2}\\ -2\frac{\omega}{c_\mathrm{s}}\sin\frac{k_x}{2} & \frac{\omega^2}{c_\mathrm{s}^2}+4\sin^2\frac{k_y}{2} & -4\sin\frac{k_x}{2}\sin\frac{k_y}{2}\\ -2\frac{\omega}{c_\mathrm{s}}\sin\frac{k_y}{2} & -4\sin\frac{k_x}{2}\sin\frac{k_y}{2} & \frac{\omega^2}{c_\mathrm{s}^2}+4\sin^2\frac{k_x}{2}\end{pmatrix}.\tag{4.86}$$

However, the interaction-matrix (4.86) is singular and, therefore, needs to be regularized in order to derive a well-defined inverse. This may be achieved by adding a convenient zero in the form of $0 = \Omega_{\mathbf{k},\omega}\chi_{\mathbf{k},\omega}$ with

$$\Omega_{\mathbf{k},\omega} = \begin{pmatrix} \omega/c_{\mathrm{s}} \\ 2\sin\frac{k_x}{2} \\ 2\sin\frac{k_y}{2} \end{pmatrix} \otimes \begin{pmatrix} \omega/c_{\mathrm{s}} \\ 2\sin\frac{k_x}{2} \\ 2\sin\frac{k_y}{2} \end{pmatrix}. \tag{4.87}$$

The Euler-Lagrange equations of the action (4.14) imply that $\Omega_{\mathbf{k},\omega}\chi_{\mathbf{k},\omega} = 0$ is indeed fulfilled. In the language of electromagnetism, this is just the discrete Lorentz-gauge condition. In turn, the regularized interaction-matrix $\Delta^{\mathrm{reg}}_{\mathbf{k},\omega} = \Delta_{\mathbf{k},\omega} + \Omega_{\mathbf{k},\omega}$ is purely diagonal, and takes the form already presented in eq. (4.19).

Chapter 5

Fractional Excitations in Cold Atomic Gases

5.1 Motivation

Excitations carrying fractional quantum numbers are one of the most intriguing features of strongly interacting many-body systems. Arguably the most celebrated of those is the charge $e/3$ Laughlin quasiparticle responsible for the fractional quantum hall effect, where a single electronic charge attaches to three magnetic flux-quanta [126]. Much effort is devoted into finding novel phases with even more exotic excitations such as non-abelian anyons and fractional statistics in three-dimensional systems. Yet, those excitations are notoriously hard to study in solid-state systems, as their very nature is based on interactions rather than single-particle properties. In the quest for the experimental realization of such strongly-correlated phases, cold atomic gases with their clean and controllable environment are a promising candidate and testing-ground [16].

A variety of theoretical proposals in cold atomic gases focus on the realization of strongly-correlated phases with fractional excitations. Among the most prominent examples are systems which support spin-liquid phases [127], as well as Kitaev's famous toric-code with abelian anyonic excitations [128–131], and systems in large effective magnetic fields [103, 105] which exhibit fractional quantum hall states [104, 132–137]. These proposals are based on standard experimental tools presently available in the context of quantum-simulation, and are reviewed in the comprehensive work of Bloch, Dalibard and Nascimbéne [138]. The latest development of experiments [27, 139] with single-site readout and addressability in optical lattices has opened the path for the observation of a novel quantum phase transition in tilted optical lattices [2, 140–142], and marks a first step in this direction of simulating fractional excitations within cold atomic gases.

A tilted optical lattice exhibits a transition from a phase with one atom on each lattice-site into a density-wave phase with broken translational symmetry, in which fundamental excitations are domain-walls carrying an effective fractional charge. Yet, the simplest experimentally accessible excitation is achieved by moving a single atom from a doubly-occupied site to its neighboring site and corresponds to the creation of two closely bound domain-walls. This is in direct analogy to the one-dimensional Ising-model in the antiferromagnetic phase; there, the fundamental excitations take the form of two adjacent spins pointing upwards. The important question is then, whether these experimentally accessible excitations will decay into the fundamental domain-wall excitations and how to detect these fractional excitations. In this chapter, we answer this question thoroughly, and provide both a theory for the dynamics of fractional excitations as well as a scheme for their experimental observation. In addition, we confirm our theoretical analysis by t-DMRG simulations, which were created in collaboration with Jad Halimeh, Ian McCulloch and Ulrich Schollwöck in Munich.

5.2 Tilted Bose-Hubbard Model

We start with the one-dimensional tilted Bose-Hubbard model studied both theoretically [140, 142] and experimentally [2, 15]. With the on-site interaction U, the hopping-rate w, and the lattice-tilt E per site, the microscopic Hamiltonian takes the form

$$H_{\mathrm{TBH}} = -\, w \sum_j \left(a_j^\dagger a_{j+1} + a_j a_{j+1}^\dagger \right) + \frac{U}{2} \sum_j n_j (n_j - 1) - E \sum_j j n_j . \qquad (5.1)$$

Here, $a_j^\dagger$ (a_j) is the bosonic creation (annihilation) operator for a particle on site j, $n_j = a_j^\dagger a_j$ the number operator.

In the following, we focus on the regime with an average density of one atom per lattice-site and a large on-site interaction U compared to the hopping-rate w. We further assume a positive tilt $E > 0$, that is the lattice is tilted to the right. The relevant energies are then the energy difference $\Delta = E - U$ and the hopping-rate w. For large negative Δ, the Mott-insulator state is stable. However, increasing

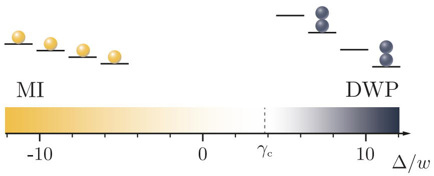

Figure 5.1: Phase diagram for the tilted Bose-Hubbard model in the regime $\Delta, w \ll U, E > 0$ and an averaged density of one particle per lattice-site: Mott-insulator (MI) ground-state for $\Delta/w < \gamma_c \approx 1.85$ [140], and the density-wave phase (DWP) for $\Delta/w > \gamma_c$.

$\Delta \approx w$ allows for particles to tunnel to their right neighboring site as long as the particle on that respective site has not tunneled itself. An adiabatic increase of the lattice-tilt E from zero to $E \gg U$ then yields a transition from the Mott-insulating phase to a density-wave phase with broken translational symmetry in which two atoms occupy each second lattice-site. Note that this is not the ground-state but rather a metastable state, in which energy conservation prevents relaxation.

These constraints are most conveniently incorporated by a mapping of the Bose-Hubbard model to a spin-model: The spin-degree of freedom resides between two lattice-sites i and $i+1$. If an atom has tunneled from site i to site $i+1$, the respective spin points down. In turn, if the atom is still on its original site i, the spin points up. Then, the Bose-Hubbard model maps to the one-dimensional Ising-model

$$H_{\text{Ising}} = -2\sqrt{2}w \sum_i S_x^i + \Delta \sum_i S_z^i + J \sum_i \left(S_z^i - \frac{1}{2}\right)\left(S_z^{i+1} - \frac{1}{2}\right), \tag{5.2}$$

where S_z^i (S_x^i) is the spin operator along the z (x) axis. Moreover, the last term accounts for the conditional tunneling constraint and formaly requires to take the limit $J \to \infty$. In the Ising-picture, the Mott-insulating state corresponds to a paramagnetic phase with all spin-up, whereas the ordered broken-symmetry phase corresponds to a Ising antiferromagnetic ground-state.

5.3 Effective Model for Fractional Excitations

The fundamental excitations in the density-wave phase with $E, U \gg \Delta \gg w$ take the form of domain-walls separating the two degenerate density-wave realizations, and are marked by a singly occupied site. However, the experimentally accessible low-energy excitations are achieved by moving a particle from a doubly occupied lattice-site to its neighboring site on the left (see Fig. 5.4). The energy cost of such a single-particle excitation is the energy due to the lattice-tilt E minus the on-site interaction U, that is Δ, and is exactly double the energy of a single domain-wall. In that sense, domain-walls are excitations carrying a fraction, namely half, the energy of a single-particle excitation. A single-particle excitation can thus be considered as two domain-walls sitting on adjacent lattice sites. The fractional character shows directly in the analog Ising picture: There, a single-particle excitation in the density-wave phase corresponds to a single spin-flip in the antiferromagnetic configuration, thus creating three adjacent spins pointing upwards. Conversely, a domain-wall is a configuration where only two adjacent spins point upwards, and separates the two degenerate antiferromagnetic phases.

5.3.1 Second-Order Processes

Quantum-fluctuations allow a domain-wall to hop from one lattice site to the other. Due to the broken translational symmetry of the density-wave phase, an individual hopping process takes place from site i to site $i \pm 2$. Therefore, domain-walls are restricted to even or odd lattice-sites each, depending on the local order. In principle, such hopping allows for the decay of a single-particle excitation into two spatially separated domain-walls, and hence creates a phase of opposing order between the latter. In second-order perturbation in w/Δ, only a single process contributes to the domain-wall hopping (see Fig. 5.3): For a domain-wall hopping to the right, a particle from the doubly occupied site to the right of the single particle associated with the domain-wall first moves to the left. Then, the initial single particle moves one site to the right, and thus creates a double occupancy on the previously empty site. The single occupancy is now directly to the right of this particular site. The energy difference between the intermediate state and the initial one in this process is Δ. In contrast, reversing the order of this process would yield an intermediate state with energy difference $-E$. Since we assumed $E \ll \Delta$, the latter is strongly suppressed. The resulting expression for the second-order hopping rate then takes the form

$$z = 2w^2/\Delta. \tag{5.3}$$

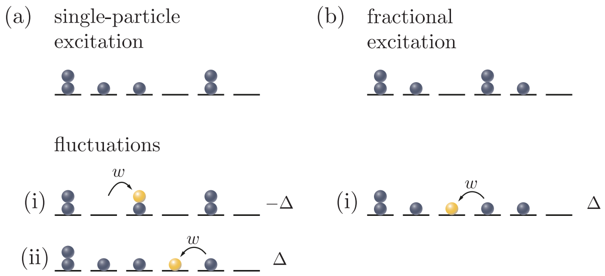

Figure 5.2: Leading order fluctuation processes contributing to the nearest-neighbor interaction: (a) Fluctuations of the single-particle excitation: A particle from the second site can hop to the third and back again (i). Likewise, a particle from the fifth site can hop to the fourth (ii). Those two intermediate states have an opposing energy difference with respect to the initial configuration, and thus the energy contribution vanishes. However, in an initial state of two fractional excitations (b) a particle can hop from the fourth to the third site (i). In turn, the energy of this configuration is lowered by $2w^2/\Delta$, where the factor of 2 is due to Bosonic enhancement. Processes on the order of $1/E$ and $1/U$ are not shown in this diagram.

An explicit calculation for this particular expression is found in appendix 5.A. On the other hand, adding quantum-fluctuations lifts the classical ($w = 0$) degeneracy between the single-particle excitation and two spatially separated domain-walls. By applying the same second-order perturbation-theory as above we find the energy-shift

$$V = 2w^2/\Delta, \tag{5.4}$$

which represents a repulsive short-range interaction between the domain-walls. Note that this interaction energy V takes the same value as the hopping rate z. In consequence, the effective theory derived below will feature but a single energy scale. The question is weather this interaction gives rise to a stable bound state of domain-walls.

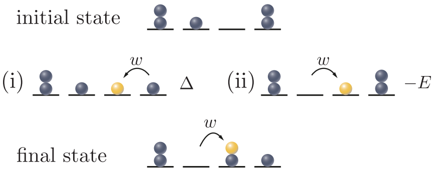

Figure 5.3: Intermediate states for a fractional excitation hopping from the second to the fourth site: In second-order, one of the two particle from the fourth can first hop to the third site, and then the particle from the second can hop to the third site (i). The reversed order process however, in which the particle from the second site hops to the third site first (ii) is strongly suppressed due to the large energy difference E of the intermediate state.

5.3.2 Hard-Core Boson Model

The conditional tunneling restriction of fractional excitations in the microscopic lattice can be uniquely fulfilled by introducing a new lattice: Each singly occupied site and the combination of a doubly occupied site next to an empty site count as a new lattice-site (see Fig. 5.4). In consequence, the number of effective lattice-sites between two excitations is half the number of microscopic lattice-sites. The dynamics of fractional excitations is then governed by the hard-core boson model with nearest-neighbor hopping z and interaction V,

$$H_{\mathrm{HCB}} = -z \sum_{i} \left(b_j^\dagger b_{j+1} + b_j b_{j+1}^\dagger \right) + V \sum_{j} n_j n_{j+1}, \tag{5.5}$$

where $b_j^\dagger$ (b_j) is the creation (annihilation) operator for a fractional excitation on site j, and $n_j = b_j^\dagger b_j \in [0, 1]$ the number operator. Similar Hamiltonians have been studied previously in the context of repulsively-bound states [143, 144]. There, a bound-state of fractional excitations means that the experimental accessible single-particle excitation cannot decay into its two fractional constituents due to energy conservation. Likewise, the absence of a bound state corresponds to a situation in which the single-particle excitation decays into delocalized fractional excitations, and thus can be observed individually in an experiment. Up to second-order perturbation, the hard-core Boson model has the single energy scale $z = V$, which yields an universal bound-state structure for the fractional excitations.

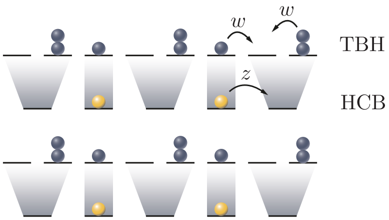

Figure 5.4: Mapping from the tilted Bose Hubbard model (TBH) onto the effective hard-core boson model (HCB): Two neighboring lattice-sites occupied by a $0, 2$-configuration map onto a single unoccupied site, whereas a singly occupied site maps onto an occupied site. A second-order transition with $z = 2w^2/\Delta$ allows for an effective hopping of the fractional excitations.

5.3.3 Eigenstates of the Hard-Core Boson Hamiltonian

In order to derive the two-particle eigenfunctions of the effective Hamiltonian (5.5), we write the wave-function for two fractional excitations in the effective model as $\psi(i, j)$, where i and j denote the positions of the fractional excitations in the effective lattice. The discrete translational invariance of the system provides conservation of the center-of-mass quasi-momentum Q, which allows for an expansion into eigenfunctions of H_{HCB} for a fixed center-of-mass quasi-momentum. Therefore, the two-particle wave-function can be factorized as $\psi(X, x) = e^{-iQX}\psi(x)$ with the center-of-mass $X = (i + j)/2$ and relative coordinates, $x = i - j$ (see appendix 5.C.1). In particular, we choose the normalization such that x is restricted to non-negative values.

We find two different regimes for the two-particle states: In the first regime with $|Q| \leq Q_{\text{c}} = 2\pi/3$, the two-particle eigenfunctions are given by scattering states ψ_q alone with energy $E_q = -z_Q \cos q$, where q is the relative momentum and $z_Q = 2z \cos Q/2$ denotes the hopping-rate in the center-of-mass frame. Its wave-function reduces to plane waves, $\psi_q(x) = (1 - \delta_{x,0}) \cos(q|x| + \phi_{Q,q})$, with a scattering-phase shift

$$\phi_{Q,q} = \arctan \frac{\cos q + 2 \cos Q/2}{\sin q}.$$

The Kronecker-delta factor $1 - \delta_{x,0}$ then accounts for the hard-core constraint and enforces $\psi_q = 0$ at $x = 0$. In the second regime for $|Q| > Q_{\text{c}}$, an additional bound state ψ_B emerges. The repulsive interaction yields a bound-state energy $E_\mathrm{B} = z(1 - 4\cos^2 Q/2)$ lying above the scattering continuum (see Fig. 5.5). Its two-particle wave-function shows an exponential decay with relative distance x, and can be written as

$$\psi_\mathrm{B}(x) = (1 - \delta_{x,0}) \left[\frac{1 - 4\cos^2 Q/2}{4\cos^2 Q/2}\right]^{\frac{1}{2}} \left(-2\cos\frac{Q}{2}\right)^{|x|}. \tag{5.6}$$

Note that the alternating amplitude of the wave-function is a typical feature of a repulsively-bound state. The general wave-function of two fractional excitations with fixed center-of-mass momentum Q can therefore be decomposed as

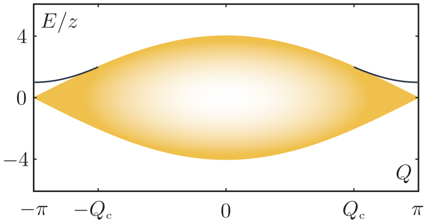

Figure 5.5: Center-of-mass energy diagram for the scattering states and the bound state of the effective hard-core boson model. The scattering continuum is indicated by the *fish-eye* (yellow). Above a critical momentum $Q_\mathrm{c} = 2\pi/3$, a stable repulsively bound state emerges (blue line).

$$\psi(X, x) = e^{-iQX}\left[C_\mathrm{B}\psi_\mathrm{B}e^{-iE_\mathrm{B}t/\hbar} + \int \frac{dq}{2\pi}\, C_q\psi_q e^{-iE_q t/\hbar}\right], \tag{5.7}$$

with C_B and C_q denoting the overlap of the initial wave-function with the bound and scattering eigenfunctions of H_HCB.

5.4 Time-Evolution of a Single-Particle Excitation

In the following we use an initial state of delocalized excitations with a finite center-of-mass momentum Q in order to maximize the correlation-function $C(t)$. This behavior may seem counterintuitive at first, as one would expect a localized excitation to yield stronger correlations. Yet, localization in configuration space gives rise to a flat momentum distribution and thus a superposition of eigenstates with different center-of-mass momenta Q. Even so, the finite-Q initial state can still be composed of localized excitations via superposition, so that

$$|\psi_Q\rangle = \sum_{j\in 2\mathbb{N}} e^{i\frac{Q}{2}j} a^\dagger_{j-1} a_j |\mathrm{DWP}\rangle, \tag{5.8}$$

with $|\mathrm{DWP}\rangle$ denoting the density-wave phase with two particles on every even lattice-site. The factor of two in the phase then accounts for the two-site hopping of fractional excitations in the microscopic model. In the effective model the initial state (5.8) corresponds to two adjacent occupied sites, so that $\psi_{\mathrm{SPE}} = e^{-iQX}\delta_{x,1}$. Then, the overlap with the bound eigenstates of the effective Hamiltonian takes the form

$$C_{\mathrm{B}} = \theta(|Q| - Q_{\mathrm{c}})\sqrt{1 - 4\cos^2 Q/2}, \tag{5.9}$$

where $\theta(x)$ is the Heaviside step-function. Likewise, the overlap with the scattering states is

$$C_q = \sqrt{2}\cos(q + \phi_{Q,q}). \tag{5.10}$$

The integral over the relative quasi-momentum q in eq. (5.7) can be carried out analytically, giving rise to a formal solution in terms of an infinite sum of Bessel-functions of the first kind: First, since the integrand $C_q\psi_q$ is periodic in q, we can express it in terms of a Fourier-series

$$C_q\psi_q = \sum_m c_m e^{iqn}, \tag{5.11}$$

where the Fourier-coefficients $c_m = \int dq\, C_q\psi_q$ take the form of hypergeometric functions. Integration over different relative momenta yields

$$\int_{-\pi}^{\pi} \frac{dq}{2\pi}\, C_q\psi_q e^{-iE_q t/\hbar} = \sum_m c_m e^{i\frac{\pi}{2}m} J_m(2z_Q t/\hbar), \tag{5.12}$$

where J_m is the m-th Bessel-function of the first kind. Since the Fourier-coefficients scale like $c_m \sim 1/m!$, this gives access to a powerful approximation scheme. On the other hand, the time-evolution is solely governed by the Bessel-functions and in turn allows us to calculate the scaling explicitly. At the critical center-of-mass

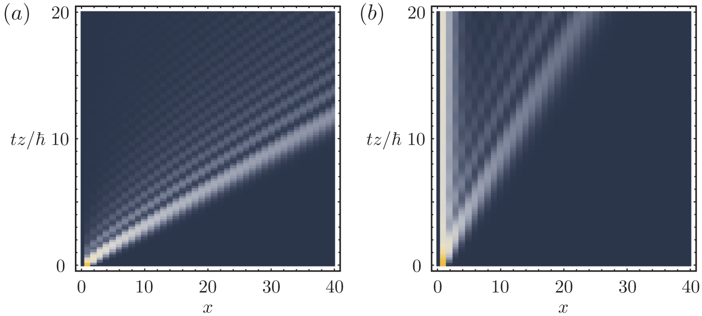

Figure 5.6: Time evolution of the relative wave-function $\psi(x)$: (a) For $Q = 0.3 Q_\mathrm{c} \leq Q_\mathrm{c}$, the wave-function is strongly localized at around a relative distance $x \approx tz_Q$. (b) For $Q = 0.8\,Q_\mathrm{c} > Q_\mathrm{c}$, the bound state adds an additional exponentially decaying contribution, with its maximum at $x = 1$.

momentum, the summation reduces to a closed-form expression, which yields the wave-function

$$\psi_\mathrm{SPE}(X, x) = e^{-iQ_c X} e^{-i\frac{\pi}{2}|x|} \left[J_{|x|}(2zt) + iJ_{|x|-1}(2zt) \right] . \tag{5.13}$$

The time-evolution of the wave-function for $Q = 0.3\,Q_\mathrm{c}$ and $Q = 0.8\,Q_\mathrm{c}$ is shown in Fig. 5.6 (a) and (b), respectively. The superposition of scattering states leads to a ballistic expansion of the fractional excitations with a velocity determined by the hopping energy z_Q. In turn, the two-particle wave-function ψ_SPE is strongly localized around a linearly growing relative distance $x \approx tz_Q/\hbar$, with some additional interference fringes appearing at smaller relative distances x, but propagating at the same velocity. On the other hand, the finite overlap with the bound state (5.6) for $Q > Q_\mathrm{c}$ creates an additional stationary peak at $x \approx 1$ (see Fig. 5.6(b)). With the scattering states moving away from each other, measurement of the wave-function amplitude at $x = 1$ on times $t \gg 1/z_Q$ allows us to single out the bound-state contribution. Formally, this can be cast in terms of a correlation-function

$$C(t) = |\psi_\mathrm{SPE}(X, x = 1)|^2 \tag{5.14}$$

on the effective lattice. In the microscopic lattice, $C(t)$ corresponds to $\langle P_i P_{i+1} \rangle$, with $P_i = n_i(n_i - 2)$ being the projection operator on singly-occupied sites. The time-evolution of $C(t)$ for different center-of-mass quasi-momenta is shown in

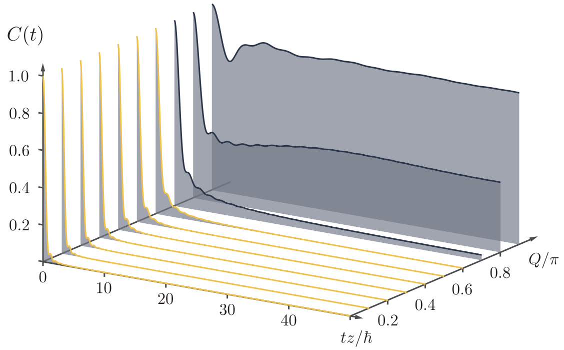

Figure 5.7: Time evolution of the correlation-function $C(t)$ for different center-of-mass quasi-momenta Q: Below the critical momentum $|Q| < Q_\mathrm{c}$, the correlation-function decays to zero, while for $|Q| > Q_\mathrm{c}$, the overlap with the emerging repulsively bound state leads to a finite probability for fractional excitations to stay at relative distance $x = 1$, resulting in a finite value of the correlation-function for $tz_Q/\hbar \gg 1$.

Fig. 5.7. For $Q < Q_c$, the correlation-function decays to zero with a characteristic behavior $\sim (tz_Q/\hbar)^{-3}$, and exhibits characteristic oscillations due to interference between the different scattering states. Furthermore, the correlation-function $C(t)$ exhibits an intermediate regime with a characteristic behavior $\sim (tz_Q/\hbar)^{-1}$. The time scale for the crossover between the long-time behavior and this intermediate regime diverges approaching the critical value Q_c. Consequently, the decay at $Q = Q_c$ is given by a critical behavior $\sim (tz_Q/\hbar)^{-1}$ for the correlation-function, in agreement with the analytical solution (5.13). The presence of a bound state is characterized by a saturation of the correlation-function

$$C(t) \to \theta(|Q| - Q_\mathrm{c})[1 - 4\cos^2 Q/2]^2 \tag{5.15}$$

for $tz_Q/\hbar \gg 1$, where the bound-state contribution grows steadily towards the edge of the Brillouin-zone and eventually becomes an eigenstate of the Hamiltonian at $|Q| = \pi$ with a constant correlation-function $C(t) = 1$. The characteristic beating of the correlation function is due to interference. Its frequency can be calculated directly by use of the formal analytic solution (5.7) to be

$$\omega^\pm = E_\mathrm{B} \pm E_\mathrm{SC}(q = 0) = z(1 - \cos^2 Q/2 \pm 2\cos Q/2). \tag{5.16}$$

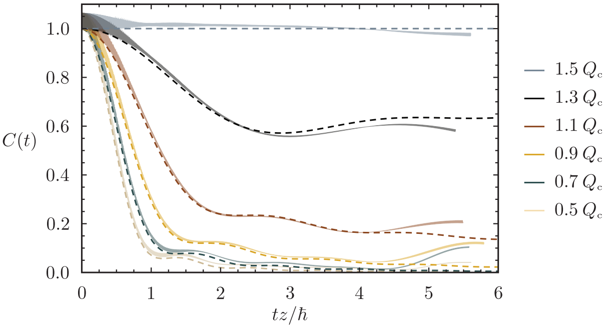

Figure 5.8: t-DMRG results (solid lines) in a finite lattice with $L = 30$ microscopic sites (i.e. $l = 16$ sites in the effective lattice) in comparison to the analytic results (dashed lines) in an infinite lattice for various center-of-mass momenta Q. Finite size effects start come into play a role at times $t \approx 4\hbar/z$.

This gives experimental access to the energy-gap between bound- and scattering-states, and allows for the measurement of the energy-diagram in Fig. 5.5.

5.5 Deviations from the Ideal Setup and *t*-DMRG

To confirm our perturbative results and to provide further insight into an experimental realization, we provide time-adaptive density matrix renormalization group (t-DMRG) simulations [145,146] of a single-particle excitation in the original tilted Bose-Hubbard model in eq. (5.1). Here, we use a realistically large lattice of $L = 30$ sites, which translates to $l = 16$ sites in the effective lattice. Time-evolution calculations are performed using second- and fourth-order Trotter decompositions. A comparison between the analytic correlation-function and the t-DMRG result is shown in Fig. 5.8. On the one hand, t-DMRG results show good agreement with the perturbative model. We find that the timescale of the correlation-function decay and the saturation values agree well with the analytic results. On the other hand, we observe deviations due to finite system size and finite values U, E, and w, which we discuss in the following. First, the simulations are performed in a finite-size system. This leads to revivals of the correlation-function $C(t)$ due to scattering of fractional excitations at the system boundaries. In a microscopic lattice of $L = 30$ sites, we find deviations due to finite-size at times $t \approx 4\hbar/z$. A hard-core model neglecting nearest-neighbor interaction that allows for an analytic solution even in a finite system, agrees well with the t-DMRG result and gives an estimate for revival times. From this, we can derive a lower boundary of $L \gtrsim 26$ to observe a signature for a bound state in the correlation-function. Second, the simulated correlation-function shows an additional high-frequency oscillation, which can be explained as follows: Since the initial state is not an energy eigenstate of the Hamiltonian for a finite ratio w/Δ, this leads to interference between different energy contributions, and ultimately in oscillations on the order of the excitation spectrum, namely Δ. We find that for a ratio of $\Delta/w \gtrsim 30$ the suppression of these oscillations is strong enough to see a clear correlation-function signal (see Fig. 5.8). Finally, the validity of the correlation-function is based on the stability of the density-wave phase. However, second-order processes in w/U and w/E allow the system to reach states with more than two particles on a single lattice-site (see ref. [140]). Our simulations show the probability for having three particles on a single lattice-site at times $t = 4\hbar/z$ of the order 10^{-6}.

5.6 Experimental Setup

In order to observe excitation decay as described above, one needs access to the correlation-function $C(t)$ via single-site resolution as demonstrated in the groups of Markus Greiner and Immanuel Bloch. The density-wave phase is prepared by an adiabatic tilt of the Mott-insulator phase, see ref. [2]. Single-site addressing [138] then allows for the creation of the initial single-particle excitation state $|\psi_Q\rangle$. Although current experiments can only resolve an even or odd number of atoms per lattice-site, this is no limitation in our case: Fractional excitations can still be observed as single atoms, whereas the density-wave phase with zero or two atoms per lattice-site show as zero atoms. Since the typical lifetime of an atom in an optical lattice is on the order of seconds, an effective hopping-rate $z \approx 1$ Hz should be sufficient for observation of the correlation-function saturation $C(t) \to const.$ If we assume a microscopic hopping-rate of $w = 15$ Hz, suppression of high-frequency oscillations requires a minimal single-particle excitation energy $\Delta \gtrsim 450$ Hz. Finally, an on-site interaction $U = 3.6$ kHz results in a strong suppression of effects on the order of $1/U$ as well as a stable broken-symmetry phase for the duration of the experiment. To limit the effect of the finite system size, we require a lattice-size of $L \gtrsim 26$ sites. Although the realization of such a large density–wave phase might be the hardest part to accomplish, a sufficiently large initial Mott-insulting state should be experimentally accessible via algorithmic cooling [147].

5.7 Conclusion

In chapter 5, we have studied the behavior of excitations in the tilted one-dimensional Bose-Hubbard model as recently realised in the group of Markus Greiner [2]. In the density-wave phase with two particles occupying every other lattice site, the experimentally accessible excitations are achieved by moving a single particle from a doubly-occupied site against the tilt by one site. Such a single-particle excitation carries an energy Δ, which is given by the difference between the tilt per lattice site E and the on-site interaction U. On the other hand, fundamental excitations in this system are domain-walls that correspond to singly occupied sites and separate the two possible realizations of the density-wave phase. These domain-walls each carry an energy of $\Delta/2$, and thus are fractional excitations. In this chapter, we thoroughly answered the question whether single-particle excitations decay into fractional excitations, or remain stable. To these means we employed a perturbative treatment which allowed us to derive an effective hard-core Boson model describing the time-evolution of the domain-walls. The dynamics of a single-particle excitation can then be calculated by an expansion into eigenfunctions of the effective Hamiltonian. The latter featured a single repulsively bound state above a critical center-of-mass momentum $Q_\mathrm{c} = 2\pi/3$, whose overlap with an initial single-particle excitation increased towards the edge of the Brillouin zone. Conversely, for center-of-mass momenta smaller than Q_c, a single-particle excitation can be fully described by the scattering states. We derived an analytic expression for the time evolution of such a single-particle excitation, and provided an in-depth analysis of the correlation-function $C(t)$ describing the probability for finding two domain-walls on adjacent lattice sites. We found that below the critical center-of-mass momentum, a single-particle excitation completely decays into a ballistically expanding state of two domain-walls. Above the critical center-of-mass momentum, we found a finite probability for the domain-walls to stay in a bound state, which showed as a finite value in the long-time behavior of the correlation-function $C(t)$. The validity of our approach was confirmed by the use of t-DMRG simulations created in collaboration with Jad Halimeh, Ian McCulloch and Ulrich Schollwöck, and gave insight into the limits of our perturbative analysis as well as the finite-size effects. Moreover, we discussed the implementation of our setup in state-of-the-art experiments, and gave parameters important for an actual measurement of fractional-excitation dynamics in cold atomic gas.

5.A Perturbation Theory

We start with a Hamiltonian H, which we decompose into its diagonal and off-diagonal components, that is

$$H \approx H_{\mathrm{D}} + H_{\mathrm{O}}. \tag{5.17}$$

For dominating diagonal elements H_{D}, we can approximate the above Hamiltonian via

$$H \approx H_{\mathrm{D}} + \sum_{I} \frac{H_{\mathrm{O}}|I\rangle\langle I|H_{\mathrm{O}}}{H_{\mathrm{D}} - \langle I|H_{\mathrm{D}}|I\rangle}, \tag{5.18}$$

where I denotes intermediate states. In the case of the tilted Bose-Hubbard model (5.1), the decomposition into diagonal and off-diagonal parts takes the form

$$\begin{aligned} H_{\mathrm{D}} &= \frac{U}{2}\sum_j n_j(n_j-1) - E\sum_j j n_j, \\ H_{\mathrm{O}} &= -w\sum_j \left(a_j^\dagger a_{j+1} + a_j a_{j+1}^\dagger\right). \end{aligned} \tag{5.19}$$

The intermediate states $|I\rangle$ contributing to the expectation value $\langle H\rangle$ for a single-particle excitation and two spatially separated fractional excitations are depicted in Fig. 5.9. Consequently, with $U, E \gg \Delta$, the leading order contributions are of the form $1/\Delta$. Thus, the energy difference V between a single-particle excitation and two fractional excitations take the form

$$V = E_{\mathrm{SPE}} - E_{\mathrm{2FE}} = \frac{2w^2}{\Delta}. \tag{5.20}$$

Likewise, the matrix element connecting a fractional excitation on site i to one on site $i \pm 1$ takes the form

$$z = \frac{2w^2}{\Delta}, \tag{5.21}$$

with intermediate states $|I\rangle$ shown in Fig. 5.9.

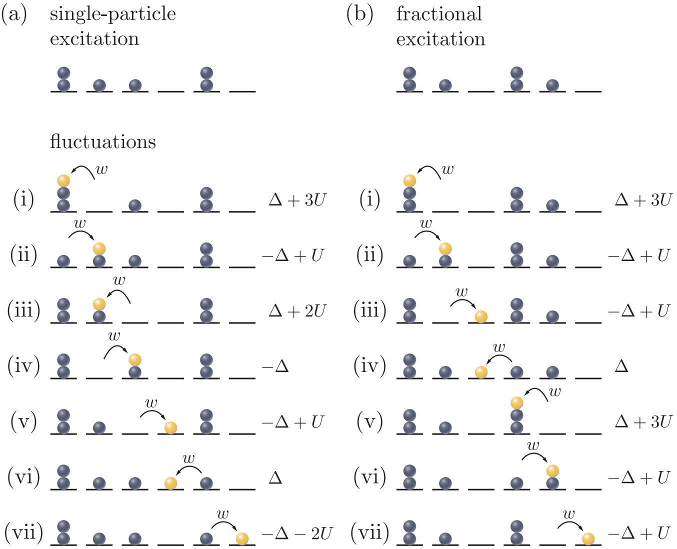

Figure 5.9: Second-order fluctuation processes contributing to the nearest-neighbor interaction: (a) Fluctuations of the single-particle excitation with intermediate energy. (b) Fluctuations of two domain-walls with intermediate energy. Since $U \gg \Delta$, only the processes (iv) and (vi) for the single-particle excitation and (iv) for the two domain-walls do contribute.

5.B Scaling-Limit

In the scaling-limit $z_Q t/\hbar \gg 1$, the Bessel-function of the first kind takes the approximate form

$$J_m(2z_Q t/\hbar) \approx e^{i\frac{\pi}{2}m} \sqrt{\frac{2}{\pi 2z_Q t/\hbar}} \cos\left(2z_Q t/\hbar - \frac{\pi}{4} - \frac{\pi}{2}m\right). \tag{5.22}$$

Hence, we can write the equation (5.12) in the form

$$\begin{aligned}&\sum_m c_m e^{i\frac{\pi}{2}m} J_m(2z_Q t/\hbar)\\ &\approx \sqrt{\frac{2}{\pi 2z_Q t/\hbar}} \left[\sin\left(\frac{2z_Q t}{\hbar} + \frac{\pi}{4}\right) \sum_{m\ \text{even}} c_m + i\cos\left(\frac{2z_Q t}{\hbar} + \frac{\pi}{4}\right) \sum_{m\ \text{odd}} c_m\right].\end{aligned}$$

The summation over even and odd Fourier-coefficients c_m can then be expressed as a superposition between the wave-functions at relative momentum $q = 0$ and $q = \pi$, respectively,

$$\sum_{m\text{even}} c_m = \sum_m \frac{c_m}{2} \left[e^{-i0x} + e^{-i\pi x} \right] = \frac{\psi_0 C_0 + \psi_\pi C_\pi}{2},$$

$$\sum_{m\text{odd}} c_m = \sum_m \frac{c_m}{2} \left[e^{-i0x} - e^{-i\pi x} \right] = \frac{\psi_0 C_0 - \psi_\pi C_\pi}{2}.$$

However, both $\psi_0 C_0$ and $\psi_\pi C_\pi$ vanish identically except at the critical center-of-mass momentum Q_c, where they take the form

$$c_m = \frac{e^{-i\frac{\pi}{2}x}}{2} \left(\delta_{|m|,x} + i\delta_{|m|,x-1} \right). \tag{5.23}$$

For a leading-order expansion we use the next order in the Bessel-function series, that is

$$J_m(2z_Q t/\hbar) \approx \frac{1-4m^2}{4} \sqrt{\frac{1}{2\pi Y^3}} \sin\left(-2z_Q t/\hbar + m\frac{\pi}{2} + \frac{\pi}{4} \right). \tag{5.24}$$

The term proportional to 1 will vanish identically according to the above calculation. We are thus left with the term proportional to m^2, so that the above equation reduces to

$$\sum_m c_m e^{i\frac{\pi}{2}m} J_m(2z_Q t/\hbar)$$
$$\approx \sqrt{\frac{1}{2\pi(2z_Q t/\hbar)^3}} \left[\cos\left(\frac{2z_Q t}{\hbar} + \frac{\pi}{4} \right) \sum_{m \text{ even}} m^2 c_m + i \sin\left(\frac{2z_Q t}{\hbar} + \frac{\pi}{4} \right) \sum_{m \text{ odd}} m^2 c_m \right]$$

By use of the relation $-\partial_q^2 f(q) = \sum_m m^2 f(m)$, the summations take the closed form

$$\sum_{m \text{ even}} m^2 c_m = \sum_m m^2 \frac{c_m}{2} \left[e^{-i0n} + e^{-i\pi n} \right] = -\frac{\psi_0'' C_0'' + \psi_\pi'' C_\pi''}{2} = -4z_Q^2 \frac{z^2 + z_Q^2}{(z^2 - z_Q^2)^2},$$

$$\sum_{m \text{ odd}} m^2 c_m = \sum_m m^2 \frac{c_m}{2} \left[e^{-i0n} - e^{-i\pi n} \right] = -\frac{\psi_0'' C_0'' - \psi_\pi'' C_\pi''}{2} = 4z_Q^2 \frac{2zq_Q}{(z^2 - z_Q^2)^2},$$

where the prime denotes derivatives with respect to q. The resulting long-time behavior for $Q \neq Q_\mathrm{c}$ is thus given by

$$\psi = -\sqrt{\frac{2}{\pi(2z_Q t/\hbar)^3}}\left[\frac{z_Q^2}{(z-z_Q)^2}e^{i\frac{\pi}{4}+i2z_Q t} + \frac{z_Q^2}{(z+z_Q)^2}e^{-i\frac{\pi}{4}-i2z_Q t}\right]. \tag{5.25}$$

Here, it is important to note that the coefficients diverge for $z_Q \to z$, which corresponds to $Q \to Q_\mathrm{c}$.

5.C Eigenstates of the Effective Hamiltonian

5.C.1 First-Quantized Version of the Hard-Core Boson Hamiltonian

It is most convenient to express the hard-core Boson Hamiltonian (5.5) in a first-quantized form in order to find the two-particle eigenstates. Formally, this can be done by introducing a non-symmetrized coordinate basis $\{|i,j\rangle\}$ where i and j denote are the positions of the two particles in the lattice. A general two-particle state $|\psi\rangle$ then decomposes like

$$|\psi\rangle = \sum_{i,j}\psi(i,j)|i,j\rangle, \tag{5.26}$$

where $\psi(i,j)$ is the probability amplitude for finding the first particle at position i and the second at position j. In this basis, the Schrödinger-equation takes the form

$$\begin{aligned} &-z\sum_{i,j}\Big[\psi(i+1,j)+\psi(i,j+1)+\psi(i-1,j)+\psi(i,j-1)\Big]|i,j\rangle \\ &\qquad + V\sum_{i,j}\psi(i,j)\left(\delta_{i+1,j}+\delta_{i-1,j}\right)|i,j\rangle = E_Q\sum_{i,j}\psi(i,j)|i,j\rangle, \end{aligned} \tag{5.27}$$

where E_Q is the center-of-mass energy. By using the orthogonality relation of the coordinate-basis vectors, a projection of the above equation on a basis bra $\langle i',j'|$ yields

$$\begin{aligned} &-z\Big[\psi(i+1,j)+\psi(i,j+1)+\psi(i-1,j)+\psi(i,j-1)\Big] \\ &\qquad + V\psi(i,j)\left(\delta_{i+1,j}+\delta_{i-1,j}\right) = E\psi(i,j). \end{aligned} \tag{5.28}$$

The translational invariance of this equation gives rise to a conservation of the total quasi momentum Q. In turn, the wave-function factorizes as $\psi(i,j) = e^{iQX}\psi_q(x)$, where $x = i - j$ and $X = (i+j)/2$ are the relative and center-of-mass coordinates, respectively. Here we restrict ourselves to positive relative coordinates x only, which also takes care of the symmetrization of the wave-function. The resulting Schrödinger-equation (5.28) thus reads

$$-ze^{iQX}2\cos\frac{Q}{2}\big[\psi(x+1)+\psi(x-1)\big] + V\delta_{|x|,1}e^{iQX}\psi(x) = E_Q e^{iQX}\psi(x). \quad (5.29)$$

Last, by only keeping track of the relative coordinate, eq. (5.29) takes its final compact form

$$-z_Q\big[\psi(x+1)+\psi(x-1)\big] + V\delta_{|x|,1}\psi(x) = E\psi(x), \quad (5.30)$$

where $z_Q = 2z\cos Q/2$ the center-of-mass hopping-rate.

5.C.2 Bound States

In a one-dimensional system, a bound state decays exponentially with the relative distance of the constituents. We use an ansatz $\psi(x \geq 1) = \mathcal{N}\Lambda_Q^{|x|-1}$ with $\mathcal{N}$ a normalization-constant and $\psi_{\mathrm{B}}^{Q}(x=0) = 0$ due to the hard-core nature of the interaction. This yields the two equations

$$x = 1: \quad -z_Q\Lambda_Q + V - E_Q = 0, \quad (5.31)$$

$$x \geq 2: \quad -z_Q(\Lambda_Q^{x-2} + \Lambda_Q^{x}) - E_Q\Lambda_Q^{n-1} = 0. \quad (5.32)$$

The first equation of (5.32) provides an expression for the bound-state energy,

$$E_Q = -z_Q\frac{1+\Lambda_Q^2}{\Lambda_Q}. \quad (5.33)$$

Substitution of E_Q in the second equation of (5.32) then leads to

$$-z_Q\Lambda_Q + V + z_Q\frac{1+\Lambda_Q^2}{\Lambda_Q} = 0. \quad (5.34)$$

which gives rise to $\Lambda_Q = -z_Q/V = -2\cos Q/2$.

5.C.3 Scattering States

The scattering states are obtained by using a standard plane-wave ansatz with an additional scattering-phase shift $\phi_{Q,q}$, that is

$$\psi_q = \sqrt{2}(1-\delta_{x,0})\,\mathrm{sign}\,x\cos(q|x|+\phi_{Q,q}). \tag{5.35}$$

This ansatz solves the Schrödinger-equation for all x except $|x|=1$, giving rise to the condition

$$\left(\cos q + 2\cos\frac{Q}{2}\right)\cos\phi_{Q,q} - \sin q\sin\phi_{Q,q} = 0, \tag{5.36}$$

which can be solved by

$$\phi_{Q,q} = \arctan\frac{\cos q + 2\cos\frac{Q}{2}}{\sin q}. \tag{5.37}$$

5.C.4 Green's-Function Approach

There are at least two ways in order to derive a two-particle bound state in a Bose-Hubbard Hamiltonian. Here, we show that the calculation via the exponential ansatz [144] yields the same result as a Green's-function approach [143]. Poles in the scattering amplitude $f(Q,E)$ indicate the presence of a bound sate. For nearest-neighbor interactions the former reduces to [148]

$$\begin{aligned} f(Q,E) = -\frac{1}{G_Q^0(E;n)} + 2V\frac{G_Q^0(E;0)-G_Q^0(E;1)}{G_Q^0(E;0)} \\ \times\frac{\cos q - \frac{G_Q^0(E;1)}{G_Q^0(E;0)}}{1+2V\frac{G_Q^0(E;1)}{G_Q^0(E;0)} - V[G_Q^0(E;0)+G_Q^0(E;2)]}, \end{aligned} \tag{5.38}$$

where $G_Q^0(E;n)$ is the free Green's-function. In turn, the last factor and, accordingly, the scattering amplitude diverges for

$$1+2V\frac{G^2(1)}{G(0)} - V[G(0)+G(2)] = 0. \tag{5.39}$$

By use of the explicit form for a free one-dimensional Green's-function [149]

$$
\begin{aligned}
G^0_Q(E,x) &= \int\limits_{-\pi}^{\pi} \frac{dq}{2\pi} \frac{e^{iqx}}{E - 4z\cos Q/2} \\
&= (-1)^x \mathrm{sign}^{x+1} E \, \frac{e^{-|x|\cosh^{-1}\left|\frac{E}{4z\cos Q/2}\right|}}{\sqrt{E^2 - (4z\cos Q/2)^2}},
\end{aligned}
\tag{5.40}
$$

we can show that eq. (5.39) is equivalent to eq. (5.33), and yields the same bound state energy.

5.D Hard-Core Model without Interaction

In this section we provide a model to estimate revivals of the correlation-function (5.14) due to finite-size effects. Since these revivals are due to scattering of excitations at the system boundaries, we expect interactions to play a minor role. Hence, we approximate the Hamiltonian (5.5) by neglecting nearest-neighbor interaction completely and just keep the hard-core constraint. The major advantage of this approximation is that it allows for an analytic solution even in a finite-size system. The approximate Hamiltonian for an n site lattice then reduces to

$$
H = -z \sum_{i=1}^{\bar{n}-1} b_i^\dagger b_{i+1} + b_{i+1}^\dagger b_i. \tag{5.41}
$$

The two-particle eigenstates of the corresponding Schrödinger-equation take the form

$$
\psi_2(x,y) = \begin{cases} \psi_1^k(x)\psi_1^p(y) - \psi_1^p(x)\psi_1^k(y), & x > y, \\ \psi_1^p(x)\psi_1^k(y) - \psi_1^k(x)\psi_1^p(y), & x < y, \end{cases} \tag{5.42}
$$

where $\psi_1^k(x)$ is single particle eigenstate defined via

$$
\psi_1^k(x) = \sqrt{\frac{2}{\bar{n}+1}} \sin kx, \quad k = \frac{j\pi}{\bar{n}+1}, \quad j = 1, \ldots \bar{n}. \tag{5.43}
$$

Since there are no bound states in this model, the two-particle energy is given by $E_2 = -2z(\cos k + \cos p) = -2z_Q \cos q$. The wave-function for an initial state of two particles on adjacent lattice-sites with center-of-mass momentum Q reads

$$\psi_2(0) = e^{iQ\frac{x+y}{2}} \left[\delta_{x-y,1} + \delta_{x-y,-1}\right]. \tag{5.44}$$

Time-evolution of this initial state is then most conveniently derived via Fourier-decomposition. Since we know the energy in the momentum basis, we can calculate the time-evolution for the initial state (5.44) in the form of a large sum of oscillating terms. In the limit of an infinite number of lattice-sites the summation can be approximated by an integral, and reduces the wave-function to the closed-form expression

$$\psi_2(t) = e^{iQ(x+y+1)} \sum_{s=\pm1} s\, e^{-is\frac{\pi}{2}(x-y-s)} J_{x-y-s}(-2z_Q t/\hbar). \tag{5.45}$$

As one might expect, deviations from the analytical result occur at a characteristic time-scale τ_f that scales with the system-size (see Fig. 5.11). Due to the ballistic propagation the scaling is easily understood in terms of scattering of fundamental excitations at the system boundaries. Hence we propose to measure the correlation-function $C(t)$ in the middle of the lattice in order to maximize the time it takes a scattered particle to reach the point of measurement.

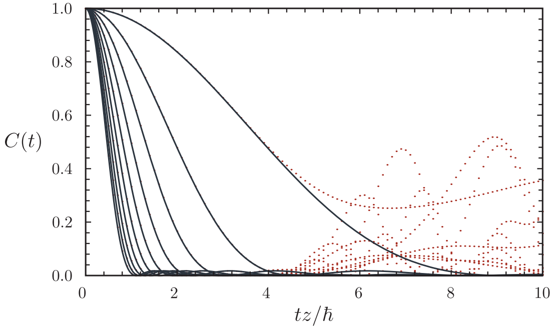

Figure 5.10: Finite size effects in the hard-core Boson model: The plot shows the analytical solution for the hard-core Boson model (5.41) for an infinite lattice (solid blue lines) and a finite lattice of size $l = 30$ for various center-of-mass momenta ranging from $Q = \pi/6$ to $\pi/2$. Deviations from the analytical solution can be seen at times $tz_Q/\hbar \approx 4$. These deviations are due to finite-size effects, that is scattering at the system boundaries.

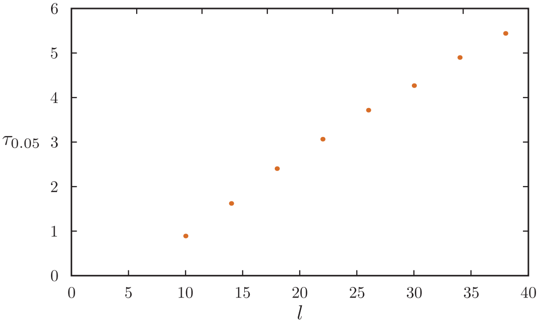

Figure 5.11: Scaling of finite-size effects with the system size l. The plot shows the time $\tau_{0.05}$ at which deviations averaged over different Q values reach 0.05. As expected, the data suggests a linear scaling of $\tau_{0.05}$ due to the ballistic motion of particles in a lattice.

CHAPTER 6

Basic Concepts

6.A Rydberg Atoms

An atom in a highly-excited electronic state close to the ionization limit is called a Rydberg atom [150]. These atoms show very extreme properties, which are mostly based on their huge spatial dimension, exceeding the radius of normal atoms by several orders of magnitude. Hence, Rydberg atoms are easily polarizable, which in turn makes them very susceptible to electric fields and account for their huge van der Waals interaction. It is exactly this property that makes them a prime candidate to study quantum many-body physics in cold atomic gases.

6.A.1 General Properties

Here we concentrate on Rydberg atoms with only a single electron excited into a high electronic state. In consequence, the atom shows a structure similar to Hydrogene, where one electron is in a state with high principal quantum-number n bound to a positively charged ion. Since the Hydrogen wave-function is strongly localized at a distance $\sim n^2$, the electron will feel only the excess charge of the shielded core, which in turn justifies the treatment as a two-body system. Any effects due to the inner structure of the core can be included via a renormalization of the principal quantum-number $n^* = n - \delta$, with $\delta < 1$. The Rydberg-Ritz formula [36] then allows for the calculation of explicit values of the so called quantum-defects δ, and have been confirmed in several experiments [151]. Most properties of Rydberg atoms strongly depend on their principal quantum-number n, or its renormalized equivalent n^*. A short compilation of the scaling-laws for several important properties is shown in table 6.1.

Property	Scaling	^{87}Rb $\|5s\rangle$	^{87}Rb $\|43s\rangle$
Binding energy	$(n^*)^{-2}$ [150]	4.18 eV	8.56 meV [49]
Level spacing	$(n^*)^{-3}$ [150]	2.5 eV	109.99 GHz [49]
Orbit-radius	$(n^*)^{2}$ [150]	0.298 nm	0.126 μm [49]
Polarizability	$(n^*)^{7}$ [152]	-79.4 mHz cm^2/V^2	8.06 MHz cm^2/V^2 [49]
Transition dipole moment	$(n^*)^{-3/2}$ [49]	-	-0.0176 a.u. [49]
Natural lifetime	$(n^*)^{3}$ [150]	-	99 μs [49]
C_6-coefficient	$(n^*)^{11}$ [150]	5.23 $\cdot 10^{-8}$Hz μm^6	189 MHz μm^6 [49]

Table 6.1: Scaling properties of Rydberg atoms and exemplary values for the ^{87}Rb $|5s\rangle$ ground-state compared to the ^{87}Rb $|43s\rangle$ Rydberg state.

Since alkali Rydberg atoms closely resemble a Hydrogen configuration, one can use the analytic Hydrogen wave-function in order to calculate dipole matrix-elements. If we reduce our discussion to s-states, the only non-vanishing dipole matrix-element is given by $\langle n'p|d|ns\rangle$, where d is the dipole-operator. On the other hand, this expression takes only significant values at the origin, and thus yields the scaling

$$\langle n'p|d|ns\rangle \sim n^{*-3/2}. \tag{6.1}$$

The application of Fermi's Golden rule allows us to calculate the natural lifetime of a Rydberg-state as

$$\gamma = \frac{2\pi}{\hbar}\sum_{\mathrm{f}} |\langle \psi_{\mathrm{i}}|d|\psi_{\mathrm{f}}\rangle|^2 g(\psi_{\mathrm{f}}) \tag{6.2}$$

where g denotes the density of states. The dominating decay-channel is the one to the lowest-energy state. The dipole-operator for this particular transition scales as $d \sim (n^*)^{-3/2}$, resulting in a cubic scaling with the principle quantum-number for the natural lifetime [49], that is $\tau \sim (n^*)^3$. For a typical Rubidium Rydberg-state like $|43s\rangle$ we find a natural lifetime of $\tau \approx 100$ μs that, again, exceeds the natural lifetime of lowly electronic excitations by several orders of magnitude. Even so, blackbody-radiation increases the decay-rate from the Rydberg-state, and ultimately results in a modified scaling behavior of the lifetime $\tau \sim (n^*)^2$.

6.A.2 Interactions

Under the assumption that the spatial separation x between the atoms is larger than the LeRoy-radius, we can expand the interaction-potential V between the atoms in a power-series, so that

$$V(x) = \sum_m \frac{C_m}{x^m}. \tag{6.3}$$

The first non-vanishing term of this expansion is the C_3 coefficient, which can be derived within quantum-defect theory [36]. Then, a two-level approximation of the interaction Hamiltonian takes the form

$$H = \begin{pmatrix} \Delta_{\mathrm{F}} & VY \\ VY & 0 \end{pmatrix}, \tag{6.4}$$

where Δ_{F} is the Förster defect energy, $V = C_3/x^3$ and Y is a geometry factor that accounts for angular momentum properties [37]. A straightforward calculation yields the energy eigenvalues

$$V_{\pm}(x) = \frac{\Delta_{\mathrm{F}}}{2} \pm \frac{1}{2}\sqrt{\Delta_{\mathrm{F}}^2 + V^2Y^2}. \tag{6.5}$$

For small inter-atom separation x, the interaction term $V = C_3/x^3$ dominates, and results in a dipole-dipole interaction. Conversely, for large inter-atom separation, the interaction is small as compared to the Förster defect-energy, and, as a result, a leading order expansion leads to a van der Waals interaction-potential,

$$V_{-} = V^2Y^2 \approx \frac{C_6}{x^6}. \tag{6.6}$$

The resulting van der Waals coefficient exhibits a strong dependence on the principal quantum-number, in particular $C_6 \approx (n^*)^{11}$. The crossover between these two regimes takes place at $x_{\mathrm{c}} \sim |VY/\Delta|^3$, and is usually smaller than the distance between Rydberg-excitations. Still, the longer range resonant dipole-dipole coupling $V \sim 1/x^3$ can be realised by using an electric microwave-field.

6.A.3 Coherent Production

Most experiments use a two-photon transition in order to excite an atom to a high-lying Rydberg-state. In the following, we assume that our atom is of the

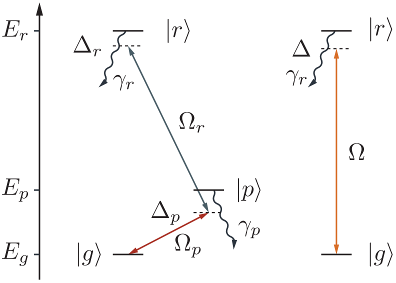

Figure 6.1: Setup for the coupling between ground and Rydberg-state $|g\rangle$ and $|r\rangle$, respectively, via the intermediate p-state. The Rabi-frequency and detuning driving the transition between ground and p-state are Ω_p and Δ_p. Likewise, the Rabi-frequency and detuning for the transition between p- and Rydberg-state are Ω_r and Δ_r. In addition, the decay rates from the intermediate p-state is γ_p, whereas the decay rate from the Rydberg-state is γ_r. For a strongly suppressed intermediate state, the internal structure can be reduced to an effective two-state system with two-photon Rabi-frequency Ω and total detuning Δ.

alkali type, or, more specifically, the species ^{87}Rb, which in general is considered to be the workhorse of atomic physics due to its convenient hyperfine-structure. We therefore start from an initial low-lying s-state, and excite the atom via a red laser to a low p-state, say $|5s\rangle \to |5p\rangle$. A second, blue laser then excites to the final Rydberg-state, which we assume to be an s-state again. In order to avoid inhomogeneous light intensities due to absorption [49], most experiments use a far off-resonant coupling to the intermediate state, $\Delta_p \gg \Omega_p$. The intermediate p-state can then be adiabatically eliminated [51], and the resulting Hamiltonian takes the form of an effective two-state system,

$$H_{\text{micro}} = -\hbar\Delta \sum_i S_z^i + \hbar\Omega \sum_i S_x^i, \tag{6.7}$$

where $S_z^i = (|r\rangle\langle r| - |g\rangle\langle g|)/2$ and $S_x^i = (|r\rangle\langle g| + |g\rangle\langle r|)/2$ are the spin operators in the z and x direction, respectively. The two-photon Rabi-frequency Ω can be expressed in terms of the initial Rabi-frequencies and the detuning from the intermediate state, so that

$$\Omega = \frac{\Omega_p \Omega_c}{2|\Delta_c|}. \tag{6.8}$$

On the other hand, the total detuning Δ takes the form

$$\Delta = \Delta_c + \Delta_p + \frac{\Omega_c^2}{4\Delta_c} + \frac{\Omega_p^2}{4\Delta_p}, \tag{6.9}$$

where the last two terms are due to the ac-Stark-shift of the respective upper levels. In most cases, one can neglect those Stark-shift terms, hence the total detuning reduces to the compact form $\Delta = \Delta_c + \Delta_p$.

6.A.4 Blockade Mechanism and Collective States

Strong interaction between excitations gives rise to a so-called blockade-mechanism for excitations [64, 153]. More specifically, the interaction-potential V between excited states exceeds the excitation line-width W, and thus only allows for a single excitation. To account for this effect, we can define a blockade-condition via

$$V > W. \tag{6.10}$$

Here it is important to note that the blockade-mechanism is a general concept and not limited to atomic physics. However, in the following we concentrate on Rydberg-atoms, as this is the only application of the blockade-mechanism in this work. Since the natural lifetime of Rydberg-atoms scales with the cube of the principle quantum-number, the excitation line-width is dominated by the power-broadening of the excitation laser and the detuning. Usually, the interaction is of a van der Waals type, and reduces eq. (6.10) to the condition

$$\frac{C_6}{x^6} > 2\hbar\sqrt{\Delta^2 + \Omega^2}, \tag{6.11}$$

and gives rise to the definition of the two-particle blockade-radius [41]

$$\xi_0 = \left(\frac{C_6}{2\hbar\sqrt{\Delta^2 + \Omega^2}} \right)^{\frac{1}{6}}. \tag{6.12}$$

The reduction of the Hilbert-space due to blockade of additional excitations has further consequences for the dynamics of the system. Consider an ensemble of

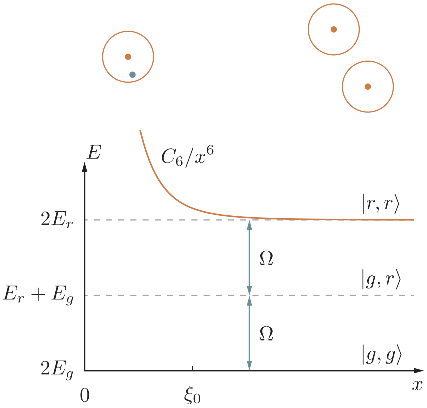

Figure 6.2: For large inter-atom separation, both atoms can acquire a Rydberg-excitation. Conversely, for small separations, the van der Waals interaction shifts the energy level of the state $|r\rangle|r\rangle$ out of resonance and thus prevents a subsequent Rydberg-excitation. The two-particle blockade-radius ξ_0 is then determined by the interaction and the line-width of the driving laser.

N atoms individually coupled via a coherent two-photon process to a Rydberg-state, with two-photon Rabi-frequency Ω and total detuning Δ. The Hamiltonian describing this system then takes the form of equation (6.7). If we further assume that the spatial confinement of the whole atomic ensemble is smaller than the blockade-volume ξ_0^3, the system can only support a single excitation. Thus, the Hilbert-space is spanned by the ground state $|g\rangle$ and N excited states $|i\rangle$ defined via

$$|G\rangle = \otimes_i |g_i\rangle, \quad |i\rangle = |e_i\rangle \otimes_{j\neq i} |g_j\rangle. \tag{6.13}$$

Although in principle all states $|i\rangle$ are accessible, the Hamiltonian (6.7) only couples to the symmetric superposition of these excited states

$$|W\rangle = \frac{1}{\sqrt{N}} \sum_{i=1}^{N} |i\rangle. \tag{6.14}$$

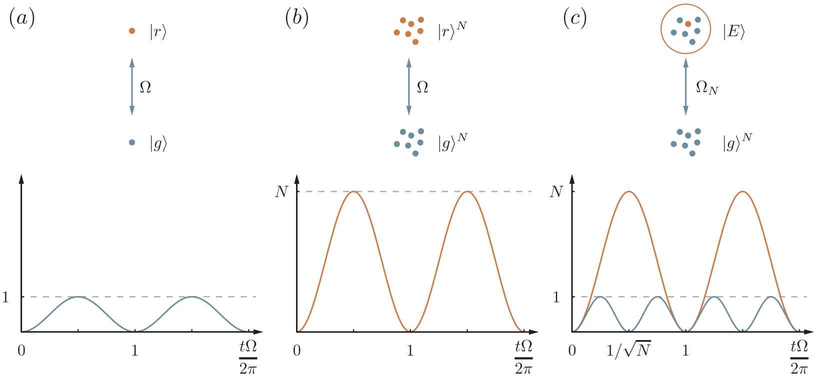

Figure 6.3: Excitation dynamics of a single atom (a), N non-interacting atoms (b), and the collective state (c) as is defined in eq. (6.14). Since the *super-atom* can only support a single excitation, it shows the same maximum number of excitations as the single atom. Yet, the bosonic enhancement yields the same quadratic increase in the number of excitations as in the non-interacting case (b).

In consequence, the system again reduces to an effective two-level system described by the Hamiltonian

$$H = \frac{\hbar\Omega_N}{2}\left(|W\rangle\langle G| + |G\rangle\langle W|\right) + \frac{\hbar\Delta}{2}\left(|W\rangle\langle W| - |G\rangle\langle G|\right), \qquad (6.15)$$

where $\Omega_N = \sqrt{N}\Omega$ is the collective Rabi-frequency. It is this effective Hamiltonian that coined the term *super-atom* [154], as the whole ensemble behaves again like one of its constituents. The increase in the characteristic timescale by a factor of $\sqrt{N}$ is in analogy to the enhancement of the spontaneous decay-rate predicted in ref. [59].

6.B Open Quantum-Systems

In the most general case, an open quantum-system is one that interacts with the environment. By definition, the environment cannot be controlled on a quantum level despite its time-evolution being governed by quantum-mechanics. Therefore, the interaction with the quantum-system adds an unknown component to the dynamics, which in turn cannot be described within coherent time-evolution predicted by the Schrödinger-equation, but has to be treated within a more general approach. However, not being able to control the environment on a quantum level does not mean not being able to control it at all: most often the nature of the coupling together with macroscopic parameters such as the temperature are known, and allow one to either limit the environmental influence or design it in a fashion that benefits ones means [155].

6.B.1 Reduced Density-Matrix

One of the general principles of quantum mechanics is that every observable corresponds to an operator A [67,156]. The expectation value of this observable then takes the form of a trace

$$\langle A \rangle = \operatorname{tr} \rho A, \tag{6.16}$$

where ρ is the density-matrix of the system on which the measurement takes place. In general, ρ describes both the system one in interested in and the lab including the PhD-student performing the measurement. Yet one (or, more specifically, the supervisor) is usually interested in the quantum-system S alone, not the macroscopic environment E. In turn, any operator corresponding to an observable on S alone can be decomposed via $A = A_S \otimes \mathrm{id}_E$, where id_E is the identity operator on the environment E. Then, by defining the partial trace tr_S and tr_E over system and bath degrees of freedom, respectively, we can write the expectation value of an observable $A = A_S \otimes \mathrm{id}_E$ as

$$\langle A \rangle = \mathrm{tr}_S \left[A_S \mathrm{tr}_E \rho \right]. \tag{6.17}$$

The density-matrix $\rho_S = \mathrm{tr}_E\, \rho$ is called the reduced density-matrix, and allows to describe the time-evolution of an open quantum-system in terms of system degrees of freedom alone. Indeed, a measurement performed on the open system then takes the form

$$\langle A_S \rangle = \mathrm{tr}_S A_S \rho_S, \tag{6.18}$$

in analogy to eq. (6.16). On the downside, the time-evolution of ρ_S is no longer described within the Liouville-equation, but requires a more general approach, which we discuss below.

6.B.2 Master-Equation

The dynamics of the reduced density-matrix ρ_S can be described in terms of a master-equation, where the individual environmental degrees of freedom are removed from the equation of motion. The resulting equation then reads [156]

$$\dot{\rho} = -\frac{i}{\hbar}\left[H_S, \rho_S\right] + \int\limits_0^t dt' \, \mathrm{tr}_E \left[K(t-t')\rho(t')\right] . \tag{6.19}$$

The first term describes the coherent time-evolution of the quantum-system in analogy to the Liouville-equation, whereas the second term accounts for processes induced via system-environment interaction. It is the operator $K(t-t')$ that encodes all information about the environment and its coupling to the quantum-system. Integration over t' results in the time-evolution of ρ that is influenced by all prior states of both the system and the environment.

Despite this very general form of the master-equation, it can be reduced to a fairly easy to handle differential form. This is based on two approximations that are both well justified for a large variety of systems. First, under the Born-approximation one assumes that the interaction between the system and individual environment degrees of freedom is weak, so that the back-action from the system to the environment is small. This allows us to replace the total density-matrix ρ by a product $\rho_{\mathrm{E}} \otimes \rho_{\mathrm{S}}$, where the environment density-matrix ρ_{E} does not change in time. Even so, this does not necessarily mean that the influence of the environment is small. Second, in the Markov-approximation one neglects any influence from previous events at times t'. To put it another way, the environment is assumed to have no memory, and thus forgets the quantum state of the system immediately. Under these approximations it can be shown [156] that the master-equation (6.19) reduces to the so called Lindblad-form

$$\dot{\rho} = -\frac{i}{\hbar}\left[H_S, \rho_S\right] + \sum_i \frac{\Gamma_i}{2}\left[2c_i\rho c_i^\dagger - c_i^\dagger c_i \rho - \rho c_i^\dagger c_i\right] . \tag{6.20}$$

Again, the first term accounts for the coherent time-evolution, whereas the second describes non-coherent processes due coupling of the quantum-system to the environment. The operators c_i are called jump-operators, and, true to their name, incoherently jump the system from one state into the other with a rate Γ_i. The precise form of the jump-operators c_i and the rates Γ_i is subject to the environment and its coupling. A major advantage of this master-equation over the first one is its differential form and consequently its locality in time. Even if no analytic solution exists, it can most often be treated numerically by standard routines for solving systems of differential equations.

6.C Wigner Quasi-Probability Distribution

The Wigner-function or Wigner quasi-probability distribution is a phase space representation of a density-matrix ρ [71]. To be more precise, it is a Weyl-Wigner transformation [78] of the density-matrix, defined via

$$W(q,p) = \frac{1}{2\pi\hbar} \int dy \left\langle q + \frac{y}{2} \middle| \rho \middle| q + \frac{y}{2} \right\rangle e^{\frac{ipy}{\hbar}}, \tag{6.21}$$

where $|q \pm y/2\rangle$ are eigenkets of the position operator. For a pure state $\rho = |\psi\rangle\langle\psi|$, the Wigner-function takes the form

$$W(q,p) = \frac{1}{2\pi\hbar} \int dy \, \psi^* \left(q + \frac{y}{2}\right) \psi \left(q + \frac{y}{2}\right) e^{\frac{ipy}{\hbar}}. \tag{6.22}$$

Integration over all momenta p gives the probability-density for the spatial coordinate q, that is

$$\int dp \, W(q,p) = |\psi(q)|^2. \tag{6.23}$$

Likewise, integration over the the spatial coordinate q yields

$$\int dq \, W(q,p) = |\psi(p)|^2. \tag{6.24}$$

It directly follows that the Wigner-function is normalized in the sense that

$$\int dq \, dp \, W(q,p) = 1. \tag{6.25}$$

Here it is important to stress that despite its name, the Wigner quasi-probability distribution is not a true probability-distribution since it can take negative values. In turn, a state with a negative Wigner-function is then called non-classical. One of the most prominent non-classical states is a Fock-state containing a single

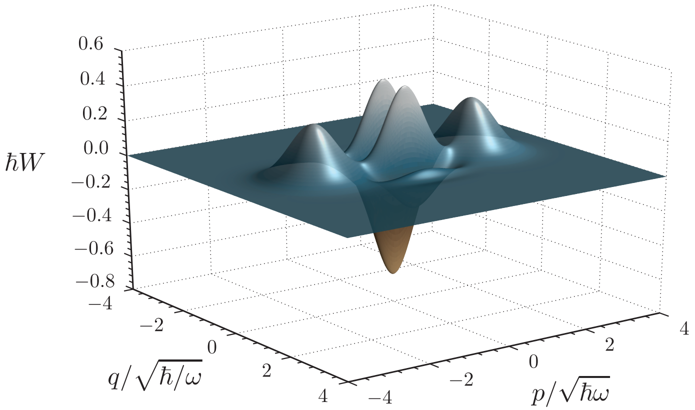

Figure 6.4: Wigner-function for an odd cat-state $|\text{odd cat}\rangle = |\alpha = 2\rangle - |\alpha = -2\rangle$

excitation. Its Wigner-function is easily calculated to be [78]

$$W_{n=1} = \frac{1}{\pi}\, e^{-p^2-q^2}(2p^2 + 2q^2 - 1), \tag{6.26}$$

and exhibits a negative dip in the middle, that is a clear telltale for its non-classical nature. Likewise, the most classical state imaginable is a coherent state, that is an eigenstate of the annihilation-operator $a|\alpha\rangle = \alpha|\alpha\rangle$. Its Wigner-function takes the form of a Gaussian [78],

$$W_\alpha = \frac{1}{\pi}\, e^{-2(q-\alpha)^2-2p^2}, \tag{6.27}$$

and is centered around α in the phase-space plane. In contrast to the Fock-state, the Wigner-function for a coherent state stays positive for all values of p and q.

Fig. (6.4) shows the Wigner-function for a Schrödinger cat, meaning the quantum superposition of two classically distinct states. In this particular example, the latter are two coherent states $|\alpha\rangle$ and $|-\alpha\rangle$. A statistical mixture of the coherent states would only feature the two *lumps* representing the dead and living cat centered at α and $-\alpha$, respectively. In contrast, the odd cat $|\text{odd cat}\rangle = |\alpha\rangle - |-\alpha\rangle$ shown here exhibits oscillations around $p = q = 0$. For the sake of completeness, we give the explicit expression of the Wigner-function of this particular cat,

$$W_{\text{oddcat}} = \frac{1}{\pi} \frac{e^{-2(q-\alpha)^2-2p^2} + e^{-2(q+\alpha)^2-2p^2} - 2e^{-2p^2-2q^2} \cos 4p\alpha}{1+e^{-2\alpha^2}}. \tag{6.28}$$

Bibliography

[1] M. Lewenstein, A. Sanpera, and V. Ahufinger, *Ultracold Atoms in Optical Lattices: Simulating quantum many-body systems*, Oxford University Press, 2012.

[2] J. Simon et al., Nature **472**, 307 (2011).

[3] M. H. Anderson, J. R. Ensher, M. R. Matthews, C. E. Wieman, and E. A. Cornell, Science (New York, N.Y.) **269**, 198 (1995).

[4] F. Dalfovo, S. Giorgini, and S. Stringari, Reviews of Modern Physics **71**, 463 (1999).

[5] E. A. Cornell and C. E. Wieman, Reviews of Modern Physics **74**, 875 (2002).

[6] W. Ketterle, Reviews of Modern Physics **74**, 1131 (2002).

[7] O. Morsch and M. Oberthaler, Reviews of Modern Physics **78**, 179 (2006).

[8] I. Bloch and W. Zwerger, Reviews of Modern Physics **80**, 885 (2008).

[9] H. Stoof, M. Houbiers, C. Sackett, and R. Hulet, Physical Review Letters **76**, 10 (1996).

[10] C. Chin, P. Julienne, and E. Tiesinga, Reviews of Modern Physics **82**, 1225 (2010).

[11] S. L. Cornish, N. R. Claussen, J. L. Roberts, E. A. Cornell, and C. E. Wieman, Physical Review Letters **85**, 1795 (2000).

[12] D. Jaksch, C. Bruder, J. Cirac, C. Gardiner, and P. Zoller, Physical Review Letters **81**, 3108 (1998).

[13] G.-B. Jo et al., Physical Review Letters **108**, 045305 (2012).

[14] M. P. A. Fisher, G. Grinstein, and D. S. Fisher, Physical Review B **40**, 546 (1989).

[15] M. Greiner, O. Mandel, T. Esslinger, T. W. Hänsch, and I. Bloch, Nature **415**, 39 (2002).

[16] M. Lewenstein et al., Advances in Physics **56**, 243 (2007).

[17] M. Girardeau, E. Wright, and J. Triscari, Physical Review A **63**, 033601 (2001).

[18] J. M. Luttinger, Journal of Mathematical Physics **4**, 1154 (1963).

[19] T. Kinoshita, T. Wenger, and D. S. Weiss, Science (New York, N.Y.) **305**, 1125 (2004).

[20] B. Paredes et al., Nature **429**, 277 (2004).

[21] D. Petrov, G. Shlyapnikov, and J. Walraven, Physical Review Letters **85**, 3745 (2000).

[22] J. Billy et al., Nature **453**, 891 (2008).

[23] P. W. Anderson, Physical Review **109**, 1492 (1958).

[24] Z. Hadzibabic, P. Krüger, M. Cheneau, B. Battelier, and J. Dalibard, Nature **441**, 1118 (2006).

[25] J. M. Kosterlitz and D. J. Thouless, Journal of Physics C: Solid State Physics **6**, 1181 (1973).

[26] Y. O. Dudin and a. Kuzmich, Science (New York, N.Y.) **336**, 887 (2012).

[27] W. S. Bakr et al., Nature **462**, 74 (2009).

[28] M. Cheneau et al., Nature **481**, 484 (2012).

[29] M. Endres et al., Nature **487**, 454 (2012).

[30] A. McGee, American McGee's Alice, 2000.

[31] E. Tiesinga, B. J. Verhaar, and H. T. C. Stoof, Physical Review A **47**, 4114 (1993).

[32] S. Inouye et al., Nature **392**, 151 (1998).

[33] P. Courteille, R. S. Freeland, D. J. Heinzen, F. A. van Abeelen, and B. J. Verhaar, Physical Review Letters **81**, 69 (1998).

[34] P. O. Fedichev, Y. Kagan, G. V. Shlyapnikov, and J. T. M. Walraven, Physical Review Letters **77**, 2913 (1996).

[35] T. Lahaye et al., Nature **448**, 672 (2007).

[36] K. Singer, J. Stanojevic, M. Weidemüller, and R. Côté, Journal of Physics B: Atomic, Molecular and Optical Physics **38**, S295 (2005).

[37] T. Walker and M. Saffman, Physical Review A **77**, 032723 (2008).

[38] K. Singer, M. Reetz-Lamour, T. Amthor, L. G. Marcassa, and M. Weidemüller, Physical Review Letters **93**, 163001 (2004).

[39] D. Tong et al., Physical Review Letters **93**, 063001 (2004).

[40] T. Vogt et al., Physical Review Letters **97**, 83003 (2006).

[41] R. Heidemann et al., Physical Review Letters **99**, 163601 (2007).

[42] U. Raitzsch et al., Physical Review Letters **100**, 13002 (2008).

[43] H. Weimer, R. Löw, T. Pfau, and H. P. Büchler, Physical Review Letters **101**, 250601 (2008).

[44] H. Weimer and H. P. Büchler, Physical Review Letters **105**, 230403 (2010).

[45] G. Pupillo, A. Micheli, M. Boninsegni, I. Lesanovsky, and P. Zoller, Physical Review Letters **104**, 223002 (2010).

[46] C. Cohen-Tannoudji, J. Dupont-Roc, and G. Grynberg, *Atom-Photon Interactions*, Wiley, 1998.

[47] J. Weiner and P. S. Julienne, Reviews of Modern Physics **71**, 1 (1999).

[48] N. Henkel, R. Nath, and T. Pohl, Physical Review Letters **104**, 195302 (2010).

[49] R. Heidemann, *Rydberg Excitation of Bose-Einstein Condensates: Coherent Collective Dynamics*, PhD thesis, Universität Stuttgart, 2008.

[50] M. Fleischhauer, J. J. P. Marangos, and A. Imamoglu, Reviews of Modern Physics **77**, 633 (2005).

[51] E. Brion, L. H. Pedersen, and K. Mølmer, Journal of Physics A: Mathematical and Theoretical **40**, 1033 (2007).

[52] W. Anderson, J. Veale, and T. Gallagher, Physical Review Letters **80**, 249 (1998).

[53] S. Sachdev, *Quantum Phase Transitions (Google eBook)*, Cambridge University Press, 2011.

[54] F. Robicheaux and J. Hernández, Physical Review A **72**, 063403 (2005).

[55] Y. Colombe et al., Nature **450**, 272 (2007).

[56] A. Gaëtan et al., Nature Physics **5**, 115 (2009).

[57] J. Pritchard et al., Physical Review Letters **105**, 193603 (2010).

[58] M. Saffman and T. Walker, Physical Review A **66**, 65403 (2002).

[59] R. Dicke, Physical Review **93**, 99 (1954).

[60] A. Gorshkov, J. Otterbach, M. Fleischhauer, T. Pohl, and M. Lukin, Physical Review Letters **107**, 133602 (2011).

[61] E. Shahmoon, G. Kurizki, M. Fleischhauer, and D. Petrosyan, Physical Review A **83**, 033806 (2011).

[62] M. Stobiska, G. Alber, and G. Leuchs, EPL (Europhysics Letters) **86**, 14007 (2009).

[63] J. Oreg, F. Hioe, and J. Eberly, Physical Review A **29**, 690 (1984).

[64] M. D. Lukin, M. Fleischhauer, and R. Cote, Physical Review Letters **87**, 037901 (2001).

[65] M. Saffman, T. G. Walker, and K. Mølmer, Reviews of Modern Physics **82**, 2313 (2010).

[66] P. Michler et al., Science **290**, 2282 (2000).

[67] C. Gardiner and P. Zoller, *Quantum Noise: A Handbook of Markovian and Non-Markovian Quantum Stochastic Methods with Applications to Quantum Optics (Google eBook)*, Springer, 2004.

[68] B. Huber et al., Physical Review Letters **107**, 243001 (2011).

[69] B. Misra and E. C. G. Sudarshan, Journal of Mathematical Physics **18**, 756 (1977).

[70] M. Dakna, T. Anhut, T. Opatrný, L. Knöll, and D.-G. Welsch, Physical Review A **55**, 3184 (1997).

[71] D. Walls and G. J. Milburn, *Quantum Optics (Google eBook)*, Springer, 2008.

[72] M. Müller, I. Lesanovsky, H. Weimer, H. P. Büchler, and P. Zoller, Physical Review Letters **102**, 170502 (2009).

[73] M. Saffman, Physical Review Letters **102**, 240502 (2009).

[74] B. Yurke, W. Schleich, and D. Walls, Physical Review A **42**, 1703 (1990).

[75] A. Ourjoumtsev, R. Tualle-Brouri, J. Laurat, and P. Grangier, Science (New York, N.Y.) **312**, 83 (2006).

[76] J. Neergaard-Nielsen, B. Nielsen, C. Hettich, K. Mølmer, and E. Polzik, Physical Review Letters **97**, 83604 (2006).

[77] V. Parigi, A. Zavatta, M. Kim, and M. Bellini, Science (New York, N.Y.) **317**, 1890 (2007).

[78] C. Gerry and P. Knight, *Introductory Quantum Optics*, Cambridge University Press, 2004.

[79] A. Ourjoumtsev, H. Jeong, R. Tualle-Brouri, and P. Grangier, Nature **448**, 784 (2007).

[80] A. Wallraff et al., Nature **425**, 155 (2003).

[81] W. Marshall, C. Simon, R. Penrose, and D. Bouwmeester, Physical Review Letters **91**, 130401 (2003).

[82] M. Sahu et al., Nature Physics **5**, 503 (2009).

[83] A. D. O'Connell et al., Nature **464**, 697 (2010).

[84] A. Caldeira and A. Leggett, Physical Review Letters **46**, 211 (1981).

[85] W. H. Zurek, Reviews of Modern Physics **75**, 715 (2003).

[86] N. Mermin, Reviews of Modern Physics **51**, 591 (1979).

[87] T. W. Neely, E. C. Samson, A. S. Bradley, M. J. Davis, and B. P. Anderson, Physical Review Letters **104**, 160401 (2010).

[88] L. Thompson and P. Stamp, Physical Review Letters **108**, 184501 (2012).

[89] C.-C. J. Wang, R. A. Duine, and A. H. MacDonald, Physical Review A **81**, 013609 (2010).

[90] A. Burkov and E. Demler, Physical Review Letters **96**, 180406 (2006).

[91] P. Vignolo, R. Fazio, and M. Tosi, Physical Review A **76**, 023616 (2007).

[92] P. Nikolić and S. Sachdev, Physical Review B **73**, 134511 (2006).

[93] R. Fazio and G. Schön, Annalen der Physik **524**, 113 (2012).

[94] S. Tung, V. Schweikhard, and E. A. Cornell, Physical Review Letters **97**, 240402 (2006).

[95] H. Pu, L. Baksmaty, S. Yi, and N. Bigelow, Physical Review Letters **94**, 190401 (2005).

[96] J. Reijnders and R. Duine, Physical Review Letters **93**, 060401 (2004).

[97] A. Auerbach, D. P. Arovas, and S. Ghosh, Physical Review B **74**, 064511 (2006).

[98] D. Arovas and A. Auerbach, Physical Review B **78**, 094508 (2008).

[99] O. Fialko, A. Bradley, and J. Brand, Physical Review Letters **108**, 015301 (2012).

[100] N. H. Lindner, A. Auerbach, and D. P. Arovas, Physical Review Letters **102**, 070403 (2009).

[101] N. Lindner, A. Auerbach, and D. Arovas, Physical Review B **82**, 134510 (2010).

[102] M. Fisher and D. Lee, Physical Review B **39**, 2756 (1989).

[103] J. Dalibard, F. Gerbier, G. Juzelinas, and P. Öhberg, Reviews of Modern Physics **83**, 1523 (2011).

[104] A. Sørensen, E. Demler, and M. Lukin, Physical Review Letters **94**, 86803 (2005).

[105] D. Jaksch and P. Zoller, New Journal of Physics **5**, 56 (2003).

[106] A. Altland, B. Simons, and E. Altland, *Condensed Matter Field Theory*, Cambridge University Press, 2006.

[107] S. D. Huber, *Excitations and Transport in Strongly Correlated Bosonic Matter*, PhD thesis, ETH Zürich, 2008.

[108] R. Savit, Reviews of Modern Physics **52**, 453 (1980).

[109] C. Itzykson and J.-M. Drouffe, *Statistical Field Theory: Volume 1, From Brownian Motion to Renormalization and Lattice Gauge Theory*, Cambridge University Press, 1991.

[110] J. D. Jackson, *Classical Electrodynamics Third Edition*, Wiley, third edition, 1998.

[111] G. Blatter, V. B. Geshkenbein, A. I. Larkin, and V. M. Vinokur, Reviews of Modern Physics **66**, 1125 (1994).

[112] D.-H. Lee and M. P. Fisher, International Journal of Modern Physics B **5**, 2675 (1991).

[113] P. M. Chaikin and T. C. Lubensky, *Principles of Condensed Matter Physics*, Cambridge University Press, 2000.

[114] S. D. Huber and N. H. Lindner, Proceedings of the National Academy of Sciences of the United States of America **108**, 19925 (2011).

[115] M. Feigelman, V. Geshkenbein, L. Ioffe, and A. Larkin, Physical Review B **48**, 16641 (1993).

[116] D. P. Arovas and J. Freire, Physical Review B **55**, 1068 (1997).

[117] U. Eckern and A. Schmid, Physical Review B **39**, 6441 (1989).

[118] P. Stamp, E. Chudnovsky, and B. Barbara, International Journal of Modern Physics B **6**, 1355 (1992).

[119] N. H. Lindner and A. Auerbach, Physical Review B **81**, 054512 (2010).

[120] D. Hofstadter, Physical Review B **14**, 2239 (1976).

[121] D. Xiao, M.-C. Chang, and Q. Niu, Reviews of Modern Physics **82**, 1959 (2010).

[122] Y.-J. Lin et al., Nature **462**, 628 (2009).

[123] J. F. S. Brachmann, W. S. Bakr, J. Gillen, A. Peng, and M. Greiner, Optics Express **19**, 12984 (2011).

[124] F. Chevy, K. Madison, V. Bretin, and J. Dalibard, Physical Review A **64**, 031601 (2001).

[125] A. W.-C. Peng, *Quantum Gas Microscope With Optical Lattice*, PhD thesis, Harvard University, 2010.

[126] H. Stormer, Reviews of Modern Physics **71**, 875 (1999).

[127] H. P. Büchler et al., Physical Review Letters **95**, 040402 (2005).

[128] A. Micheli, G. K. Brennen, and P. Zoller, Nature Physics **2**, 341 (2006).

[129] L.-M. Duan, E. Demler, and M. Lukin, Physical Review Letters **91**, 90402 (2003).

[130] H. Weimer, M. Müller, I. Lesanovsky, P. Zoller, and H. P. Büchler, Nature Physics **6**, 382 (2010).

[131] Y.-J. Han, R. Raussendorf, and L.-M. Duan, Physical Review Letters **98**, 150404 (2007).

[132] M. Roncaglia, M. Rizzi, and J. Dalibard, Scientific reports **1**, 43 (2011).

[133] R. Palmer and D. Jaksch, Physical Review Letters **96**, 180407 (2006).

[134] D. N. Sheng, Z.-C. Gu, K. Sun, and L. Sheng, Nature Communications **2**, 389 (2011).

[135] B. Juli et al., New Journal of Physics **14**, 55003 (2012).

[136] M. Popp, B. Paredes, and J. Cirac, Physical Review A **70**, 53612 (2004).

[137] M. Baranov, K. Osterloh, and M. Lewenstein, Physical Review Letters **94**, 70404 (2005).

[138] I. Bloch, J. Dalibard, and S. Nascimbène, Nature Physics **8**, 267 (2012).

[139] J. F. Sherson et al., Nature **467**, 68 (2010).

[140] S. Sachdev, K. Sengupta, and S. Girvin, Physical Review B **66**, 75128 (2002).

[141] M. Kolodrubetz, B. Clark, and D. Huse, Physical Review Letters **109**, 15701 (2012).

[142] S. Pielawa, T. Kitagawa, E. Berg, and S. Sachdev, Physical Review B **83**, 205135 (2011).

[143] K. Winkler et al., Nature **441**, 853 (2006).

[144] Y.-M. Wang and J.-Q. Liang, Physical Review A **81**, 45601 (2010).

[145] A. J. Daley, C. Kollath, U. Schollwöck, and G. Vidal, Journal of Statistical Mechanics: Theory and Experiment **2004**, P04005 (2004).

[146] S. R. White and A. E. Feiguin, Physical Review Letters **93**, 076401 (2004).

[147] W. S. Bakr et al., Nature **480**, 500 (2011).

[148] A. Janisch, *Scattering properties of quantum degenerate atomic gases*, PhD thesis, Universität Stuttgart, 2009.

[149] N. Nygaard, R. Piil, and K. Mølmer, Physical Review A **78**, 23617 (2008).

[150] T. F. Gallagher, *Rydberg Atoms*, Cambridge Monographs on Atomic, Molecular And Chemical Physics, Cambridge University Press, 2005.

[151] W. Li, I. Mourachko, M. Noel, and T. Gallagher, Physical Review A **67**, 052502 (2003).

[152] A. Grabowski, *Aufbau einer Messapparatur zur Laserkühlung und hochauflösende Rydberg-Spektroskopie an 87 Rb-Atomen*, PhD thesis, Universität Stuttgart, 2006.

[153] D. Jaksch, J. I. Cirac, P. Zoller, R. Côté, and M. D. Lukin, Physical Review Letters **85**, 2208 (2000).

[154] V. Vuletic, Nat. Phys. **2**, 801 (2006).

[155] S. Diehl, E. Rico, M. A. Baranov, and P. Zoller, Nature Physics **7**, 971 (2011).

[156] H.-P. Breuer and F. Petruccione, *The Theory of Open Quantum Systems*, Oxford University Press, 2002.

Acknowledgements

The last three and some years have been an extraordinary time in my life, and there are a great many people I wish to thank for that: First and foremost, my gratitude goes to Professor Hans Peter Büchler, who has been a great advisor and a real inspiration and I do owe him deeply for the opportunity to do research on such an interesting topic. Thank you! To Professor Walter Metzner, who I only met a few weeks ago, but who nevertheless showed a strong interest in my work and, to my fortune, made a real effort in creating a calm atmosphere in my exam. I am grateful to Professor Tilman Pfau for introducing me to atomic physics. I benefitted vastly from his teaching and the time I spent at PI5, even though I joined the theory department later on. And of course thanks to Gil Refael, Tony Lee, Alexey Gorshkov, David Pekker and Kun Woo Kim for the awesome time at Caltech. Also thanks to all of my colleges at the Institute for Theoretical Physics III. It was a pleasure working with you, and I really enjoyed the discussions during the coffee-breaks, some of which even involved actual physics. Especially, I'd like to thank Thorsten, with whom I spent lots of fun hours bouldering, Adam for all those discussions about video games, and Michael, who had my back in the final weeks before my exam. I owe to Mrs. Poljak and Mr. Nagel for all those times they were helping me to avoid the perils of university administration.

Many thanks to all those people I spent the last couple of years bouldering with, and who were vastly responsible for the necessary distraction from the hours spent in front of my desk. In particular I want to thank Eva and Freddy, with whom I also had the pleasure to share a flat for quite some time. A special thanks goes out to Seba, Werner and Martin, who always motivated and inspired me, and are responsible for the small amount of climbing technique I managed to acquire. And, of course, Sudabeh, who can always find the right words to make one smile. Moreover, I should thank John “TB” Bain for playing his part in keeping me sane during my PhD. *Indeed.* Thanks to all of my friends, some of which I probably have dearly neglected while writing this thesis, but who are nevertheless very dear to me. Here, Andi deserves a special place. I had a great time climbing with you, and I will never forget the both of us traveling through Thailand without any clue whatsoever. I'm sorry for your lost weight, though. I promise I will feed you better next time. And Natalie, thanks for allowing Andi to come along with me. Again, I promise to feed him better next time. Thanks to my ex-flat-mates and friends Jan

and Leonie. It was awesome living with you, and I intent to hold on to our Tichu sessions. Then, of course, my old gaming group: Matthias, Steffen, Falk, Martin, Ferdi and his wife Meike (whose name I always spell wrong). I hope there will be more time to play in the future! If not, well, we'll make some. Steffi, thanks for the occasional coffee, and sharing the daily problems of a PhD-student. To Daniel, thanks for you just being you. Drop in whenever you like. And Jakob, you are a real inspiration to me, and I am looking forward to regaining our endurance together. Last, my dearest friend Denis. What can I say? I think both of us have come a long way in the years since we first met. Even so, I still consider you my best friend. And I am quite sure that despite everything that is going on, this will not change.

Finally, a big thanks goes out to all of my and Jessi's Family, who not only supported me during the time of my PhD but my whole life. I would never have been able to do it without your support. I thank especially my parents, who always believed in me, and my little brother, who I very much admire.

And, well, Jessi. I love you!